

DISSERTATION IN ASTRONOMY

SUBMITTED TO THE
COMBINED FACULTIES OF THE NATURAL SCIENCES AND MATHEMATICS
OF THE
RUPERTO-CAROLA-UNIVERSITY OF HEIDELBERG
GERMANY

FOR THE DEGREE OF
DOCTOR OF NATURAL SCIENCES

PUT FORWARD BY

MAURICIO ORTIZ ÁLVAREZ
BORN IN SANTIAGO, CHILE

ORAL EXAMINATION: 14 DECEMBER 2016

PLANETS AROUND GIANT STARS

TWO CLOSE-IN TRANSITING PLANETS AND ONE S-TYPE PLANET IN AN ECCENTRIC BINARY SYSTEM

Mauricio Ortiz Álvarez

Landessternwarte, Zentrum für Astronomie

**Referees: Prof. Dr. Andreas Quirrenbach
PD. Dr. Hubert Klahr**

Abstract

The study of planets around giant stars is an excellent way of probing the effects of stellar evolution on planetary systems. This is because as the star evolves from its main-sequence (MS) lifetime into the red giant branch (RGB) phase, it experiences important physical changes, like for example, significant mass loss, increase of the stellar radius and luminosity variability. These effects have the potential of influencing the whole architecture of planets that might have formed previously in the system. Additionally, as giant stars are generally more massive than MS stars, the effects of stellar mass on planet formation and migration theories can be tested. In this thesis, planets around evolved stars are studied from different perspectives.

First, a comprehensive radial velocity (RV) follow-up of transiting planet candidates around evolved stars – observed by the *Kepler* telescope – was initiated to unveil a population of close-in planets ($a < 0.5$ au) that have been undetected by previous RV surveys. This effort led to the confirmation of the planetary nature of two close-in planets, Kepler-432 b and Kepler-91 b, providing evidence that short-period planets can exist around intermediate-mass evolved stars. These results suggest that gravitational interaction, with other planets or stars, is likely to be the preferred migration channel for close-in planets in intermediate-mass giant stars. Additionally, the findings in this thesis are in agreement with the view in which the scarcity of short-period planets around clump giants is explained by an increased planet-star tidal interaction during the RGB, subsequently leading to the tidal engulfment of giant planets.

In the second part of this thesis, a very interesting binary system hosting a giant planet is analyzed. The planet, HD 59686 Ab, is orbiting the primary K-giant star at ~ 1 au, while the stellar companion is in a very eccentric orbit ($e \sim 0.7$) with a small semi-major axis of ~ 13.6 au. The existence of this planet in a tight eccentric binary system severely challenges the standard view in which gas giant planets form beyond the ice line of their hosts and then experience a migration phase to reach their current positions. The planet HD 59686 Ab presented in this thesis can become a benchmark object for the study of giant planets in close-separation binaries and might allow to shed light onto different planet formation theories in tight binaries.

Zusammenfassung

Die Untersuchung von Planeten um Riesensterne ist ein ausgezeichnete Weg um die Effekte stellarer Evolution auf Planetensysteme zu untersuchen. Denn ein Stern welcher sich von der Hauptreihe (MS, en. *main sequence*) hin zum Roten Riesen Ast (RGB, en. *red giant branch*) entwickelt erfährt wichtige physikalische Veränderungen. Zum Beispiel verliert er einen Signifikanten Teil seiner Masse, vergrößert seinen Radius und variiert seine Leuchtkraft. Diese Effekte haben einen möglichen Einfluss auf die gesamte Architektur der Planeten welche sich möglicherweise vorher im System gebildet hatten. Zusätzlich sind Riesensterne im Allgemeinen massereicher als MS-Sterne, sodass Effekte der Sternmasse auf Planetenentstehung und Migrationstheorien getestet werden können. In dieser Arbeit werden nun Planeten um Entwickelte Sterne aus verschiedenen Blickwinkeln untersucht.

Zunächst wurde eine umfangreiche Nachbeobachtungsreihe mittels Radialgeschwindigkeit (RV, en. *radial velocity*) von Planetenkandidaten – beobachtet mit dem *Kepler* Weltraumteleskop – um Entwickelte Sterne in die Wege geleitet. Diese hatte das Ziel eine Population sternnaher Planeten ($a < 0.5$ au, en. *astronomical unit*) zu enthüllen welche in vorherigen RV-Beobachtungen unentdeckt blieben. Diese Bemühungen führten zur Bestätigung zweier sternnaher Planeten: Kepler-432-b und Kepler-91b. Mit diesen war nun bewiesen, dass Planeten mit kurzen Umlaufzeiten um mittelschwere Entwickelte Sterne existieren können. Dies legt wiederum die Vermutung nahe, dass gravitative Wechselwirkungen – mit anderen Planeten oder Sternen – der bevorzugte Migrationskanal für sternnahe Planeten um mittelschwere Riesensterne ist. Zusätzlich sind die Resultate in dieser Arbeit in Übereinstimmung mit der Sichtweise dass Planeten mit kurzen Umlaufzeiten um Geklumpte Riesen deshalb rar sind, da die verstärkten Gezeitenkräfte zwischen Planet und Stern während der RGB-Phase zu einem Verschlingen des Riesenplaneten führt.

Im zweiten Teil wird dann ein sehr interessantes Binärsystem mit einem Riesenplaneten analysiert. Der Planet, HD 59686 Ab umkreist den primären K-Riesen während der stellare Begleiter auf einer sehr exzentrischen Bahn ($e \sim 0.7$) mit einer kleinen Großen Halbachse von nur ~ 13.6 au kreist. Die Existenz dieses Planeten in einem engen, exzentrischen Orbit stellt das Standardmodell der Entstehung von Riesenplaneten infrage: hier nämlich entstehen die Riesenplaneten jenseits der Eislinie ihres Zentralsterns um dann während einer Migrationsphase auf ihre jetzige Bahn zu gelangen. Der in dieser Arbeit präsentierte Planet HD 59686 Ab kann als Maßstab für die Untersuchung von sternnahen Riesenplaneten dienen und erlaubt uns vielleicht sogar Aufschluss über verschiedene Planetenentstehungstheorien in engen Binärsystemen zu geben.

*A mi familia y amigos
y a mi querida esposa*

Contents

List of Figures	xiii
------------------------	-------------

List of Tables	xxiii
-----------------------	--------------

1 Introduction	1
1.1 A brief history of exoplanet detections	1
1.2 Tools and techniques for exoplanet detection	3
1.2.1 Radial velocity	3
1.2.1.1 Keplerian orbits	4
1.2.1.2 Description of orbital motion	6
1.2.1.3 Radial velocity curve	7
1.2.1.4 Calculation of Doppler shifts	9
1.2.2 Photometric transit	12
1.2.2.1 Description of light curves	13
1.2.2.2 Light curve modulations	15
1.2.2.3 Bayesian modeling	18
1.2.2.4 Kepler mission	19

1.3	Planets in giant stars	21
1.3.1	Properties of planets around giant stars	21
1.3.2	Occurrence rate of planets in giant stars	24
1.3.3	Close-in planets around giant stars	25
1.4	Planets in binary stars	26
1.4.1	The role of binarity in giant planet formation	26
1.4.2	Types of planets in binary systems	27
1.4.3	Planets in close-separation binaries	29
2	The transiting warm Jupiter Kepler-432 b	33
2.1	Context	33
2.2	High-resolution spectroscopic follow-up	34
2.3	Results	35
2.3.1	Stellar properties	35
2.3.2	Orbit and planet parameters	36
2.4	Discussion	38
2.4.1	Internal structure and equilibrium temperature	38
2.4.2	Kepler-432 b: a close-in eccentric planet	40
2.4.3	Comparison with other works	41
2.4.4	Post-main-sequence evolution	43
2.5	Summary	45
3	The transiting hot Jupiter Kepler-91 b	47
3.1	Context	47
3.2	High-resolution spectroscopic follow-up	49

3.3	Spectroscopic parameters	49
3.4	Transit and radial velocity modeling	50
3.4.1	Overview	50
3.4.2	Data	51
3.4.2.1	Kepler long cadence photometry	51
3.4.2.2	Radial velocity observations	51
3.4.3	Log posterior density	51
3.4.4	Radial velocity model	52
3.4.5	Light curve model	52
3.4.5.1	Reflected and emitted flux	53
3.4.5.2	Ellipsoidal variations	53
3.4.5.3	Doppler boosting	53
3.4.6	Parameterization and priors	54
3.4.7	Numerical methods	54
3.4.8	Derived parameters	54
3.4.8.1	Bond albedo	54
3.4.8.2	Brightness temperature	55
3.4.8.3	Planetary mass from ellipsoidal variation	55
3.5	Results	55
3.6	Discussion	60
3.6.1	Physical properties of the planet	60
3.6.2	Eccentricity	62
3.6.3	Close-in planets around evolved stars	64
3.6.4	Implications for planet migration	67

3.7	Summary	68
4	The S-type planet HD 59686 Ab in an eccentric close binary	71
4.1	Context	71
4.2	Observations	73
4.3	Results	74
4.3.1	Stellar properties	74
4.3.2	Keplerian orbits	75
4.4	Validating the planetary signal	79
4.4.1	Rotational modulation	79
4.4.2	Infrared radial velocities	79
4.4.3	Photometry	82
4.4.4	Spectral activity indicators	84
4.4.5	Discarding a hierarchical triple star system	86
4.5	High-contrast images	87
4.5.1	Previous search for stellar companions in HD 59686 A	87
4.5.2	Observations and data reduction	88
4.5.3	PSF subtraction	88
4.5.4	Contrast curve calculation	91
4.6	Discussion	93
4.6.1	HD 59686 Ab: a planet in a close-separation binary	93
4.6.2	Nature of the stellar object HD 59686 B	95
4.6.3	Possible origin of the planet HD 59686 Ab	98
4.7	Summary	100

5	Summary and Outlook	103
5.1	Review of the thesis	103
5.2	Close-in planets around evolved stars	104
5.3	Circumstellar planets in binary systems	106
5.4	Future and ongoing exoplanet projects	106
A	Radial velocity observations of Kepler-432	109
B	Radial velocity data of Kepler-91 and posterior samples from the MCMC fitting	111
C	Radial velocity observations of the giant star HD 59686 A	117
	Acknowledgements	121
	Abbreviations and Acronyms	123
	Bibliography	126

List of Figures

1.1	The left panel shows the period variations of the millisecond pulsar PSR 1257+12 fitted by a 2-planet model with masses of $\sim 4 M_{\oplus}$ and periods of 66 and 98 days. The right panel plots the RV oscillations of the solar-type star 51 Peg induced by the $0.5 M_{\text{Jup}}$ hot Jupiter planet 51 Peg b orbiting the star every 4.2 days. Figures taken from Wolszczan & Frail (1992) and Mayor & Queloz (1995)	2
1.2	Three-dimensional representation of a Keplerian elliptical orbit. Figure taken from Perryman (2011)	4
1.3	Representation of an elliptical orbit of planetary motion. The auxiliary circle has a radius equal to the semi-major axis a . The semi-minor axis is b . The true anomaly ν describes the points on the elliptical orbit at a certain time. Alternatively, the points in the ellipse can be also described by the eccentric anomaly E . The focus of the ellipse is F_1 , which also represents the system barycenter. Figure taken from Perryman (2011)	6
1.4	Examples of the modeling of the stellar spectrum and the I_2 cell for the stars 16 Cyg B (left panel) and τ Cet (right panel). The plots show the I_2 template spectrum, the star template spectrum, the observed spectrum taken through the I_2 cell (dots) together with the model (solid line), and the residuals from the fit (5 times the difference between the model and the observation). The observation is modeled as the product of the I_2 and stellar template spectra convolved with the derived instrumental profile of the spectrograph using Equation 1.12. Figure taken from Sato et al. (2002)	10

- 1.5 Cross-correlation function for a K0 III star with a $S/N = 1$. The spectral resolution is $R = 40\,000$ spanning the range $4110 - 4440 \text{ \AA}$ in ten orders (letters a to j). The top panel is the same order as the one below, but with a $S/N = 40$. The lower panel shows the derived cross-correlation function. Figure taken from [Queloz \(1995\)](#). 11
- 1.6 Schematic diagram showing a planetary transit. During the transit, the planet blocks a fraction of the star light. After the transit, the planet's brighter day-side progressively comes into view, and the total flux rises. It drops again during the secondary eclipse as the planet passes behind the star. In the upper plot are shown the contact points (one to fourth) for a smaller impact parameter b (dotted circles) and a larger value of b (dashed circles). For smaller b , the circles are more closely separated in time, and the ingress/egress slopes correspondingly steeper. The total transit duration t_T is between first and fourth contact, while t_F is timed between second and third contact. Figure from [Winn \(2009\)](#) adapted by [Perryman \(2011\)](#). 15
- 1.7 Example of the phase folded light curve of the planet-hosting star KOI-13. The left panel shows the *Kepler* long cadence data (grey dots), the binned data (black points) and the corresponding sinusoidal model constructed taking into account the effects of the out-of-transit modulations (solid line). The right panel illustrates the relative contribution of the three effects modeled: beaming (B), ellipsoidal (E) and reflection (R). The solid black line is the fitted double harmonic model, which is the sum of the three effects. Figure taken from [Shporer et al. \(2011\)](#). 17
- 1.8 The left panel shows the planet mass versus orbital period for the non-*Kepler* discoveries color-coded according to the detection technique. The same planets are plotted in the left panel where the mass-radius relation from [Lissauer et al. \(2011\)](#) has been used to transform planet mass to radius. Additionally, all the *Kepler* discoveries (yellow) are added for comparison. 86% of the non-*Kepler* planets are larger than Neptune while the inverse is true for the *Kepler* discoveries: 85% of the *Kepler* planets are smaller than Neptune. Figure taken from [Batalha \(2014\)](#). 20

- 1.9 Planet mass (minimum) as a function of the semi-major axis (left panel) and the stellar mass (right panel) for planets around solar-type stars (black dots), subgiants (blue triangles) and giant stars (red circles). The dashed lines correspond to a RV amplitude of 30 m s^{-1} , for a planet orbiting a star with a mass of $1.5 M_{\odot}$ (left panel) at an orbital distance of 1 au (right panel). Figure taken from [Jones et al. \(2014\)](#). 22
- 1.10 The left panel shows the planet occurrence as a function of stellar metallicity for the sample of 373 G and K giant stars from the Lick survey (not taking into account the stellar mass effect). The red histogram shows secure planets, while the open purple one shows planet candidates. The solid line is an exponential fit to the occurrence rate in the secure planet sample for a stellar mass of $1.9 M_{\odot}$. The black dots are also an exponential fit, but taking into account the individual mass distribution in each bin. The right panel is the planet occurrence as a function of mass, ignoring the effects of metallicity. The solid line represents the best Gaussian fit for zero metallicity and the black dots take into account the metallicity distribution in each bin. Figure taken from [Reffert et al. \(2015\)](#). 24
- 1.11 Schematic representation of the S- (left panel) and P-type orbits (right panel). In the case of the S-type orbits, the two stars of the binary revolve around their center of mass (CoM) while the planet orbits only one of the stars. For P-type orbits both stars and the planet rotate around the center of mass of the binary (shown by CoM). Figures taken from [Haghighipour & Kaltenegger \(2013\)](#) and [Kaltenegger & Haghighipour \(2013\)](#). 28
- 1.12 Architecture of all S-type planets around binary stars with a separation of $a_B < 1000 \text{ au}$ (as it was until July 2013). Stellar companions are displayed with yellow circles, whose size is proportional to the binary mass ratio M_2/M_1 . Planets are represented by blue circles, whose size is proportional to the planet mass. The horizontal lines in each of the symbols marks the radial excursion of the planets and stars orbit (when they are known). For most binaries of separation $\geq 100 \text{ au}$, the orbit is not known and the displayed value corresponds to the projected current separation. The short vertical lines correspond to the outer limit of the orbital stability region around the primary star, as derived by [Holman & Wiegert \(1999\)](#). Figure taken from [Th ebault & Haghighipour \(2015\)](#). 30

- 2.1 Radial velocity measurements of Kepler-432. *Upper panel:* CAFE (blue circles) and FIES (red squares) RVs, and Keplerian fit to the data (black solid line) – including the linear RV trend. *Middle panel:* RV residuals. The rms is ~ 17 m/s and ~ 5 m/s for the CAFE and FIES data, respectively. The observed rms of the FIES RVs is consistent with the expected value of ~ 6 m/s for a star with $\log g = 3.35$ dex (Hekker et al. 2008; Nowak 2013). Quadratically adding a jitter of 6 m/s to our formal RV measurement errors does not change the derived orbital parameters significantly ($< 1\sigma$). Additionally, a fit to the FIES data alone yields consistent results within 1σ . *Lower panel:* Bisector velocity span (BVS) of the FIES CCF versus RVs, assuming that the error bars of the former are twice those of the latter. 37
- 2.2 Radius and masses of the known transiting exoplanets (black empty circles). The position of Kepler-432 b is marked by the red triangle. The Fortney et al. (2007) isochrones for planet core masses of 0, 10, 25, 50, and $100 M_{\oplus}$ – interpolated to the insolation and age of Kepler-432 b – are overplotted with dashed lines from top to bottom. The upper left inset is a zoom around Kepler-432 b. Also shown are models for planets of different compositions derived by Seager et al. (2007). Solar system planets are marked with magenta letters. We note that Kepler-432 b falls in a region with a lack of planets between ~ 4.5 and $\sim 7 M_{\text{Jup}}$ 39
- 2.3 *Left panel:* Eccentricity and semi-major axis of the extrasolar planets discovered around MS stars (black dots) and giant stars (magenta circles). The dashed line shows the value of $a = 0.5$ au. *Right panel:* Orbital period versus stellar mass. The dashed lines represent the region of $10 \leq P_{\text{orb}} \leq 100$ days. The position of Kepler-432 b is marked with a green triangle in both panels. 41
- 2.4 The upper plots show the RV signal caused by Kepler-432 b (left) and Kepler-432 c (right), while the bottom plot is the combined RV time series. Red colors represent data obtained with FIES and blue colors with TRES. For Kepler-432 c, the light blue color is the individual RVs and the dark blue is the binned data. Figure taken from Quinn et al. (2015). 42
- 2.5 Evolution of the stellar radius (solid line) during the RGB and the semi-major axis (dash-dotted line) of a $1 M_{\text{Jup}}$ planet. Different MS stellar masses are also shown, and the set of dashed lines are the orbits for different initial values for the semi-major axis. Figure taken from Villaver & Livio (2009). 44

- 3.1 The upper panel shows the phase-folded light curve (red points) centered at the mid-transit time, together with the best-fit transit model (blue solid line). The data were binned (black points) with 500 observed points per bin. The lower panel shows the residuals from the transit model. 56
- 3.2 The upper panel shows the phase-folded and binned *Kepler* light curve (blue line) and the model including the effects of reflection/emission from the planet, ellipsoidal variations and Doppler beaming (black line). The lower panel plots the FIES (blue), CAFE (green), HRS (red), and HDS (purple) radial velocity dataset with the best-fit Keplerian model (black line). 57
- 3.3 Planetary radius as a function of planet mass for all the transiting planets with $0.1 < M_p < 2 M_{\text{Jup}}$. Also shown is the model from Fortney et al. (2007) for a coreless planet interpolated to the insolation and age of Kepler-91 b (black solid line). The black dashed line marks the approximate limit of $R_p \sim 1.2 R_{\text{Jup}}$ defining an inflated planet (Lopez & Fortney 2016). The position of Kepler-91 b is shown in red color. The radius of the planet is more than 2σ above the predicted value from the Fortney et al. model. 61
- 3.4 Planetary radius as a function of the equilibrium temperature for all the transiting hot Jupiters. The current incident flux on the planets is color coded. There is an evident correlation between the flux received by the planet and its radius. Kepler-91 b is a highly irradiated planet with an equilibrium temperature of $T_{\text{eq}} = 2186 \pm 16$ K that falls well within the trend observed for the rest of hot Jupiters. 62
- 3.5 Posterior distribution for the orbital eccentricity of the planet Kepler-91 b. The derived eccentricity is small, but significant at the 6σ level, and we can rule out with a high probability a circular orbit. 63
- 3.6 Semi-major axis of planets around MS (black dots), giant (red circles) and subgiant stars (with $a < 0.5$ au, green squares) as a function of the host-star radius. The blue dashed line marks the value of $a = 0.5$ au to define a close-in planet. Transiting planets are highlighted with filled symbols. The *Kepler* mission alone (including K2) has discovered 65% of the close-in planets around evolved stars. 65

- 3.7 Semi-major axis of planets around giant (red symbols) and subgiant stars (with $a < 0.5$ au, green squares) as a function of the host-star mass. The blue dashed line marks the value of $a = 0.5$ au to define a close-in planet. Transiting planets are highlighted with filled symbols. The giant stars with a radius larger than $10 R_{\odot}$ are marked with a cross. 66
- 4.1 Radial velocity measurements of the HD 59686 system. Note that a jitter of 19.83 m s^{-1} was added in quadrature to the formal RV uncertainties, and this is reflected in the plot. *Upper left*: Lick RVs together with the best Keplerian fit to the data. *Upper right*: RV residuals from the fit. *Lower left*: Phased RV variations and Keplerian fit for the $\sim 7 M_{\text{Jup}}$ planet HD 59686 Ab after subtracting the signal of the stellar companion. *Lower right*: RV data and Keplerian fit for the $\sim 0.5 M_{\odot}$ stellar object HD 59686 B after subtracting the planetary signal. 77
- 4.2 *Top*: GLS periodogram of the RV data of HD 59686 A. The significant peaks at ~ 5000 and ~ 340 days represent the orbits of the stellar and planetary companions, respectively. The 5000-day period is the time frame of our observations, therefore it is much shorter than the actual stellar period. The dotted, dashed, and dash-dotted lines show FAPs of 0.1%, 1%, and 5%, respectively. *Middle*: Periodogram of the residual RVs after the signal due to the stellar companion is removed from the data. Now the peak due to the planetary companion becomes much stronger and the alias period at ~ 400 days disappears. Additionally, another alias period appears at ~ 1700 days. *Bottom*: Periodogram of the residual RVs after subtracting the orbital fit (stellar+planetary companions); it shows no significant peaks. 78
- 4.3 *Upper panel*: CRIRES infrared RV measurements of HD 59686 A. The black solid line shows the best Keplerian fit obtained from the Lick data alone. *Bottom panel*: Residuals of the CRIRES RVs from the optical fit. The value of the rms is $\sim 59 \text{ m s}^{-1}$, which is consistent with the large infrared RV errors. The mean error of the CRIRES data, with a jitter of 19.83 m s^{-1} added in quadrature, is $\sim 45 \text{ m s}^{-1}$ 81
- 4.4 *Upper panel*: GLS periodogram of the $H\alpha$ index measurements of HD 59686 A. *Bottom panel*: GLS periodogram of the Hipparcos V-band photometry of HD 59686 A. The dotted, dashed, and dash-dotted lines in both panels show FAPs of 0.1%, 1%, and 5%, respectively, obtained by bootstrapping. No significant periodicities are found in the data. 83

- 4.5 *Upper panel:* $H\alpha$ index measurements at the time of each RV observation of HD 59686 A. *Bottom panel:* $H\alpha$ index measurements as a function of the RVs due to the planetary companion HD 59686 Ab, that is, with the stellar component subtracted from the data. No significant correlation is seen in the data, which corroborates that a giant planet is part of the system. 85
- 4.6 High-contrast L' -band LMIRCam images of HD 59686 A. Panels *a, b, c,* and *d* show the residual images after running the PCA with 10, 38, 77, and 81 principal components. Panel *e* shows the image obtained with a local, subannular PCA approach, and panel *f* presents the residual image after subtracting the stellar PSF using the new LLSG algorithm. No signal of the companion star HD 59686 B is detected in any of the panels. 90
- 4.7 $5\text{-}\sigma$ detection limits in terms of the magnitude contrast in the L' -band as a function of the distance from the central star. The black dashed line represents the binary separation upper limit of ~ 11.7 au at the time of the observations. The dash-dotted line marks the saturation radius of $\sim 0.085''$. The red solid lines mark the expected contrasts for a G2 V star of $1 M_{\odot}$ and a M0 V star of $0.5 M_{\odot}$, from top to bottom. 92
- 4.8 Sky-projected orbit of the HD 59686 binary system assuming values of $i = 50^{\circ}$ and $\Omega = 45^{\circ}$ for the orbital inclination and longitude of the ascending node, respectively. Labeled in the orbit are the positions of each star as a function of time. The green symbol marks the position of HD 59686 A and HD 59686 B at the time of our LBT observations. The dotted line is the line of nodes, and the letter P denotes the positions of the stars at periastron. The yellow dot marks the center of mass of the system. 93
- 4.9 Semi-major axis of planetary companions plotted against binary separation for all known planet-hosting binary systems. Shown are binaries with MS (blue circles) and evolved subgiant/giant (red triangles) primary stars as well as two microlensing binaries (green squares), in which the spectral type of the stars is not known. The filled symbols show binaries in which the secondary star is a white dwarf. The position of the HD 59686 system is marked with a red cross. The dashed line marks the 1:1 relation between planet semi-major axis and binary separation. Most of the discovered planets are found in binary stars with separations greater than ~ 100 au. 94

4.10	Final periods and eccentricities resulting from all simulations that led to the formation of a HB giant star with a WD companion. The initial masses of the stars were 1.9 and 2.3 M_{\odot} . We also show histograms reflecting the distribution of final periods and eccentricities. The position of the HD 59686 system is marked with a red asterisk. <i>Left panel:</i> Results for $B_W = 0$, meaning that the mass loss is treated with the traditional Reimers prescription. It is clear that none of the simulations can reproduce the HD 59686 system. In the majority of the cases the orbit is fully circularized due to tidal interactions during the AGB phase. <i>Right panel:</i> Results for an enhanced mass-loss rate ($B_W = 10^4$) showing that a large fraction of initial orbital conditions lead to long-period and eccentric binaries similar to the HD 59686 system. The black solid line marks the period and eccentricity evolution of the model that agrees best with the orbital properties of HD 59686 AB.	97
B.1	Histograms of the marginalized posterior distributions of the 24 parameters included in the MCMC planet model.	114
B.2	Histograms of the marginalized posterior distributions of the derived physical parameters of Kepler-91 b.	115

List of Tables

2.1	Stellar parameters of Kepler-432.	36
2.2	Orbital parameters of Kepler-432 b.	38
3.1	Stellar parameters of Kepler-91.	50
3.2	Model parameterization and priors.	58
3.3	Orbital parameters of Kepler-91 system.	59
4.1	Stellar parameters of HD 59686 A.	75
4.2	Orbital parameters of the HD 59686 system.	76
A.1	CAFE and FIES radial velocity measurements of Kepler-432.	110
B.1	CAFE, FIES, HRS, and HDS radial velocity measurements of Kepler-91.	112
C.1	Radial velocity data of HD 59686 A.	118

Introduction

1.1 A brief history of exoplanet detections

The notion of other *worlds* besides our own dates back more than 2000 years in the past, in ancient Greece. Around the year 305 B.C., in his Letter to Herodotus¹, the Greek Philosopher Epicurus (341–270 B.C.) already said: “*there is an infinite number of worlds, some like this world, others unlike it*”. He went even further writing: “*For nobody can prove that in one sort of world there might not be contained, whereas in another sort of world there could not possibly be, the seeds out of which animals and plants arise and all the rest of the things we see*”. Although the meaning of *worlds* back then is not the same as the modern concept of a planet, the words written by Epicurus symbolize the inherent human curiosity of wondering about our place in the universe and the existence of other *worlds*. More than 2000 years later, the question of other *worlds* is still valid, but posed in a modern scientific way: are there other planets or planetary systems around the billions of stars in the Milky Way? To answer that question a collective effort of brilliant people and technological advances was necessary that probably started with the Galilean revolution in the European Renaissance and the establishment of the scientific method.

Perhaps, the first notion of the scientific method was developed by the Arabic scientist al-Hasan Ibn al-Haytham (965–1040). His book *Kitab al-Manazir*² about Optics was translated into Latin and read by several brilliant scientists in Europe ([Zewail & Thomas 2010](#); [Al-Khalili 2015](#)). From then on the ideas of Francis Bacon and René Descartes, among others, contributed to a more robust understanding of science by switching from the Aristotelian deduction method to

¹Diogenes Laertius, *Lives of Eminent Philosophers*, Volume II: Books 6-10. Translated by R. D. Hicks. Loeb Classical Library 185. Cambridge, MA: Harvard University Press, 1925

²The meaning of the phrase is Book of Optics. See the article of [Al-Khalili \(2015\)](#) for a revision.

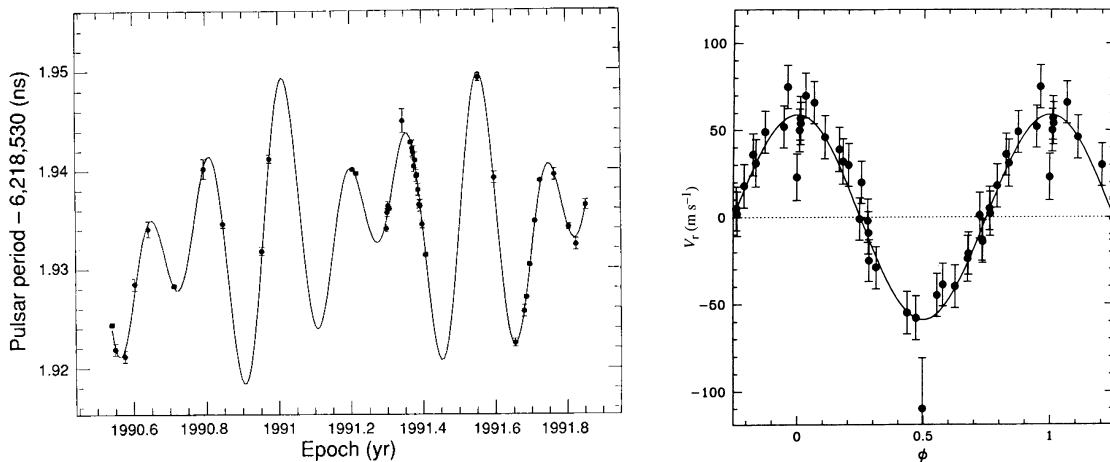


Figure 1.1: The left panel shows the period variations of the millisecond pulsar PSR 1257+12 fitted by a 2-planet model with masses of $\sim 4 M_{\oplus}$ and periods of 66 and 98 days. The right panel plots the RV oscillations of the solar-type star 51 Peg induced by the $0.5 M_{\text{Jup}}$ hot Jupiter planet 51 Peg b orbiting the star every 4.2 days. Figures taken from [Wolszczan & Frail \(1992\)](#) and [Mayor & Queloz \(1995\)](#).

a more experimental-based approach. This scientific revolution reached its highest point with two groundbreaking works: the description of what is now known as kinematics and strength of materials by Galileo Galilei ([Galilei 1638](#)) and the formulation of the laws of gravitation by Isaac Newton ([Newton 1687](#)). These works established the foundations of modern science and allowed to go from ideas and mere speculations to well tested and scientific theories.

The modern history that led to the detection of the first extrasolar planet around a star similar to the Sun started in the early 1940s, when a few claims of planetary bodies outside the Solar System were made³ ([Strand 1943](#); [Reuyl & Holmberg 1943](#)). Later, several groups started to look for planets relying on the idea that the gravitational influence of a minor body orbiting around a star would cause a shift in its radial velocity (RV), which could be measured in the stellar spectrum⁴. This method is based on measuring tiny periodic shifts of spectral absorption lines, which at the time was extremely challenging. This was a severe problem for decades until in the early 1980s, the pioneering work of [Campbell & Walker \(1979\)](#) demonstrated an RV precision⁵ of $\sim 13 \text{ m s}^{-1}$. They started an RV survey of around 20 solar-type stars to look for Jupiter-analogs that ended many years later with no detections ([Walker et al. 1995](#)). Another effort had been also initiated by [Marcy & Butler \(1993\)](#) monitoring 25 solar-like stars obtaining similar, non-positive, results ([Marcy & Butler 1994](#)).

³The suggested existence of these planets was subsequently probed wrong by several works: [Heintz \(1978\)](#), [Walker et al. \(1995\)](#), [Cumming et al. \(2008\)](#).

⁴This idea had been proposed before by [Belorizky \(1938\)](#) and [Struve \(1952\)](#).

⁵As a reference, Jupiter induces a 12 m s^{-1} radial velocity signal on the Sun with a periodicity of 12 years.

In April 1994, Michel Mayor and Didier Queloz started a systematic search for brown dwarfs or giant planets in a survey of 142 solar-type stars using the ELODIE spectrograph (Baranne et al. 1996). This work would finally lead to the unambiguous detection of the first exoplanet orbiting a normal star: 51 Peg b (Mayor & Queloz 1995). This was, however, not the first detection of a planet outside the Solar System as three years before the radio astronomers Aleksander Wolszczan and Dale Frail have detected unusual sinusoidal variations in the period of the millisecond pulsar PSR 1257+12. They attributed this changes to the presence of two terrestrial-mass planets in the system (Wolszczan & Frail 1992). The discovery of one Jupiter-like planet orbiting with a period of 4.2 days and also two terrestrial-mass planets around a pulsar provided the first evidence that planets could be very different from the ones in the Solar System.

The discovery of 51 Peg b was, however, taken with skepticism by some astronomers as the planet formation theories at the time had not predicted the existence of such close-in planets. Some studies wondered if the RV signal could be attributed to non-radial pulsations (Hatzes et al. 1997) or an unknown mode of stellar oscillations (Gray 1997). It was not until the detection of the first multiplanetary system (Butler et al. 1999) and the first transiting planet (Charbonneau et al. 2000; Henry et al. 2000) that the interpretation of these RV signals was generally accepted as caused by planetary bodies. Since then on, the field of exoplanets was born leading to the discovery of more than 3000 extrasolar planets⁶, which has revolutionized our understanding of how planets form and evolve in our galaxy.

1.2 Tools and techniques for exoplanet detection

The field of exoplanets has grown exponentially during the last decade. It is now quite usual to hear about new planets being discovered on a monthly/weekly basis. It seems logical to me to start with the tools and methods that made possible this avalanche of planet discoveries during the past 20 years. I will mainly focus on two techniques that have been the most successful ones and are also the most relevant to this thesis work: radial velocity and transits.⁷

1.2.1 Radial velocity

The radial velocity technique established the foundation for the exoplanet research, as it was with this technique that the first exoplanet orbiting a Sun-like star was discovered (Mayor & Queloz

⁶As of October 2016 based on <http://exoplanetarchive.ipac.caltech.edu>

⁷For descriptions and details on other exoplanet detection techniques, like direct imaging, microlensing and astrometry, I refer the reader to the following papers and books: Wright & Gaudi (2013), Perryman (2011), Perryman et al. (2014), Fischer et al. (2014), Gould (2016), Claudi (2016), Bowler (2016).

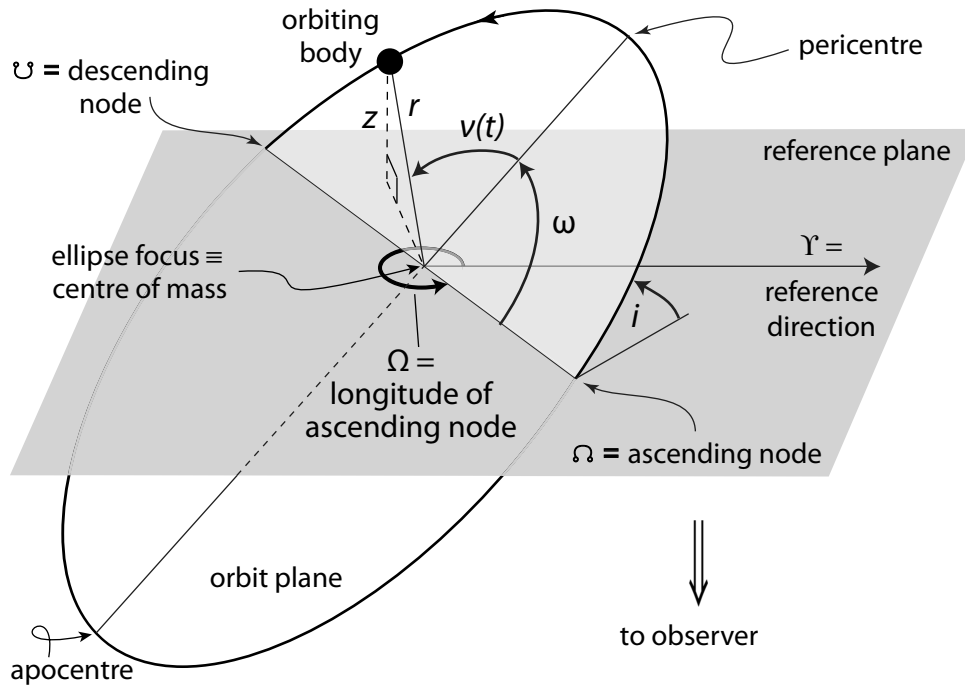


Figure 1.2: Three-dimensional representation of a Keplerian elliptical orbit. Figure taken from [Perryman \(2011\)](#).

1995). The method is based on measuring the velocity change of a star along the line-of-sight that is caused by the gravitational influence of a body, in this case a planet, orbiting around it.

1.2.1.1 Keplerian orbits

The motion of two spherical bodies (point masses) acting solely under the influence of gravitational forces is described by Keplerian orbits. Generally, the orbit of a body is represented in a two-dimensional plane by either an ellipse, parabola or hyperbola. For the case of planetary motion, the basic elements of a Keplerian orbit are shown in Fig. 1.2. These include:

- *Reference plane:* This is the plane tangent to the celestial sphere.
- *Line of nodes:* line segment defined by the intersection between the reference plane with the orbital plane.

- *Descending node*: point in the orbit where the planet crosses the reference plane in the direction towards the observer.
- *Ascending node*: point in the orbit where the planet crosses the reference plane in the direction away from the observer.
- *Longitude of ascending node*: angle between the vernal equinox (reference direction) and the ascending node. It defines the orientation of the orbit in the sky.

The full parametrization of a Keplerian orbit requires seven parameters: Two elements that define the shape and size of the ellipse:

- a : semi-major axis that defines the long axis of the elliptical orbit.
- e : eccentricity that describes the degree of elongation of the orbit with respect to a circle

Three elements that define the orientation of the orbital plane in which the ellipse is embedded:

- ω : argument of periastron that is the angle measured from the ascending node to the pericentre.
- i : orbital inclination that is the vertical tilt of the ellipse with respect to the reference plane, measured at the ascending node.
- Ω : longitude of ascending node.

And two additional parameters:

- P : orbital period that is related to a and the component masses through Kepler's third law.
- T_0 : a reference time that generally is taken to be the time of periastron passage.

Radial velocity measurements can determine all of these parameters except for two: Ω and i . This is particularly relevant as, how it will be shown later, the non-determination of the orbital inclination, i , implies that we can only derive a lower limit for the planet mass. This is because we measure one component of the star's motion – along the line-of-sight – and consequently, we can determine only the planet mass times the sine of the orbital inclination.

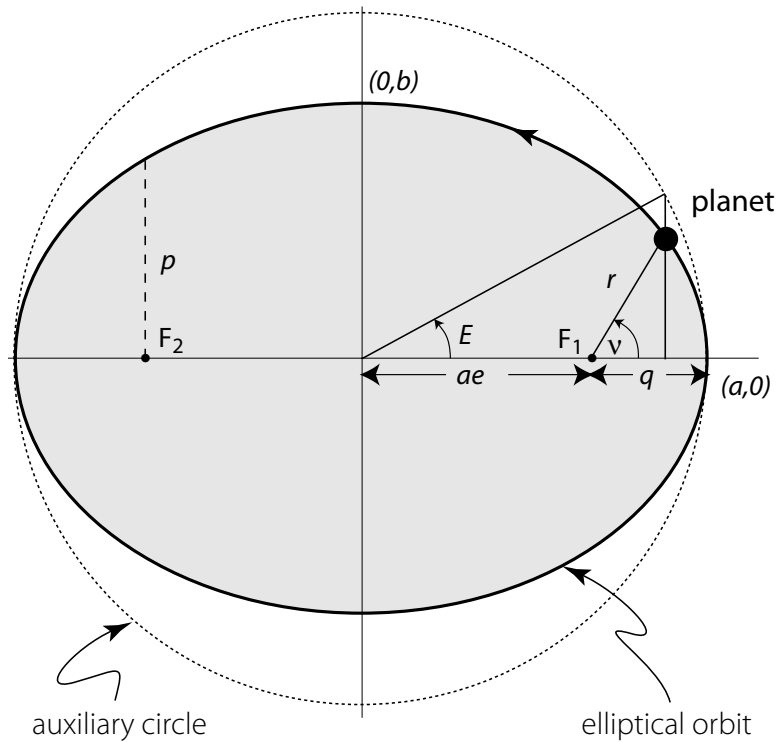


Figure 1.3: Representation of an elliptical orbit of planetary motion. The auxiliary circle has a radius equal to the semi-major axis a . The semi-minor axis is b . The true anomaly ν describes the points on the elliptical orbit at a certain time. Alternatively, the points in the ellipse can be also described by the eccentric anomaly E . The focus of the ellipse is F_1 , which also represents the system barycenter. Figure taken from [Perryman \(2011\)](#).

1.2.1.2 Description of orbital motion

In Keplerian orbits the star and the planet move around the center of mass, or barycenter, on elliptical orbits where the barycenter is at the focus of the ellipse. Figure 1.3 shows the elements of an elliptical orbit. Taken this Figure as a reference, the ellipse can be represented in polar coordinates (with respect to a focus) by the expression:

$$r = \frac{a(1 - e^2)}{1 + e \cos \nu} \quad (1.1)$$

where ν is the true anomaly that describes the position of the planet along the trajectory measured from the pericentre of the ellipse at a certain time. The eccentricity, e , is related to the semi-major axis, a , and semi-minor axis, b , by:

$$b^2 = a^2(1 - e^2) \quad (1.2)$$

For the calculation of the orbital motion of a body there are two additional angles, besides the true anomaly, that are particularly important: the eccentric anomaly, E , and the mean anomaly, M ⁸. The eccentric anomaly is the angle between the direction of the pericentre and the position of the planet, but referred to the auxiliary circle (see Fig. 1.3) that has a radius equal to the semi-major axis a . The true and eccentric anomaly are related geometrically by:

$$\cos \nu(t) = \frac{\cos E(t) - e}{1 - e \cos E(t)} \quad (1.3)$$

The mean anomaly is an angle relating time and position of a planet moving through the fictitious auxiliary circle (see Fig. 1.3) that can be used to calculate the true anomaly. For eccentric orbits the planet does not move at a constant rate over an orbit. However, we can define a time-averaged angular velocity over an orbit as $n = 2\pi/P$. Thus, the mean anomaly with respect to an arbitrary time reference, t_0 , is defined by:

$$M(t) = \frac{2\pi}{P}(t - t_0) \quad (1.4)$$

The relation between the mean anomaly, $M(t)$, and the eccentric anomaly, $E(t)$, is given by Kepler's equation:

$$M(t) = E(t) - e \sin E(t) \quad (1.5)$$

What is generally done to calculate the orbit of an orbiting body is, first, get the position of the planet (mean anomaly) at a certain time, t , using Equation 1.4. Then, solve for $E(t)$ in the transcendental Kepler's equation. Finally, Equation 1.3 is used to obtain the true anomaly $\nu(t)$.

1.2.1.3 Radial velocity curve

Referring to Fig. 1.2, we can define the position of the star moving around the barycenter of the system⁹ (instead of the planet). The star position projected onto the line-of-sight can be derived from trigonometry:

⁸These angles are called anomalies because for a long time the movement of the planets in the celestial sphere was considered anomalous.

⁹We do this because what we measure are the small changes in the radial velocity of the star, not the planet.

$$z = r(t) \sin(\nu + w) \sin i \quad (1.6)$$

where $r(t)$ is the distance from the barycenter. Then, to calculate the velocity in the direction of the observer we have to take the time derivative of $z(t)$:

$$v_r = \frac{dz}{dt} = [\dot{r} \sin(\nu + w) + r\dot{\nu} \cos(\nu + w)] \sin i \quad (1.7)$$

The equation above is not so useful, as it still includes the time derivatives of the position, \dot{r} , and true anomaly, $\dot{\nu}$. To obtain a more practical expression for the RV equation we have to use Kepler's second law and the representation of an ellipse in polar coordinates. Referring to Figure 1.3, a planet moving by a small angle $d\nu$ will sweep out an area $1/2r^2d\nu$ in a time dt . Kepler's second law states that the line joining the planet and star (radius vector) sweeps out equal areas in equal times, thus we can write the following expression:

$$r^2 \frac{d\nu}{dt} = \frac{2\pi a^2 \sqrt{1 - e^2}}{P} \quad (1.8)$$

where we have used the fact that the total area of an ellipse is $\pi a \sqrt{1 - e^2}$ which is covered by the orbiting body in a period, P . Then, using the previous equation together with equation 1.1, we can eliminate the time derivatives and write:

$$v_r = K[\cos(\nu + w) + e \cos w] \quad (1.9)$$

where the RV semi-amplitude, K , is defined by:

$$K = \frac{2\pi a_\star \sin i}{P \sqrt{1 - e^2}} \quad (1.10)$$

The previous expression for K can be rewritten in a more convenient way by using Kepler's third law:

$$K = \left(\frac{2\pi G}{P} \right) \frac{M_p \sin i}{(M_\star + M_p)^{2/3}} \frac{1}{\sqrt{1 - e^2}} \quad (1.11)$$

where M_p is the planet mass, M_\star is the stellar mass and G is the gravitational constant. This form of the RV semi-amplitude is particularly useful as it allows to derive the planet (minimum) mass with RV observations.

1.2.1.4 Calculation of Doppler shifts

The calculation of RVs relies on the Doppler effect (Doppler 1842; Fizeau 1848, 1870): as the star moves away from the observer, the light it emits is redshifted and when it moves towards the observer there is a blueshift effect. When we observe a star with a spectrograph, this effect results in a periodic shift of spectral lines, which in turn are used to derive the RV. The physical shift, in pixels, at the detector is extremely small. For instance, for a resolving power of $R = 100,000$ the resolution will be 0.05 \AA at 5000 \AA . In a good spectrograph this corresponds to a dispersion of 0.025 \AA/pixel , which results in a velocity resolution of 1500 m s^{-1} per CCD pixel. Thus a Jovian planet causing a 10 m s^{-1} Doppler shift translates to a change in the position of a spectral line of 0.0067 pixels. A typical CCD pixel has a size of around $15 \text{ }\mu\text{m}$, therefore the shift of the spectral line in the focal plane is 10^{-4} cm . For a 1 m s^{-1} Doppler shift this is a factor of 10 smaller. This means that if care is not taken to make a stable, both thermal and mechanical, spectrograph then instrumental shifts can make the detection of giant exoplanets very difficult. The key to overcome these problems is to record simultaneously the calibration and stellar spectra. The two more successful methods to accomplish that are described below.

The gas cell method: The idea of this method is to use a controlled gas cell that absorbs certain known wavelengths of the incoming stellar spectra. The absorption lines are not found in the stellar spectra or in the spectrum of the Earth's atmosphere. The gas that is typically used for this purpose is molecular iodine (I_2), that presents several advantages; it is a relatively benign gas that can be permanently sealed. It has useful absorption lines in the wavelength range $5000\text{-}6000 \text{ \AA}$. The typical path length of the I_2 cell is a few cm, thus the cell can be easily put in front of the spectrograph slit. The high density of spectral I_2 absorption lines can be used to model the instrumental profile of the spectrograph.

The first I_2 cells were used by Beckers (1976) and Koch & Woehl (1984) for solar observations. Later, Marcy & Butler (1992) used a I_2 cell for their high precision RV survey at the Lick Observatory. To model the stellar spectrum through the I_2 cell, $I(\lambda)$, two functions are used; the intrinsic stellar spectrum $S(\lambda)$, and the transmission function of the I_2 cell, $T(\lambda)$:

$$I(\lambda) = k[T(\lambda)S(\lambda + \Delta\lambda)] \otimes IP \quad (1.12)$$

where k is a normalization factor, $\Delta\lambda (= \lambda\Delta v/c)$ is the stellar Doppler shift and IP is the instrumental profile of the spectrograph. The symbol \otimes denotes the convolution. To derive the I_2 transmission function, $T(\lambda)$, usually a fully resolved and oversampled spectrum of the iodine cell is taken with a Fourier transform spectrometer (FTS). The intrinsic stellar spectrum, $S(\lambda)$ is more difficult to obtain as in the process of observation this template spectrum has already been convolved with the IP of the spectrograph. To overcome this, a stellar spectrum is observed and

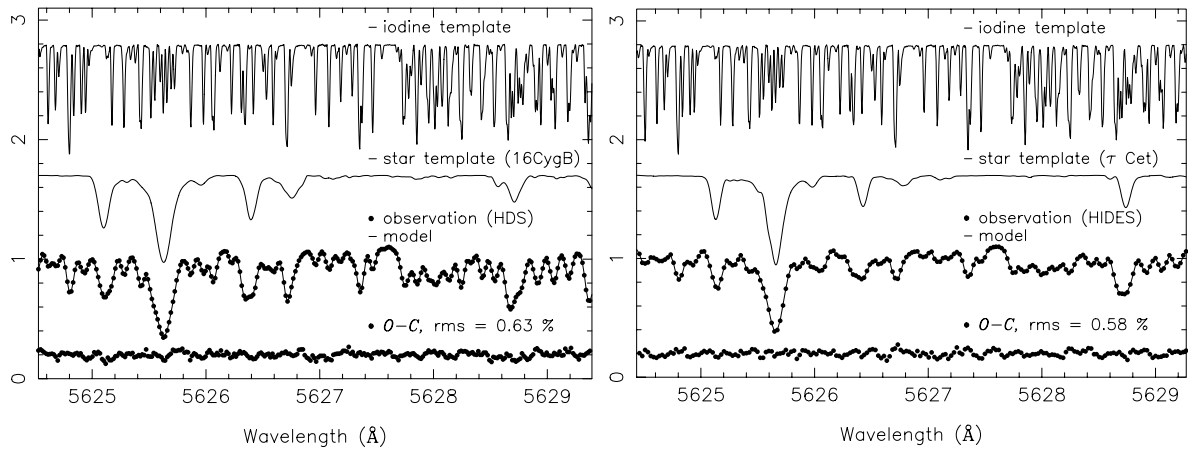


Figure 1.4: Examples of the modeling of the stellar spectrum and the I_2 cell for the stars 16 Cyg B (left panel) and τ Cet (right panel). The plots show the I_2 template spectrum, the star template spectrum, the observed spectrum taken through the I_2 cell (dots) together with the model (solid line), and the residuals from the fit (5 times the difference between the model and the observation). The observation is modeled as the product of the I_2 and stellar template spectra convolved with the derived instrumental profile of the spectrograph using Equation 1.12. Figure taken from [Sato et al. \(2002\)](#).

is later deconvolved using the reconstructed IP from observations of a rapidly rotating B-star passing through the I_2 cell¹⁰ (e.g., [Butler et al. 1996](#); [Endl et al. 2000](#)). The calculation of the IP involves the fitting of multiple Gaussians, in which the central one is kept at a fixed position and constant amplitude, while the other, satellite, Gaussians are allowed to vary in position and/or amplitudes and widths (e.g., [Valenti et al. 1995](#)).

To calculate the stellar RV each spectral order is divided into several chunks and then equation 1.12 is solved iteratively. Usually the number of free parameters are within 10-15 (depending on the number of Gaussians), including the Doppler shift that is used to derive the RV. The final RV is the average of the RV obtained for each individual chunk. The precision reached by this method is $\sim 3 \text{ m s}^{-1}$ (e.g., [Butler et al. 1996](#); [Vogt et al. 2000](#); [Butler et al. 2001](#)). Figure 1.4 illustrates the modeling of the spectrum of the stars 16 Cyg B and τ Cet using the iodine method.

Thorium-Argon method: This technique consists in recording the stellar spectrum at the same time as a standard calibration spectrum using a Thorium-Argon (ThAr) lamp. Each of these spectra is recorded using one of the two optical fibers feed to the spectrograph: the object and reference fibers. Thus the stellar spectrum is recorded on the CCD adjacent to the calibration

¹⁰These stars have few shallow spectral features due to the stellar rotation, thus what is essentially observed is the spectrum of the I_2 cell. The advantage of doing this is that the iodine spectrum is taken through the same optical path as the template stellar spectrum.

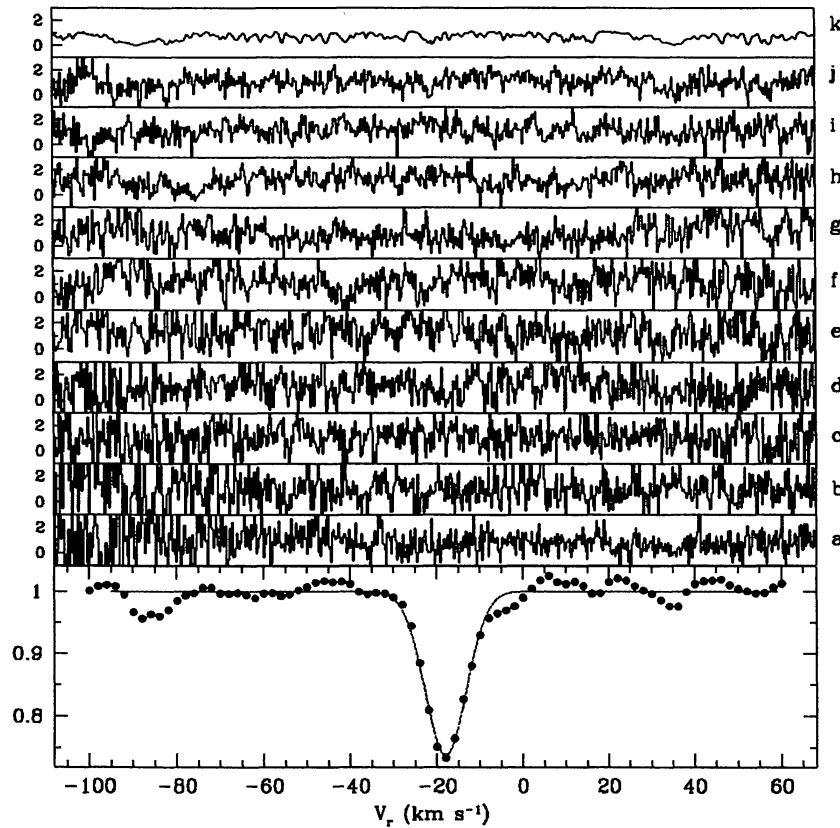


Figure 1.5: Cross-correlation function for a K0 III star with a $S/N = 1$. The spectral resolution is $R = 40\,000$ spanning the range $4110 - 4440 \text{ \AA}$ in ten orders (letters *a* to *j*). The top panel is the same order as the one below, but with a $S/N = 40$. The lower panel shows the derived cross-correlation function. Figure taken from [Queloz \(1995\)](#).

spectrum, therefore any instrumental shifts will affect both in the same way. What is typically done is to take a spectrum of a ThAr lamp at the beginning of the night (using both fibers) to determine a wavelength solution, that is, map the different wavelengths to values of pixels in the CCD: $\lambda(x, y)$ with (x, y) pixel coordinates. Typically, this wavelength solution remains valid for the whole night. The calibration spectra taken simultaneously with the stellar spectrum are used to trace any instrumental drift that may occur during the night.

This method is used by the high accuracy radial velocity planetary searcher (HARPS; [Pepe et al. 2000](#)) and can reach an RV precision of 1 m s^{-1} . The stellar RVs are derived by cross-correlating the stellar spectrum with a numerical mask adapted to the spectral type of the star. The use of the cross-correlation technique to calculate RVs was first suggested by [Fellgett \(1955\)](#) and later, demonstrated by [Griffin \(1967\)](#). The cross-correlation function (CCF) for a particular echelle order k at a certain value of the velocity v_r can be defined as:

$$CCF_k(v_r) = \frac{1}{R} \int_{\lambda_i}^{\lambda_f} S(\lambda)M(\lambda')d\lambda \quad (1.13)$$

where R is a normalization constant, $S(\lambda)$ is the stellar spectrum, and $M(\lambda')$ is a binary mask shifted to a position defined by $\lambda' = \lambda(1 + v_r/c)$. The different CCFs are then summed for all the orders typically weighting by the S/N of each order. As defined by the previous equation, the CCF will have a minimum for the value of v_r that is close to the stellar radial velocity. Then the final RV is derived from a Gaussian fit to CCF, where the mean is taken to be the stellar RV. There are several ways to define the template mask M to calculate the CCF; one can take a single observation of the star and then cross-correlate all the other spectra with this one. This guarantees an excellent match to your spectra, but can introduce some noise to the CCF. Alternatively, one can co-add all the stellar spectra to generate a master, high S/N spectrum to use as template (e.g. [Anglada-Escudé & Butler 2012](#)). Also, one can create a binary mask, adapted to the spectral type of your star, that is noise free. This mask has regions of 0 and 1 where the non-zero values correspond to the theoretical positions and widths of the stellar absorption lines at zero velocity (e.g. [Pepe et al. 2002](#)). One advantage of using the CCF to derive RVs is that it can be quite sensitive to Doppler shifts even with low S/N data. This can be appreciated in Figure 1.5 where the peak (minimum value) of the CCF is clearly visible when data with a S/N=1 is used.

Other methods: None of the previously described spectral reference sources (ThAr spectral lamps and iodine cells) would provide a spectrum sufficiently wide, rich, stable and uniform for the purpose of assigning to each pixel the correct wavelength with a repeatability of the order of $\Delta\lambda/\lambda \approx 10^{-10}$. A promising method for achieving this is the use of a laser frequency comb (LFC; see [Murphy et al. 2007](#)). A LFC emits a spectrum of lines that are equally spaced according to the laser's pulse repetition rate, whose absolute frequencies are known a priori with a relative precision better than 10^{-12} . A LFC has been installed in the HARPS spectrograph (see [Lo Curto et al. 2012](#); [Wilken et al. 2012](#)) and recently, a near-infrared LFC has been developed around $1.55 \mu\text{m}$ demonstrating a stability of $< 200 \text{ kHz}$ in the lab, corresponding to a Doppler precision of $\sim 0.3 \text{ m s}^{-1}$ ([Yi et al. 2016](#)). A similar, and more economical alternative to LFCs is the use of Fabry-Pérot interferometers to produce an optimal and regularly spaced set of calibration lines covering all orders of the spectrograph (see [Wildi et al. 2010](#); [Schäfer & Reinerts 2012](#); [Reinerts et al. 2014](#); [Schwab et al. 2015](#); [Bauer et al. 2015](#)).

1.2.2 Photometric transit

Under the right geometrical configuration, the brightness of a star may be periodically decreased as a consequence of a body orbiting around it. This is known as a photometric transit. The first suggestion to look for planets using this phenomenon was done by [Belorizky \(1938\)](#) stating

that transiting exo-Jupiters could be detected with photo-cells on existing telescopes at that time. This study was ignored, but later revived by [Struve \(1952\)](#), who calculated that the projected eclipse area of a Jovian planet would be about 1/50th of that of the star, and the decrease in magnitude of ~ 0.02 . The first detailed description of the method was done by [Rosenblatt \(1971\)](#), who proposed to monitor the brightness variations of stars and color changes produced by limb darkening using a network of telescopes. Major developments were later done by [Borucki & Summers \(1984\)](#) and by [Hale & Doyle \(1994\)](#).

The *a-priori* probability of observing a planet transiting its star is a function of the orbital parameters as well as the planet and stellar radius ([Stevens & Gaudi 2013](#)):

$$P_{tr} = \left(\frac{R_{\star} + R_p}{a} \right) \left(\frac{1 + e \sin \omega}{1 - e^2} \right) \quad (1.14)$$

where R_{\star} is the stellar radius, R_p is the planet radius, a the semi-major axis, e the eccentricity and ω is the angle at which orbital periastron occurs, such that $\omega = 90^\circ$ indicates a transit. A typical hot Jupiter with a period of $P \sim 3$ days, orbiting a solar-type star has a photometric transit depth of $k \sim 1\%$ and $P_{tr} \sim 10\%$. The super-Earth and sub-Neptune population of planets presents $k \sim 0.1\%$ and $P_{tr} \sim 2.5\%$. For comparison, an Earth-sized planet in an Earth-like orbit around a solar-type star would have $k \sim 0.01\%$ and $P_{tr} \sim 0.5\%$.

1.2.2.1 Description of light curves

Figure 1.6 illustrates the four main observables that characterize a primary transit: the transit depth, ΔF , the period, P , the total transit duration, t_T , and the time between the second and third contact, t_F . These parameters can be geometrically expressed in three equations that describe the principal features of a transit light curve for circular orbits ([Seager & Mallén-Ornelas 2003](#)):

$$\Delta F \simeq \left(\frac{R_p}{R_{\star}} \right)^2 \quad (1.15)$$

$$t_T = \frac{P}{\pi} \arcsin \left(\frac{R_{\star}}{a} \left\{ \frac{(1 + \sqrt{\Delta F})^2 - b^2}{1 - \cos^2 i} \right\}^{1/2} \right) \quad (1.16)$$

$$\frac{\sin(t_F \pi / P)}{\sin(t_T \pi / P)} = \left\{ \frac{(1 - \sqrt{\Delta F})^2 - b^2}{(1 + \sqrt{\Delta F})^2 - b^2} \right\}^{1/2} \quad (1.17)$$

where we have defined the impact parameter $b = (a/R_{\star}) \cos i$ (see Fig. 1.6). In practice, Equation 1.15 overestimates the ratio of areas when the non-uniformity of the stellar disk is not considered.

This phenomenon is known as limb darkening where the outer parts of the stellar disk appear darker than the center. This results from a combined effect of optical depth with the decreasing star density and temperature with radius. It is typically parametrized by functions of $\mu = \cos \theta$, where θ is the angle between the normal to the stellar surface and the line-of-sight to the observer. A general expression for a non-linear law of the radial dependence of the specific intensity is given by:

$$I(\mu) = 1 - \sum_{n=1}^4 c_n (1 - \mu^{n/2}) \quad (1.18)$$

where the coefficients c_n depend on the stellar effective temperature, surface gravity and metallicity. The linear and quadratic laws are recovered when $c_1 = c_3 = 0$ and $c_1 = c_3 = c_4 = 0$, respectively. Theoretical values of the limb darkening coefficients have been compiled by [Claret \(2003, 2004\)](#) and more recently, by [Sing \(2010\)](#) and [Claret & Bloemen \(2011\)](#). The most commonly used parametrization for limb darkening is that of [Mandel & Agol \(2002\)](#), though the recent treatment of [Giménez \(2006\)](#) and [Pál \(2008\)](#) present improved numerical stability and precision in some cases.

The fraction of the stellar light that is blocked by a planet during a transit depends on the inclination of the orbit with respect to the line-of-sight, the photospheric limb darkening profile and the planet-to-star area ratio. The key parameters that define the flux deficit at any time during a transit are the projected separation of the centers of the planet and the star, $z = d/R_\star$, and the radius ratio between the planet and the star, $p = R_p/R_\star$. Given a set of photometric measurements at certain times, the procedure for fitting a transit model involves adopting a set of limb darkening coefficients for the appropriate passband (or let them float in the fitting, see [Espinoza & Jordán 2015](#)), a value for the parameter p , and compute the projected separation of centers $z(t)$ at each time t , that for circular orbits is given by:

$$z(t) = \frac{a}{R_\star} [(\sin \omega_f t_c)^2 + (\cos i \cos \omega_f t_c)^2]^{1/2} \quad (1.19)$$

where ω_f is the orbital frequency, i the orbit inclination and t_c the time measured from the center of the transit. The output is generally an array of flux ratios $F(t)/F_0$, where F_0 is the stellar flux outside the transit.

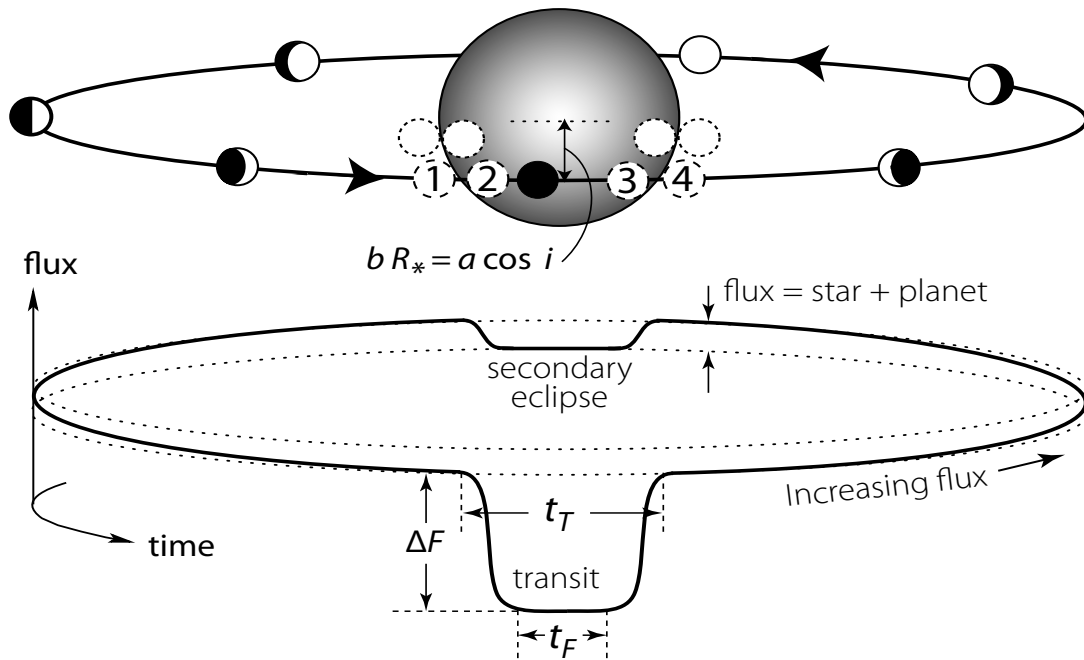


Figure 1.6: Schematic diagram showing a planetary transit. During the transit, the planet blocks a fraction of the star light. After the transit, the planet’s brighter day-side progressively comes into view, and the total flux rises. It drops again during the secondary eclipse as the planet passes behind the star. In the upper plot are shown the contact points (one to four) for a smaller impact parameter b (dotted circles) and a larger value of b (dashed circles). For smaller b , the circles are more closely separated in time, and the ingress/egress slopes correspondingly steeper. The total transit duration t_T is between first and fourth contact, while t_F is timed between second and third contact. Figure from Winn (2009) adapted by Perryman (2011).

1.2.2.2 Light curve modulations

The planet passing in front of the star is the most prominent feature of the transit light curve. However, there are other more subtle effects that can also be imprinted on the photometric curve, particularly flux modulations in the out-of-transit regions. These phenomena are known to be caused by (1) reflected/emitted light from the planetary companion (e.g. Seager et al. 2000; Sudarsky et al. 2003), (2) ellipsoidal variations induced by the planet on the star (Morris 1985; Mazeh 2008), and (3) Doppler beaming due to the reflex motion of the star induced by the presence of a massive close-in companion (Maxted et al. 2000; Loeb & Gaudi 2003; Zucker et al. 2007).

Reflected/emitted flux: When the planet is at the appropriate orbital phase, it starts to reflect the stellar light in the direction to the observer. The amount of reflected flux is a function of the planet size (R_p) and distance from the star (a), the planet phase function (Φ) and the fraction of the star light that is reflected by the atmosphere of the planet or planetary albedo (A_g). The reflected light from the planet is given by:

$$\left(\frac{\Delta F}{F}\right)_{\text{ref}} = A_g \left(\frac{R_p}{a}\right)^2 \Phi(\alpha) \quad (1.20)$$

where the phase function $\Phi(\alpha)$ is usually taken to be that of a Lambertian sphere ([Lambert 1760](#); [Russell 1916](#); [Sobolev 1975](#)):

$$\Phi(\alpha) = \frac{\sin \alpha + (\pi - \alpha) \cos \alpha}{\pi} \quad (1.21)$$

where α is the angle between the line-of-sight and the star-planet direction. Alternatively, one can define a different form of the phase function to model the reflected emission (e.g. [Faigler & Mazeh 2015](#)).

Ellipsoidal variation: the ellipsoidal modulation is produced by the gravitational influence of the planet that induces tides on the star surface. Thus the star deviates from a spherical form and the brightness varies as a function of the visible surface area. [Pfahl et al. \(2008\)](#) studied the oscillation modes induced in the star by a low-mass companion. The tidal modulation can be described by a sum of harmonics terms, and for small eccentricities, only the first harmonic ($l = 2$) is relevant. Thus, the flux variation due to ellipsoidal modulation is given by:

$$\left(\frac{\Delta F}{F}\right)_{\text{ellip}} = -\alpha_e \frac{M_p}{M_\star} \left(\frac{R_\star}{a}\right)^3 \left(\frac{1 + e \cos \nu}{1 - e^2}\right)^3 \sin^2 i \cos 2\alpha \quad (1.22)$$

where the parameter α_e depends on the linear limb darkening (u) and gravity (g) coefficients as introduced by [Morris \(1985\)](#):

$$\alpha_e = 0.15 \frac{(15 + u)(1 + g)}{3 - u} \quad (1.23)$$

For a more detailed description of this effect, including higher harmonic terms see [Lillo-Box et al. \(2016a\)](#).

Doppler beaming: this effect is a consequence of the reflex motion of the star that modulates the rate of photons, shifts the stellar spectrum and beams the photons in the direction of motion. That

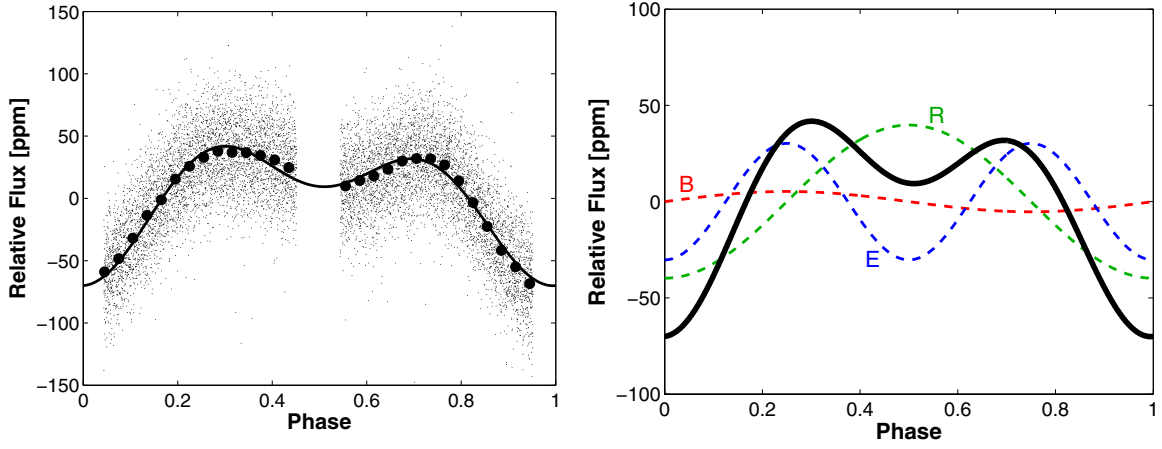


Figure 1.7: Example of the phase folded light curve of the planet-hosting star KOI-13. The left panel shows the *Kepler* long cadence data (grey dots), the binned data (black points) and the corresponding sinusoidal model constructed taking into account the effects of the out-of-transit modulations (solid line). The right panel illustrates the relative contribution of the three effects modeled: beaming (B), ellipsoidal (E) and reflection (R). The solid black line is the fitted double harmonic model, which is the sum of the three effects. Figure taken from [Shporer et al. \(2011\)](#).

is, the angular distribution of stellar flux will be beamed in the direction of the star's velocity vector (see [Rybicki & Lightman 1979](#)). This effect is bolometric and results in an observed periodic brightness change proportional to the star's radial velocity. For a star moving at a radial non-relativistic velocity relative to the observer, the expression for the Doppler beaming is given by:

$$\left(\frac{\Delta F}{F}\right)_{\text{beam}} = (3 - \Gamma) \frac{K}{c} \sin(\alpha + e \cos \omega) \quad (1.24)$$

where c is the speed of light, K is the RV semi-amplitude, ω the argument of pericenter, and the parameter Γ is defined by [Loeb & Gaudi \(2003\)](#) as:

$$\Gamma = \frac{e^x(3 - x) - 3}{e^x - 1} \quad (1.25)$$

where $x = hc/(k_B \lambda T_{\text{eff}})$. Here h is the Planck constant, k_B is the Boltzmann constant, λ is the effective wavelength, and T_{eff} is the effective stellar temperature. For a more general treatment of the definition of Γ see [Bloemen et al. \(2011\)](#).

1.2.2.3 Bayesian modeling

Once the transit and/or radial velocity models are available for generating synthetic fluxes and RVs at a set of observation times, the physical parameters of the system can be obtained by fitting these models to the data. In the case of transits, assuming circular orbits and limb-darkening coefficients fixed, the sequence of data is fully described by a model with five parameters R_p/R_\star , a/R_\star , the orbital period P , the impact parameter b , and epoch of mid-transit T_0 . In a more general way, given a set of data, we want to infer the values of the model parameters. In practice, what we are really interested in is finding how likely all possible solutions are. This is equivalent to ask: Given the data, what is the posterior probability density function (PDF) over the model parameters? To answer this question we can use Bayes' theorem (Bayes 1763; Laplace 1812; Jeffreys 1973) and set up a model, for some data D . The model can contain one or more parameters denoted by θ . Bayes's theorem associates the probability of the parameters given the data to the probability of the data given certain values of the parameters. The posterior PDF is defined as:

$$P(\theta | D) = \frac{P(D | \theta)P(\theta)}{P(D)} \quad (1.26)$$

The first term in the numerator is called the likelihood. This gives the probability of observing the data D when the model parameters have the values θ . It is often referred as the likelihood function to stress that it is a function of the model parameters. The second term in the numerator is called the prior. It is the information that we have, independently of the data, about the possible values of the model parameters. Sometimes the prior information is vague, or can be difficult to express it as a prior probability distribution. Different choices of priors are the uniform prior, Gaussian prior, or Jeffreys prior (Jeffreys 1961). The denominator is sometimes called the evidence, but for all practical purposes is a normalization constant.

If the observational errors are assumed to be Gaussian and independent, the likelihood is given by:

$$\mathcal{L} = P(D | \theta, M) = \prod_i \frac{1}{2\pi\sigma_i} \exp\left(-\frac{(D_i - f(\theta, t_i))^2}{2\sigma_i^2}\right) \quad (1.27)$$

where σ_i is the data uncertainty, and we have defined that the model is described by a function f that depends on the parameters θ and time t . Evaluating the product and taking the natural logarithm we obtain the log likelihood, which is convenient as it transforms the product into a sum of terms:

$$\ln \mathcal{L} = -\frac{N}{2} \ln(2\pi) - \sum_i^N \left(\frac{\ln \sigma_i^2}{2} + \frac{(D_i - f(\theta, t_i))^2}{\sigma_i^2} \right) \quad (1.28)$$

where N is the number of data points. As shown by equation 1.26, the posterior $P(\theta | D)$ is proportional to the product of the likelihood and the prior. Once we have defined the prior and likelihood, and we have measured some data, the posterior gives us the PDF over the parameters. To get the PDF of a particular parameter, θ_1 , we have to marginalize (integrate) the posterior over the rest of the model parameters:

$$P(\theta_1) = \int_{\theta} P(\theta_1 | \theta) P(\theta) d\theta \quad (1.29)$$

Over the last decade, it has become the standard in astronomy to use Markov-chain Monte Carlo methods (MCMC, see [Tanner & Wong 1987](#)) to determine the posterior probability distribution of the set of parameters θ (e.g. [Ford 2006](#); [Balan & Lahav 2009](#); [Schulze-Hartung et al. 2012](#); [Eastman et al. 2013](#)). What is usually done is to generate samples from the posterior distribution according to some rule. You can start from an initial state vector of parameters θ , and propose to move (jump) from that position somewhere else. For instance, the Metropolis sampler ([Metropolis & Ulam 1949](#); [Metropolis et al. 1953](#)) takes a sample from a normal distribution centered around the current state vector with a certain standard deviation that will determine how far to move. If the resulting distribution with that proposed new state vector explains the data better (that is the likelihood is higher) than your old vector, then the jump is made. A generalization of this algorithm, known as the Metropolis-Hasting rule, was made by [Hastings \(1970\)](#). This is the standard sampler that most people use at these days.

1.2.2.4 Kepler mission

The *Kepler* space telescope ([Borucki et al. 2010](#)) monitored $\approx 150,000$ FGKM dwarf stars for four years and was particularly sensitive to planets as small as Earth with periods close to one year. The analysis of the data to date has allowed to detect over 4600 planetary candidates, which include several hundred Earth-size planetary candidates, over three thousand confirmed planets, and also Earth-size planets in the habitable zone ([Borucki 2016](#)). Between July and May 2012, two of Kepler's four gyroscope-like reaction wheels failed, which prevented the accurate pointing of the spacecraft. This marked the end of a mission that made important contributions to the exoplanet science as described below.

Thanks to the *Kepler* mission it was possible to establish that the frequency of exoplanets increases for smaller size and that there are more close-in Neptune and Super-Earths than Jupiter-

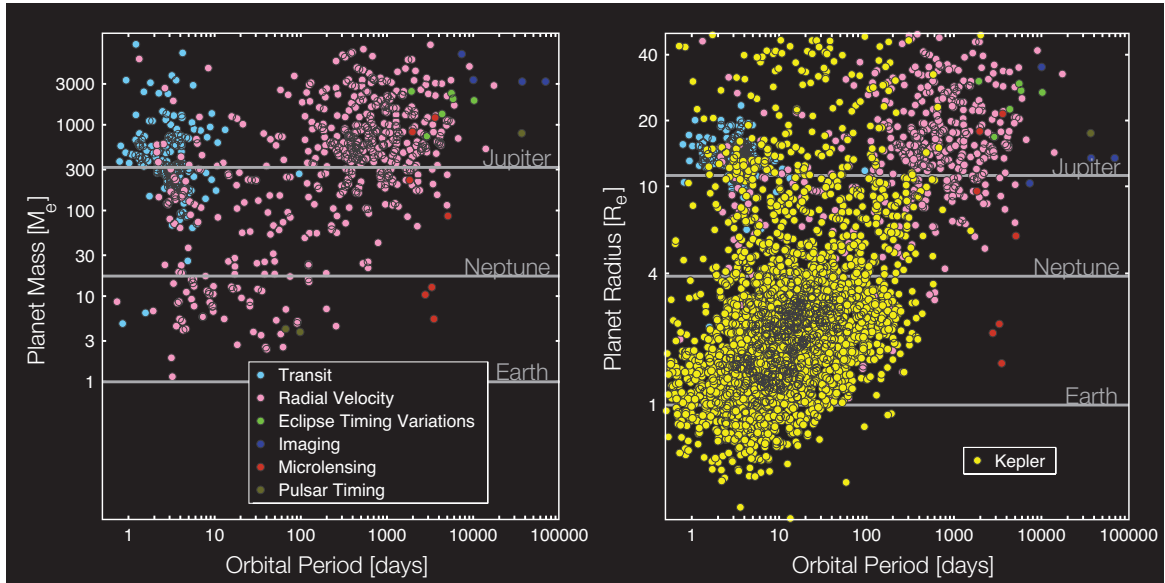


Figure 1.8: The left panel shows the planet mass versus orbital period for the non-Kepler discoveries color-coded according to the detection technique. The same planets are plotted in the left panel where the mass-radius relation from [Lissauer et al. \(2011\)](#) has been used to transform planet mass to radius. Additionally, all the *Kepler* discoveries (yellow) are added for comparison. 86% of the non-Kepler planets are larger than Neptune while the inverse is true for the *Kepler* discoveries: 85% of the *Kepler* planets are smaller than Neptune. Figure taken from [Batalha \(2014\)](#).

sized planets ([Borucki et al. 2011](#); [Fressin et al. 2013](#); [Howard 2013](#); [Petigura 2013](#)). More than half of the planet candidates found by *Kepler* are 1–3 times the size of Earth and take less than 100 days to orbit their stars ([Batalha 2014](#), see Fig. 1.8). Additionally, it demonstrated that the occurrence rate of exoplanets depends on the spectral type of the host star, with smaller planets being more abundant around smaller stars ([Howard 2012](#); [Mulders et al. 2015](#)). These results are in agreement with the previous findings of Doppler surveys around M dwarfs ([Endl et al. 2006](#); [Bonfils et al. 2013](#); [Montet et al. 2014](#)).

The *Kepler* mission also found that approximately 30% of late-type stars have densely packed multiple planet systems. Candidate planets belonging to systems with two or more transiting planets appear to orbit close to the same plane, thus with mutual inclinations similar to our Solar System ([Fabrycky et al. 2014](#)). These systems have circular orbits with eccentricities of only a few percent, which is similar to our Solar System, but small compared to the eccentricities observed in most exoplanets with periods of more than ~ 10 days. Another important result obtained by *Kepler* is that stars with only one transiting planet harbor planets of all sizes ranging from $1 R_{\oplus}$ to $1 R_{\text{Jup}}$. However, for multiple systems the sizes of planets are closer to the size of Neptune or smaller (e.g. [Latham 2011](#)), suggesting that the presence of a Jupiter-mass planet

either prevents the formation of multiplanetary systems or disrupts their orbits after they have formed.

Now, observations with the *Kepler* space telescope are continued under the *K2* mission (Howell et al. 2014) that is monitoring fields distributed around the ecliptic plane, and is expected to continue operating until 2017 or 2018.

1.3 Planets in giant stars

1.3.1 Properties of planets around giant stars

During the last 20 years, thousands of exoplanets have been discovered showing a variety of orbital configurations that do not resemble the configuration of our Solar System. These discoveries have dramatically revolutionized our view of how planets form, migrate and evolve. The vast majority of extrasolar planet searches have aimed at finding planets around solar-like main-sequence (MS) stars. However, a growing number of groups have also looked for planets around stars more massive and evolved than the Sun (Sato et al. 2003; Hatzes et al. 2005; Johnson et al. 2007; Lovis & Mayor 2007; Lee et al. 2011; Jones et al. 2011; Reffert et al. 2015; Wittenmyer et al. 2016). There are currently 95 planets orbiting giant stars in 86 systems¹¹. Although the number is still small compared to planets orbiting MS stars, their number has dramatically increased in recent years and is expected to do so in the near future with the work of ongoing surveys (e.g. Jones et al. 2016; Niedzielski et al. 2016a). Thanks to these efforts it has been possible to start characterizing this population of planets, which show some important observational properties:

- With masses between $\sim 3\text{-}10 M_{\text{Jup}}$, planets orbiting giant stars tend to be more massive than planets around MS stars.
- On average, planets around giant stars have lower eccentricities.
- Most of the planets in giant stars have periods of more than ~ 100 days.
- There is an apparent lack of close-in planets with semi-major axes of less than ~ 0.5 au.

These findings seem to suggest that there are fundamental differences between the population of planets orbiting evolved stars and the ones around MS stars. Therefore, the detection and

¹¹See the compilation of substellar companions around giant stars maintained by Sabine Reffert at <http://www.lsw.uni-heidelberg.de/users/sreffert/giantplanets.html>

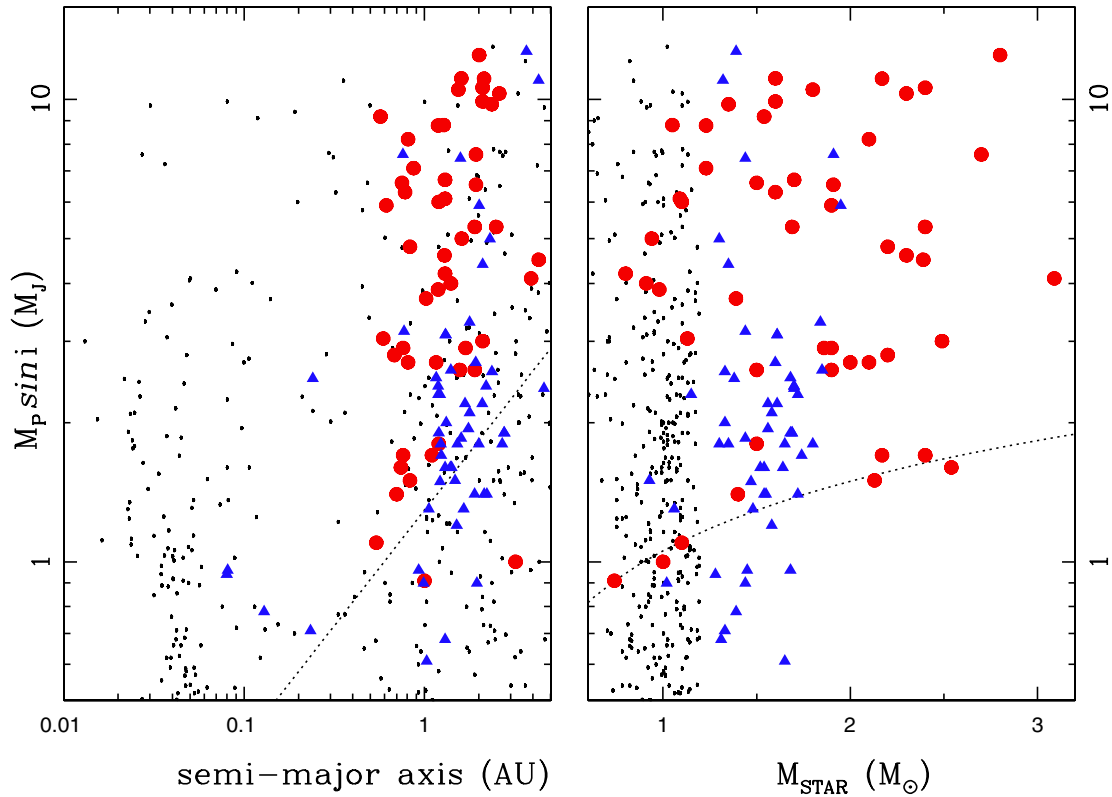


Figure 1.9: Planet mass (minimum) as a function of the semi-major axis (left panel) and the stellar mass (right panel) for planets around solar-type stars (black dots), subgiants (blue triangles) and giant stars (red circles). The dashed lines correspond to a RV amplitude of 30 m s^{-1} , for a planet orbiting a star with a mass of $1.5 M_{\odot}$ (left panel) at an orbital distance of 1 au (right panel). Figure taken from Jones et al. (2014).

characterization of more planets around evolved stars is of critical importance to further study, for instance, the influence of the host-star mass and its disk on the forming planets and their properties, or the planet evolution and planet-star interaction during critical phases of the stellar evolution.

However, for some of the properties mentioned above, it is not clear if they are intrinsic to the population of planets around evolved stars, or if they are the result of observational biases. For instance, the super-masses of planets around evolved stars was first noticed by Lovis & Mayor (2007) that reported an unusual high mass distribution of massive planets and brown dwarfs around post-MS stars. This result has been subsequently confirmed by other authors (e.g. Pasquini et al. 2007; Döllinger et al. 2009; Niedzielski et al. 2015; Reffert et al. 2015). This is

completely different than for the planet population around MS stars, in which the vast majority of planets have masses of less than $\sim 3 M_{\text{Jup}}$. The high masses of planets in giant hosts can be interpreted thinking that more massive stars are expected to have more massive and denser disks from which giant massive planets can form more efficiently. However, there seems to be no correlation between the mass of planets and the mass of their giant hosts (see Fig. 1.9). Additionally, [Jones et al. \(2014\)](#) found that the distribution of planet masses around giant and subgiants are intrinsically different, although [Jofré et al. \(2015\)](#) did not seem to confirm this result. In any case, this suggests that the planet mass is increased during the giant phase of the stellar evolution via, for example, accretion of stellar wind from the envelope of the giant host ([Livio & Soker 1983, 1984](#)) and/or direct mass transfer by Roche lobe overflow ([Jones et al. 2014](#)).

A satisfactory explanation for the high masses of planets in giant stars is further complicated by the recent controversy about the masses of evolved stars. In short, there is a discrepancy between the masses of evolved stars determined from evolutionary tracks and the ones derived from model mass distributions based on galactic population synthesis ([Lloyd 2011, 2013](#)) as well as from galactic stellar motions ([Schlaufman et al. 2013](#)), with the masses derived from evolutionary tracks being systematically higher. Additionally, [Niedzielski et al. \(2016a\)](#) have shown that the masses of giant stars calculated by some surveys may be overestimated by as much as $\sim 43\%$, but they also show that this is not sufficient to explain the large giant planet masses because of the mild dependency of planet mass on stellar mass ($\sim M_{\star}^{2/3}$).

A different interpretation for the large masses of planets around giant stars can be thought in terms of an observational bias for detecting low-mass companions by the RV method around evolved stars. It is well known that giant stars present intrinsic jitter, that mainly results from time-unresolved p-mode oscillations ([Bedding et al. 2010; Kallinger et al. 2012; Stello et al. 2013](#)). These oscillations manifest like noise in the RV curve, therefore, unlike MS stars in which the detectability of planets is mainly limited by RV precision, the detection of low-mass companions around evolved stars is fundamentally limited by the stellar jitter. In addition, low-mass planets have more chances of surviving the processes of evolving off the MS as there is a strong dependence of the tidal forces on the mass ratio of the planet-star system (e.g. [Villaver & Livio 2009; Mustill & Villaver 2012; Villaver et al. 2014](#)). However, it has been probed by several authors that dedicated RV monitoring of evolved stars can lead to the detection of planets with masses of $\lesssim 1 M_{\text{Jup}}$ (e.g. [Gettel et al. 2012; Huber et al. 2013b; Barclay et al. 2015](#)). The question is still open, and certainly more statistics of planets around giants will help to give a definitive answer to this regard.

1.3.2 Occurrence rate of planets in giant stars

There is a well known correlation between giant planet occurrence and stellar metallicity for MS planet host (Gonzalez 1997; Santos et al. 2004; Fischer & Valenti 2005; Udry & Santos 2007). Whether the same holds true for giant stars hosting planets has been a matter of debate during recent years. For example, studies based on a limited number of planets hosted by giants first reported an absence of correlation between the frequencies of planets with metallicity in giant hosts (Sadakane et al. 2005; Schuler et al. 2005; Pasquini et al. 2007; Takeda et al. 2008). Later, this result was confirmed by studies with a larger sample of giant hosting planets (Mortier et al. 2013; Jofré et al. 2015). Probable reasons to explain these results are diverse; problems in determining spectroscopic parameters in evolved stars (Hekker & Meléndez 2007; Santos et al. 2009), enhanced stellar mass compensating the lack of metals (Ghezzi et al. 2010), selection bias in giant star surveys tending to avoid high metallicity red giants (Mortier et al. 2013).

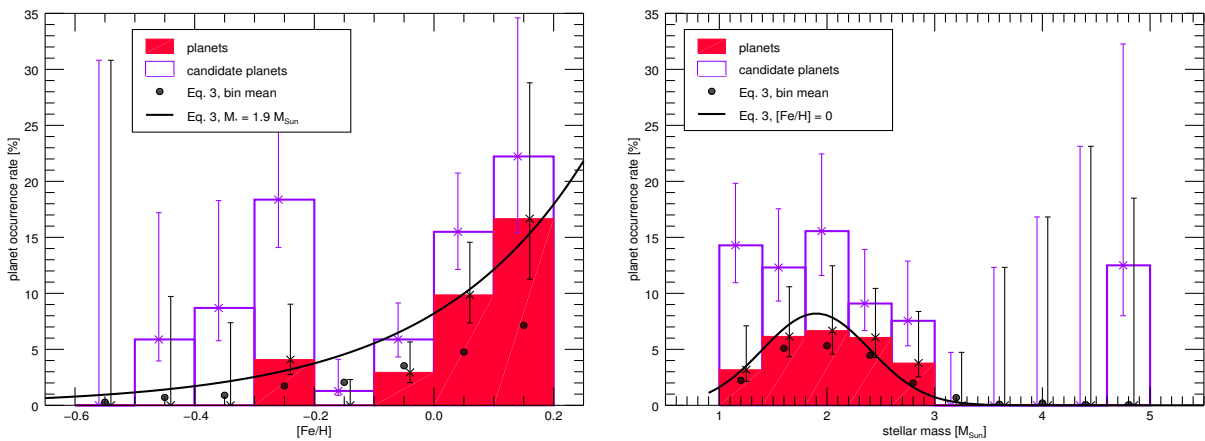


Figure 1.10: The left panel shows the planet occurrence as a function of stellar metallicity for the sample of 373 G and K giant stars from the Lick survey (not taking into account the stellar mass effect). The red histogram shows secure planets, while the open purple one shows planet candidates. The solid line is an exponential fit to the occurrence rate in the secure planet sample for a stellar mass of $1.9 M_{\odot}$. The black dots are also an exponential fit, but taking into account the individual mass distribution in each bin. The right panel is the planet occurrence as a function of mass, ignoring the effects of metallicity. The solid line represents the best Gaussian fit for zero metallicity and the black dots take into account the metallicity distribution in each bin. Figure taken from Reffert et al. (2015).

In contrast with the above findings, but also with a limited sample of stars, Hekker & Meléndez (2007) and Ghezzi et al. (2010) found a metallicity enhancement of about 0.13–0.21 dex in giants with planets, comparable to what is found in MS stars. Similar results of a positive correlation between frequency of giant planets and metallicity was obtained by Quirrenbach et al. (2011)

using preliminary results from the Lick K-giant survey (Frink et al. 2002). Additionally, Johnson et al. (2010) analyzed a sample of subgiant stars and found that their data is consistent with a giant planet-metallicity correlation. Interestingly, Maldonado et al. (2013) found a positive correlation between planet occurrence and metallicity for giant stars with masses larger than $1.5 M_{\odot}$, while for the low-mass stars the correlation is absent.

Recently, based on a much larger and homogeneous sample of planets around giant stars, Reffert et al. (2015) found strong evidence supporting the idea that giant planets are preferentially found around metal-rich hosts (see Fig. 1.10). This result agrees with preliminary findings from the EXPRESS survey (Jones et al. 2011) recently published by Jones et al. (2016). It would appear that the latest evidence based on large and homogeneous surveys points to a confirmation of the giant planet-metallicity relation for giant stars, similar to what is observed for dwarf stars. However, based on an even larger sample of giant stars with planets, although not homogeneous, Maldonado & Villaver (2016) found that the planet-metallicity correlation depends on the stellar evolutionary stage, as it holds for MS and subgiant stars, while they did not find any significant difference in the metallicity of planet and non-planet hosts among the sample of giants. Certainly, improving the sample statistics in the future will help to a better understanding on the formation of giant planets in different type of stars.

1.3.3 Close-in planets around giant stars

As mentioned before, the study of planets around giant stars allows to investigate how the stellar mass influences the formation efficiency of planets, and is thus relevant for planet formation theories. On the other hand, planets close to their host stars can give important information about the processes taking place after the host star leaves the MS. One striking characteristic of planets around evolved stars, pointed out by RV surveys, is that there seems to be a lack of close-in planets orbiting with $a < 0.5$ au (see Fig. 1.9), contrary to what is observed around MS stars. This is intriguing because, in principle, RV surveys have a strong bias towards finding more close-in planets as it has been shown by the large number of short-period planets found around MS stars. This raises the question about where are these close-in planets in evolved stars?

These phenomena have been studied from a theoretical perspective (Villaver & Livio 2009; Kunitomo et al. 2011; Villaver et al. 2014) suggesting that this short-period planets are tidally engulfed by their host stars as the star ascends through the red giant branch (RGB) phase. Villaver & Livio (2009) studied the influence of stellar tides on the orbital evolution of giant planets after the host star leaves the MS showing that a higher engulfment efficiency is expected for more massive planets and less massive stars. Similarly, Villaver et al. (2014) extended the previous work by introducing the effects of the planet eccentricity evolution, and different mass-loss prescrip-

tions in their calculations. They found that tidal engulfment along the RGB is mostly regulated by the planetary mass and showed that rapid tidal orbital decay occurs when $a < 3 R_{\star}$.

A different interpretation is related to intrinsic properties of giant planet formation in stars of distinct masses. It was first shown by [Johnson et al. \(2007\)](#) and later confirmed by [Bowler et al. \(2010\)](#) that close-in planets were absent in intermediate-mass subgiants ($1.3 < M_{\star} < 2.5 M_{\odot}$). This suggests that the scarcity of planets around giant stars may be related to different formation mechanisms dependent on stellar mass, and not to dynamical stellar evolutionary processes. For instance, migration of giant planets through the protoplanetary disk may be halted via short dissipation timescale of the disk ([Burkert & Ida 2007](#); [Currie 2009](#)) or differences in the structure of the protoplanetary disk of intermediate-mass stars with respect to MS stars ([Kretke et al. 2009](#)). However, this interpretation requires that the masses of evolved stars to be higher than MS stars, which has been put into question as described before (see Sec. 1.3.1). In addition, there has been an increase of close-in planets found to orbit MS A-F stars (e.g. [Collier Cameron et al. 2010](#); [Buchhave et al. 2011](#); [Cappetta et al. 2012](#); [Pepper et al. 2013](#); [Bieryla et al. 2014](#)), and this population of planets is not seen in evolved stars, suggesting an effect more related to the stellar evolution than to giant planet formation. However, a recent study by [Borgniet et al. \(2016\)](#) did not find any planet with periods shorter than 100 days from a sample of 108 MS AF-type stars.

1.4 Planets in binary stars

1.4.1 The role of binarity in giant planet formation

Multiple stellar systems are common in our galactic neighborhood. Moreover, the multiplicity rate of solar-like stars is estimated to be $\sim 44\text{--}48\%$ ([Duquennoy & Mayor 1991](#); [Raghavan et al. 2010](#)). It seems logical then to wonder about the possibility of forming planets in systems with more than one stellar component. This is particularly relevant because it is generally accepted that stars establish their binarity before the time in which planets may begin to form. Evidence for this statement comes from the observations of disks around young stars similar to the ones that planets are thought to form (e.g. [Rodriguez et al. 1998](#); [McCabe et al. 2003](#)). Therefore, the search for planets in binary stars gives an opportunity to study and test planet formation theories in multiple stellar environments (e.g. [Boos 2006](#)).

Statistical analyses of planets around single and binary stars have shown that the frequency of planets around single stars is very similar to that of wide separation binaries with $a_B \gtrsim 100$ au ([Raghavan et al. 2006](#); [Bonavita & Desidera 2007](#); [Desidera & Barbieri 2007](#)) implying that the role of these wide stellar companions is not relevant for the process of planet formation. On the

other hand, the population of planets in binary systems with separations of less than 100 au is significantly different than for planets orbiting single stars (Zucker & Mazeh 2002; Bonavita & Desidera 2007). Additionally, there are fewer planets orbiting binaries with $a_B \lesssim 100$ au, and this group of planets tend to be more massive when compared to single isolated stars (Bonavita & Desidera 2007; Duchêne 2010).

The influence of stellar companions in the formation of planets has been debated before, with some studies reaching very different conclusions regarding the relative importance of the core accretion (Mizuno 1980; Lissauer 1993; Pollack et al. 1996) and disk instability (Kuiper 1951; Cameron 1978; Boos 1997) models. Smoothed particle hydrodynamics (SPH) simulations by Nelson (2000) show that giant planet formation by core accretion or disk fragmentation is effectively suppressed for close-separation binaries (~ 60 au or less). Using a different set of SPH simulations Mayer et al. (2005) found that fragmentation is inhibited by the presence of a stellar companion with semi-major axes of less than ~ 60 au, while still allowing the formation of giant planets by core accretion if the disk is light enough, $M_{disk} \sim 0.01 M_{\odot}$. On the other hand, contrary to the previous results, Boos (2006) found that fragmentation is enhanced by binarity¹². It is, therefore, essential to keep increasing the number of observed planets in close-separation binaries that will allow to put strong constraints on giant planet formation in these multiple stellar systems.

1.4.2 Types of planets in binary systems

There are currently 142 exoplanets residing in systems with more than one star.¹³ Several planets have been found in triple star systems (Desidera et al. 2011; Wiegert et al. 2016; Wagner et al. 2016) and even a couple of planets were discovered residing in quadruple stellar systems (Guenther et al. 2009; Schwamb et al. 2013; Riddle et al. 2015). While the majority of planets in multiple stellar systems are found in binary stars (112 planets in 78 systems), most of the exoplanet surveys have been strongly biased against binary stars with separations of $a_B < 200$ au (e.g. Eggenberger & Udry 2010). That is why in most cases, stellar binary companions have been detected after the discovery of the exoplanets in the system, mainly thanks to dedicated imaging campaigns around exoplanet host stars (Raghavan et al. 2006; Eggenberger et al. 2007a; Mugrauer & Neuhäuser 2009; Bergfors et al. 2013; Evans et al. 2016). It is thus expected that the fraction of binary stars with planets will continue to increase in the near future.

¹²For a detailed description and comparison of the studies of Mayer et al. (2005), Nelson (2000) and Boos (2006), I refer the reader to Mayer et al. (2007).

¹³See the catalog maintained by Richard Schwarz at <http://www.univie.ac.at/adg/schwarz/multiple.html>

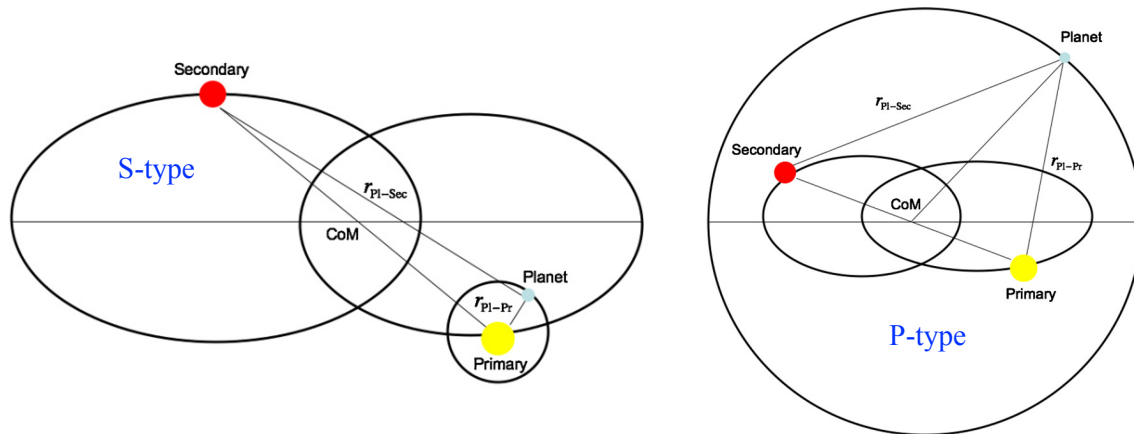


Figure 1.11: Schematic representation of the S- (left panel) and P-type orbits (right panel). In the case of the S-type orbits, the two stars of the binary revolve around their center of mass (CoM) while the planet orbits only one of the stars. For P-type orbits both stars and the planet rotate around the center of mass of the binary (shown by CoM). Figures taken from [Haghighipour & Kaltenegger \(2013\)](#) and [Kaltenegger & Haghighipour \(2013\)](#).

Planets in binary stars are mainly found in two configurations; S-type (circumstellar), where the planet orbits one star of the binary system, and P-type¹⁴ (circumbinary), where the planet orbits around both stellar components (see Fig. 1.11). Although studies concerning the stability of P-type ([Dvorak 1986](#); [Holman & Wiegert 1999](#); [Broucke 2001](#); [Pilat-Lohinger et al. 2003](#)) and S-type ([Rabl & Dvorak 1988](#); [Benest 1988, 1993](#); [Holman & Wiegert 1999](#); [Pilat-Lohinger & Dvorak 2002](#)) planets already existed since long ago, the growing detection of more systems has stimulated the research about the habitability, both in P- and S-type orbits ([Haghighipour & Kaltenegger 2013](#); [Kaltenegger & Haghighipour 2013](#); [Cuntz 2015](#)), and potential formation scenarios of these types of systems. More attention has been given to try to explain the origin of S-type planets ([Haghighipour 2006](#); [Quintana et al. 2007](#); [Haghighipour & Raymond 2007](#); [Guedes et al. 2008](#); [Th ebault et al. 2008, 2009](#); [Eggl et al. 2013a,b](#)), but with the growing number of circumbinary planets discovered by the *Kepler* telescope ([Doyle et al. 2011](#); [Welsh et al. 2012](#); [Orosz et al. 2012a,b](#); [Schwamb et al. 2013](#)), several authors have aimed at explaining also their origin ([Kley & Haghighipour 2014](#); [Meschiari 2014](#); [Bromley & Kenyon 2015](#); [Silsbee & Rafikov 2015](#)).

¹⁴There is another possibility for planets in binary systems; the so called T-type orbits, where the planet orbits in one of the Lagrangian points of the binary orbit. However, no T-type planet has been discovered so far.

1.4.3 Planets in close-separation binaries

As mentioned in Sec. 1.4.1, the study of exoplanets in tight binaries can give important insights to explore not only how these planets form in binary systems, but to understand planet formation in general. This is, however, a very difficult task as the formation of planets consists of a series of complex processes that may be affected in different ways by the presence of a perturbing stellar companion (e.g., [Haghighipour 2011](#)). For instance, the majority of studies have centered around the intermediate phase of km-size planetesimal accretion, because this stage is particularly sensitive to perturbations due to an external body, as it could be a stellar companion. Particularly challenging are the close-separation binary planet hosts with $a_B \lesssim 20$ au. Currently, there are 88 circumstellar planets, of which five reside in close binaries with $a_B \approx 20$ au: Gliese 86 ([Queloz et al. 2000](#)), γ Cep ([Hatzes et al. 2003](#)), HD 41004 ([Zucker et al. 2004](#)), HD 196885 ([Correia et al. 2008](#)), HD 87646 ([Ma et al. 2016](#)), and only two in close-binaries with $a_B \lesssim 15$ au: ν Oct ([Ramm 2016](#)), and HD 59686 ([Ortiz et al. 2016](#), presented in this thesis).

There are several ways in which a close binary companion can complicate the formation of planets. First, the disk can be severely truncated by a close stellar companion. This puts strict constraints on planet formation, determining where planets are allowed to reside and how much material is available for their formation. Second, the presence of a secondary star in an eccentric orbit can make the circumprimary disk to be also eccentric ([Paardekooper et al. 2008](#); [Kley & Nelson 2008](#); [Müller & Kley 2012](#)), and if the binary orbital plane is misaligned with respect to the disk plane, then the protoplanetary disk may become warped, twisted or even disrupted ([Larwood et al. 1996](#); [Fragner & Nelson 2010](#)). Third, disks around close binaries with $a_B < 40$ au present shorter lifetimes on the order of $\sim 0.1 - 1$ Myr (e.g., [Cieza et al. 2009](#)), thus requiring planets to form quickly, probably on timescales of less than ~ 1 Myr.

In the standard core accretion scenario planets are thought to form beyond the ice line of their respective host where there is enough material to accrete. In this context, one of the main problems for planets in tight binaries is the so-called fragmentation barrier. It is thought that planetesimals can grow via collisions and mergers with other objects of similar size ($\lesssim 1$ km) as long as the collisional velocity, v_{col} , is low enough. The presence of a stellar companion can excite the orbital eccentricity of planetesimals, increasing v_{col} to values exceeding the escape velocity or even above the critical level at which the planetesimals are not destroyed by mutual collisions ([Heppenheimer 1978](#); [Whitmire et al. 1998](#); [Thébaud et al. 2008](#)). To overcome this issue larger “initial” planetesimals are needed ($\gtrsim 100$ km) to prevent their destruction by high velocity impacts. This can be achieved by the growth of pebble-sized bodies, through the accretion of dust from the disk ([Xie et al. 2010](#); [Paardekooper & Leinhardt 2010](#); [Windmark et al. 2012](#)). Several models have been developed to advocate for such mechanisms to form km-sized bodies (e.g.,

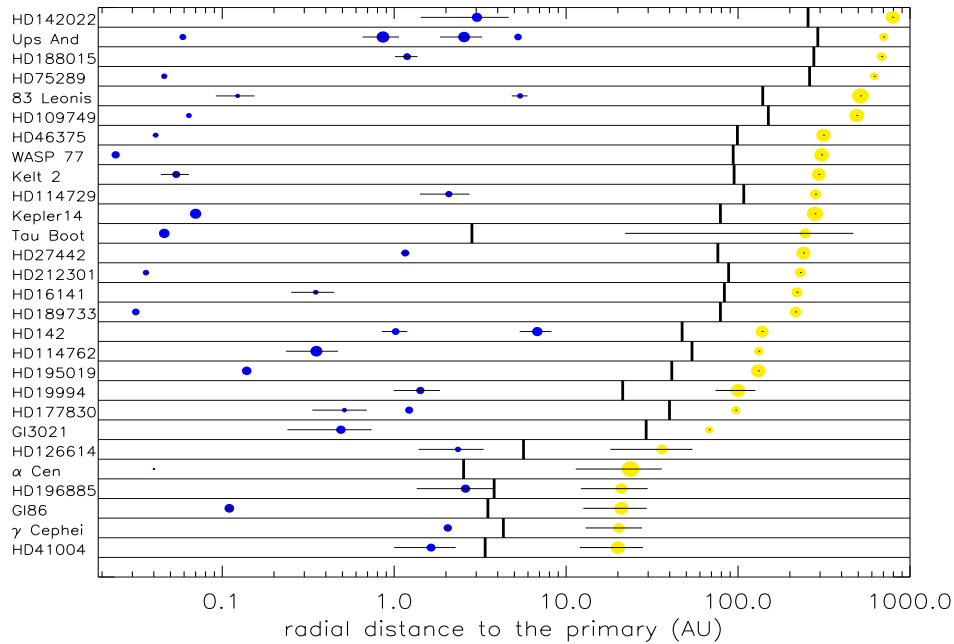


Figure 1.12: Architecture of all S-type planets around binary stars with a separation of $a_B < 1000$ au (as it was until July 2013)¹⁵. Stellar companions are displayed with yellow circles, whose size is proportional to the binary mass ratio M_2/M_1 . Planets are represented by blue circles, whose size is proportional to the planet mass. The horizontal lines in each of the symbols marks the radial excursion of the planets and stars orbit (when they are known). For most binaries of separation ≥ 100 au, the orbit is not known and the displayed value corresponds to the projected current separation. The short vertical lines correspond to the outer limit of the orbital stability region around the primary star, as derived by [Holman & Wiegert \(1999\)](#). Figure taken from [Th ebault & Haghhighipour \(2015\)](#).

[Johansen et al. 2007](#); [Cuzzi et al. 2008](#)), but it still remains to be seen if these methods can be successfully applied to the highly-perturbed environment of a binary system.

A different type of solution for the existence of S-type planets in close binaries is not related to primordial formation of planets, but to the encounter with other stars and/or planets. If most of the stars are born in clusters, then they are expected to experience many close encounters during their early history. This could lead to their planets being lost and/or exchanged ([Pfahl 2005](#); [Mart ı & Beaug e 2012](#)). Moreover, the orbital separation of the stellar pair could have been wider than what it is observed today, therefore avoiding the hostile environment for planet formation in tight binaries ([Malmberg et al. 2007](#); [Marzari & Barbieri 2007](#); [Spurzem et al. 2009](#)). In addition, free

¹⁵The planet in the α Cen system has been recently put into question by [Hatzes \(2013\)](#) and [Rajpaul et al. \(2016\)](#), implying that most likely the planet is not real.

floating planets might have been recaptured by close stellar encounters in binary systems ([Perets & Kouwenhoven 2012](#)). The question of planet formation in close-separation binaries is thus still open, and more theoretical and observational investigations are needed for a better understanding of these systems.

The transiting warm Jupiter Kepler-432 b

This Chapter presents the discovery and characterization of Kepler-432 b: a warm Jupiter planet transiting a red giant star. The Chapter is a version of the article [Ortiz et al. \(2015\)](#).

2.1 Context

The number of Jupiter-like planets found to orbit evolved stars has constantly been growing in recent years. This includes planets around subgiant ([Johnson et al. 2010, 2011](#)) and giant stars ([Gettel et al. 2012](#); [Sato et al. 2013](#); [Trifonov et al. 2014](#)). These discoveries have provided evidence that the gas-giant planet population around evolved stars possesses different orbital properties than the population orbiting main-sequence stars (e.g., [Jones et al. 2014](#)). The most notable trend is the apparent lack of close-in Jupiter-like planets orbiting giant or subgiant stars, although these objects are easily found around many MS stars by Doppler surveys (e.g., [Jones et al. 2013](#)). Specifically, there seems to be a lack of planets around giant stars with semi-major axis $a < 0.5$ au. Some exceptions to this apparent trend are the recently discovered planet HIP67851 b ([Jones et al. 2015a](#)) and Kepler-91 b, the only hot Jupiter known to transit a giant star ([Lillo-Box et al. 2014a](#)).

There are two different mechanisms that have been proposed to explain the paucity of close-in Jupiter-like planets around giant stars. The first one states that, as a result of stellar evolution, the inner planets are tidally engulfed by their host stars as the outer planets move farther out ([Kunitomo et al. 2011](#); [Adamów et al. 2012](#); [Schlaufman et al. 2013](#)). The second one suggests that although giant planets may form around intermediate-mass stars, they do not migrate inwards, owing to the short dissipation time-scale of protoplanetary disks ([Kretke et al. 2009](#);

Currie 2009). By searching specifically for close-in Jupiter-like planets around giant stars, we can help to place constraints on the theoretical models that try to explain these observations and, possibly, also learn something about the evolution of planetary systems after the host star leaves the MS.

In this Chapter, we confirm and characterize Kepler-432 b, a massive warm gas-giant planet orbiting a star ascending the red giant branch.

2.2 High-resolution spectroscopic follow-up

The radial velocity follow-up of Kepler-432 was carried out between June and October 2014 using the Calar Alto Fiber-fed Échelle spectrograph (CAFE; Aceituno et al. 2013) – mounted at the 2.2m telescope of Calar Alto Observatory (Almería, Spain) – and the FIBre-fed Échelle Spectrograph (FIES; Telting et al. 2014) – mounted at the 2.56m Nordic Optical Telescope of Roque de los Muchachos Observatory (La Palma, Spain). We acquired 11 RVs with CAFE ($R \sim 62000$), and 16 with FIES ($R \sim 67000$) at different epochs. To remove cosmic-ray hits, three consecutive exposures were usually taken per epoch observation. Following the observing strategy described in Aceituno et al. (2013) and Buchhave et al. (2010), we traced the RV drift of CAFE and FIES by acquiring long-exposed ($T_{\text{exp}} = 60\text{--}80$ sec) ThAr spectra immediately before and after each epoch observation. The data were reduced using IRAF and IDL standard routines, which include bias subtraction, flat fielding, order tracing and extraction, and wavelength calibration. Radial velocities were derived via multi-order cross-correlation with the RV standard stars HD 182572 (CAFE) and HR 5777 (FIES).

The CAFE and FIES RVs are listed in Table A.1 – along with their uncertainties, total exposure times, signal-to-noise (S/N) ratios per pixel at 5500 \AA , and cross-correlation function (CCF) bisector spans – and are plotted in Fig. 2.1 together with the Keplerian fit to the data (upper panel) and residuals to the fit (middle panel). The lower panel of Fig. 2.1 shows the FIES CCF bisector spans plotted against the RV measurements, assuming that the error bars of the former are twice those of the latter. We followed the method described in Loyd & France (2014) to account for the uncertainties of our measurements and found a $\sim 50\%$ probability that an uncorrelated set of points (null hypothesis) can reproduce the data. The lack of a significant correlation between the CCF bisector spans and the RVs indicates that the Doppler shifts observed in Kepler-432 are most likely induced by the orbital motion of a planet and not by a blended eclipsing binary or stellar activity (see, e.g., Queloz et al. 2001). Moreover, the analysis of the centroid motion during the transit reported in the *Kepler* data validation report excludes, at the $3\text{-}\sigma$ level, any scenario in which the transit signal is caused by a contaminating eclipsing binary at a distance of more than $0.4''$ from the source.

2.3 Results

2.3.1 Stellar properties

We determined the spectral parameters of Kepler-432 by fitting the co-added FIES spectrum (S/N~145 per pixel at 5500 Å) to a grid of synthetic spectra calculated with the SPECTRUM code (Gray & Corbally 1994) using ATLAS9 models (Castelli & Kurucz 2004). Microturbulent (v_{micro}) and macroturbulent (v_{macro}) velocities were derived following Hekker & Meléndez (2007). To derive the stellar mass and radius the most precise methodology involves the use of asteroseismic relations. They relate the large frequency separation $\Delta\nu$ and the frequency at which oscillations have the maximum power ν_{max} with fundamental stellar parameters, like the effective temperature T_{eff} , the stellar radius R_{\star} , stellar mass M_{\star} and density ρ_{\star} . This is based in the assumption that for all evolutionary phases, from the MS to the red-giant phase, it is safe to scale these relations against precisely measured solar values. The most general form of the asteroseismic scaling relations is given by (Chaplin & Miglio 2013):

$$\left(\frac{R}{R_{\odot}}\right) \simeq \left(\frac{\nu_{\text{max}}}{\nu_{\text{max},\odot}}\right) \left(\frac{\Delta\nu}{\Delta\nu_{\odot}}\right)^{-2} \left(\frac{T_{\text{eff}}}{T_{\text{eff},\odot}}\right)^{0.5} \quad (2.1)$$

$$\left(\frac{M}{M_{\odot}}\right) \simeq \left(\frac{\nu_{\text{max}}}{\nu_{\text{max},\odot}}\right)^3 \left(\frac{\Delta\nu}{\Delta\nu_{\odot}}\right)^{-4} \left(\frac{T_{\text{eff}}}{T_{\text{eff},\odot}}\right)^{1.5} \quad (2.2)$$

$$\left(\frac{\rho}{\rho_{\odot}}\right) \simeq \left(\frac{\Delta\nu}{\Delta\nu_{\odot}}\right)^2 \quad (2.3)$$

These relations have been empirically tested for not-evolved stars ($\log g \gtrsim 3.8$) giving errors of $\lesssim 4\%$ in radius and $\lesssim 10\%$ in mass (Huber et al. 2012; Miglio 2012a). However, it has also been shown that there might be significant deviations at other masses and evolutionary stages (White et al. 2011; Miglio et al. 2012b; Mosser et al. 2013). We then decided to use the scaling relations as defined above, but with a correction factor $f(T_{\text{eff}})$, dependent on the effective temperature for values between 4700 and 6700 K, as provided by White et al. (2011):

$$\left(\frac{\rho}{\rho_{\odot}}\right) = \left(\frac{\Delta\nu}{\Delta\nu_{\odot}}\right)^2 \left(\frac{1}{f(T_{\text{eff}})}\right)^2 \quad (2.4)$$

Table 2.1: Stellar parameters of Kepler-432.

Parameter	Value
Effective temperature T_{eff} (K)	5020 ± 60
Spectroscopic surface gravity $\log g$ (\log_{10} dex)	3.35 ± 0.07
Metallicity [M/H] (dex)	-0.02 ± 0.06
Microturbulent velocity v_{micro} (km s^{-1})	1.3 ± 0.3
Macroturbulent velocity v_{macro} (km s^{-1})	3.5 ± 0.5
Projected rotational velocity $v \sin i$ (km s^{-1})	≤ 1
Stellar mass M_{\star} (M_{\odot})	1.35 ± 0.10
Stellar radius R_{\star} (R_{\odot})	4.15 ± 0.12
Age (Gyr)	$3.6^{+1.0}_{-0.6}$
Distance (pc)	874 ± 30
Interstellar extinction A_V (mag)	0.26 ± 0.04
Spectral type	K2 III

where the factor f is given by:

$$f(T_{\text{eff}}) = -4.29 \left(\frac{T_{\text{eff}}}{10^4 \text{ K}} \right)^2 + 4.84 \left(\frac{T_{\text{eff}}}{10^4 \text{ K}} \right) - 0.35 \quad (2.5)$$

We used $\nu_{\text{max},\odot} = 3090 \pm 30 \mu\text{Hz}$ and $\Delta\nu_{\odot} = 135.1 \pm 0.1 \text{ Hz}$ (Huber et al. 2011), and the values of $\nu_{\text{max}} = 108.9 \pm 3.0 \mu\text{Hz}$ and $\Delta\nu = 9.39 \pm 0.22 \text{ Hz}$ provided by Huber et al. (2013a) for Kepler-432, to derive a stellar mass of $M = 1.35 \pm 0.10 M_{\odot}$ and a radius of $R = 4.15 \pm 0.12 R_{\odot}$. We estimated the stellar age using theoretical isochrones from Bressan et al. (2012). Distance and interstellar extinction were calculated following the method described in Gandolfi et al. (2008). The derived stellar parameters are listed in Table 2.1.

2.3.2 Orbit and planet parameters

We fitted a Keplerian orbit to the RV data using the IDL code RVLIN (Wright & Howard 2009). Uncertainties of the derived parameters were estimated using the bootstrap procedure described in Wang et al. (2012). Orbital period P_{orb} and mid-transit epoch T_0 were fixed to the values reported in the Kepler objects of interest (KOI) database.

We fitted for the eccentricity e , argument of periastron ω , radial velocity semi-amplitude K , periastron time T_p , systemic RV γ_{sys} , fixed zero point RV offset between CAFE and FIES datasets, and RV linear trend $\dot{\gamma}$. Fixing $\dot{\gamma} = 0$ leads to a poor fit to the data ($\chi_{\text{red}}^2 = 3.5$), with a systematic offset from the RV measurements. The FIES RV residuals – that is, those with

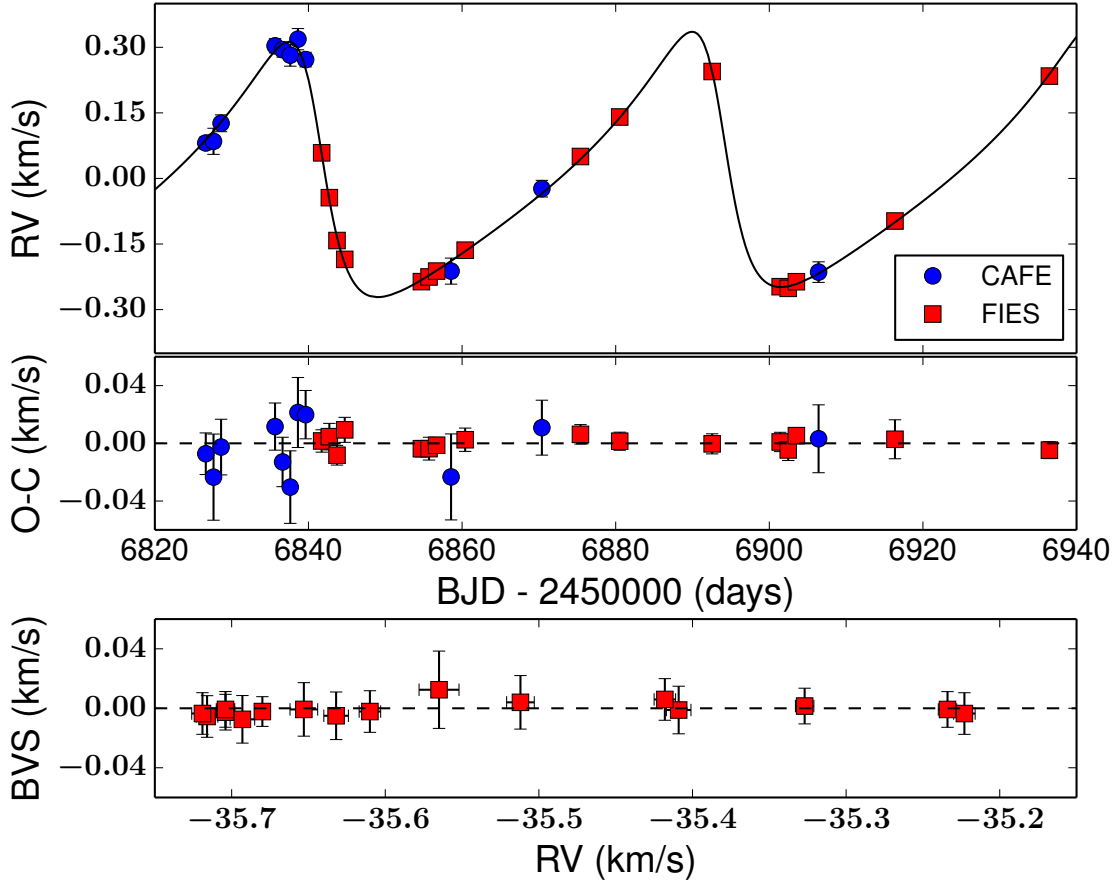


Figure 2.1: Radial velocity measurements of Kepler-432. *Upper panel:* CAFE (blue circles) and FIES (red squares) RVs, and Keplerian fit to the data (black solid line) – including the linear RV trend. *Middle panel:* RV residuals. The rms is ~ 17 m/s and ~ 5 m/s for the CAFE and FIES data, respectively. The observed rms of the FIES RVs is consistent with the expected value of ~ 6 m/s for a star with $\log g = 3.35$ dex (Hekker et al. 2008; Nowak 2013). Quadratically adding a jitter of 6 m/s to our formal RV measurement errors does not change the derived orbital parameters significantly ($< 1\sigma$). Additionally, a fit to the FIES data alone yields consistent results within 1σ . *Lower panel:* Bisector velocity span (BVS) of the FIES CCF versus RVs, assuming that the error bars of the former are twice those of the latter.

Table 2.2: Orbital parameters of Kepler-432 b.

Parameter	Value
RV semi-amplitude K (m s ⁻¹)	294.6 ± 2.1
Eccentricity e	0.478 ± 0.004
Argument of periastron ω (deg)	68.4 ± 0.7
Periastron time T_p (BJD-2 450 000)	6841.06 ± 0.03
Systemic velocity γ_{sys} (km s ⁻¹)	-33 ± 0.3
CAFE-FIES offset velocity (m s ⁻¹)	634 ± 5
RV linear trend $\dot{\gamma}$ (m s ⁻¹ d ⁻¹)	0.44 ± 0.04
Planet mass M_p (M_{Jup})	5.84 ± 0.05
Semi-major axis a (au)	0.303 ± 0.007

Period and mid-transit epoch fixed to $P_{\text{orb}}=52.5010768$ days and $T_0=5004.519$ (BJD-2 450 000). To derive the true planet mass, we use an orbital inclination value of $i=89.95^\circ$ from the KOI database.

the smaller error bars – show a significant correlation with time if no trend is considered, the correlation coefficient being 0.86 with a false-alarm probability lower than 0.9%. Therefore, we consider the trend in the RVs to be real and obtain a value of $\dot{\gamma}=0.44 \pm 0.04$ m s⁻¹ d⁻¹. This is significant at the 11- σ level and most likely due to an additional companion in the system, whose nature remains to be established (see Sec. 2.4.3). We report the best-fit orbital parameters in Table 2.2.

2.4 Discussion

2.4.1 Internal structure and equilibrium temperature

Kepler-432 b is the first *bona fide* confirmed transiting warm Jupiter found to orbit a red giant star. About 70% of the known transiting giant planets have densities in the range 0.35–1.20 g cm⁻³ and masses between 0.3 and 3 M_{Jup} , with a peak around 1 M_{Jup} (Fig. 2.2). With $M_p=5.84 \pm 0.05$ M_{Jup} and $\rho_p=5.4 \pm 0.5$ g cm⁻³, Kepler-432 b is one of the most dense and massive gas-giant planets known so far. The mass of Kepler-432 b agrees with the general trend found by Doppler surveys, that is, planets around giant stars tend to be more massive (3-10 M_{Jup}) than planets orbiting solar-like stars (see e.g., Döllinger et al. 2009; Reffert et al. 2015). In fact, around 96% of the known planets orbiting solar-type MS stars have masses lower than 5 M_{Jup} .

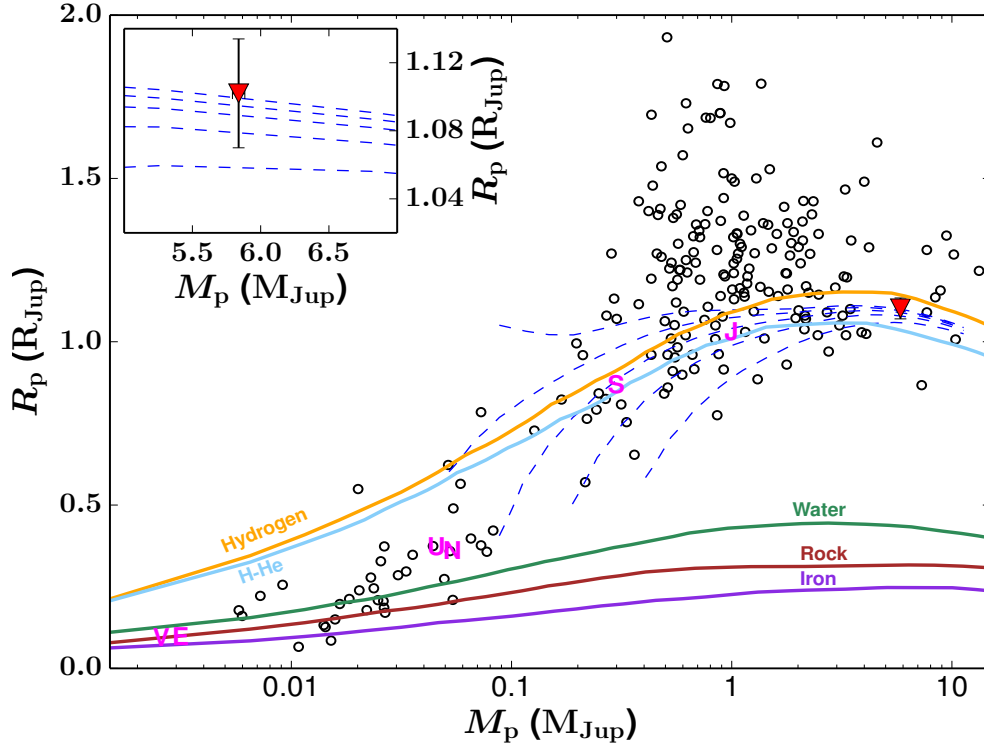


Figure 2.2: Radius and masses of the known transiting exoplanets (black empty circles). The position of Kepler-432 b is marked by the red triangle. The Fortney et al. (2007) isochrones for planet core masses of 0, 10, 25, 50, and 100 M_{\oplus} – interpolated to the insolation and age of Kepler-432 b – are overplotted with dashed lines from top to bottom. The upper left inset is a zoom around Kepler-432 b. Also shown are models for planets of different compositions derived by Seager et al. (2007). Solar system planets are marked with magenta letters. We note that Kepler-432 b falls in a region with a lack of planets between ~ 4.5 and $\sim 7 M_{\text{Jup}}$.

We investigated the internal structure of Kepler-432 b using the models from Fortney et al. (2007), which couple planetary evolution to stellar irradiation for H-He-rich planets (dashed blue lines in Fig. 2.2). The planet radius of $R_p = 1.102 \pm 0.032 R_{\text{Jup}}$ is consistent within $2\text{-}\sigma$ with theoretical values for giant planets with core masses of $\lesssim 100 M_{\oplus}$. This implies that the planet core accounts most likely for 6% or less of the total mass, that is, similar to the fractional core mass of Jupiter (Saumon & Guillot 2004). We note that the solar-like metallicity of the host star $[\text{Fe}/\text{H}] = -0.02 \pm 0.06$ dex supports the low-fractional core mass scenario for Kepler-432 b.

As a consequence of the high eccentricity of the orbit ($e = 0.478 \pm 0.004$), the planet is at nearly ~ 0.16 au ($\sim 8 R_{\star}$) from its host star during periastron, receiving a flux of $F_{\text{per}} = (6.1 \pm 0.6) \times 10^8 \text{ erg s}^{-1} \text{ cm}^{-2}$. At apastron, Kepler-432 b travels as far out as ~ 0.45 au ($\sim 23 R_{\star}$), receiving an incoming radiation of $F_{\text{apo}} = (7.6 \pm 0.8) \times 10^7 \text{ erg s}^{-1} \text{ cm}^{-2}$. The time-averaged incident flux on Kepler-432 b is $\langle F \rangle = (1.66 \pm 0.17) \times 10^8 \text{ erg s}^{-1} \text{ cm}^{-2}$.

Assuming a black-body stellar emission and planetary heat redistribution factor f between 0.25 (instantaneous energy redistribution into the planet atmosphere) and 0.67 (instantaneous energy reradiation to space; see López-Morales & Seager 2007), we derive an average equilibrium temperature of $T_{\text{eq}}=943 \pm 20$ K for a bond albedo of 0.27 (based on Kane & Gelino 2010). Following the planet classification in Sudarsky et al. (2000), Kepler-432 b would be a member of the class IV planets with temperatures in the range $900 < T_{\text{eq}} < 1500$ K, for which a tropospheric silicate layer is expected to exist. However, we note that eccentric orbits can lead to significant changes in the atmospheric compositions, owing to the large variation of the incident stellar flux (Sudarsky et al. 2005). For Kepler-432 b, we expect temperature differences of ~ 500 K between periastron and apastron.

2.4.2 Kepler-432 b: a close-in eccentric planet

Among planets orbiting giant stars, Kepler-432 b is very peculiar both in terms of eccentricity and orbital period, as it occupies scarcely populated regions of the P_{orb} versus M_* and a versus e diagrams (Fig. 2.3). While planets with orbital periods between 1 and 10^4 days are common around MS stars, there is a clear lack of short-period planets around giant stars, and Kepler-432 b is one of the few inhabitants of the region with $P_{\text{orb}} < 100$ days.

The value of $e=0.478 \pm 0.004$ for the eccentricity is among the highest for planets orbiting giant stars. Most planets around giant stars tend to have low eccentricity (63% have $e < 0.2$), with a median of $e = 0.15$, whereas planets around MS stars tend to be more eccentric. If we consider objects with $a \gtrsim 0.5$ au – where most of the planets around giant stars are found – only 39% of planets orbiting solar-type stars exhibit $e < 0.2$, and a K-S test gives a probability of 0.1% that the eccentricity of planets around giant and MS stars is drawn from the same distribution.

Because Kepler-432 b is dynamically young (circularization time scale $\tau_{\text{circ}} \sim 150$ Gyr; see Jackson et al. 2008), the non-zero eccentricity of the planet might be a tracer of its migration history. In this context, it is expected that some kind of high-eccentricity migration (HEM) mechanism might have operated to excite the eccentricity of Kepler-432 b to its current value (see Socrates et al. 2012 and references therein). Within this scenario, it has been proposed that warm Jupiters can form via tidal dissipation at the high- e stage during Kozai-Lidov oscillations (Wu & Lithwick 2011; Dong et al. 2014). Moreover, Dong et al. (2014) suggested that these planets need close companions for HEM to occur. They calculated upper limits for the perturber separation b_{per} to allow an efficient tidal dissipation of the orbit. Assuming a perturber mass between 1 and $10 M_{\text{Jup}}$, we find an upper limit of $b_{\text{per}} = 6 - 13$ au for an additional object in the Kepler-432 system.

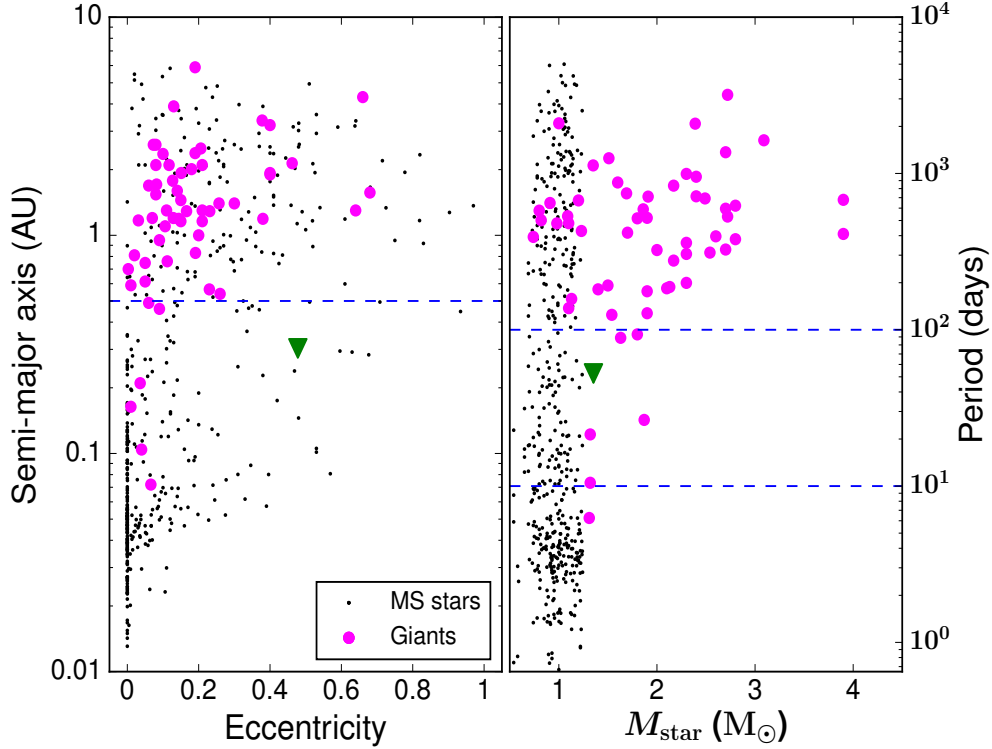


Figure 2.3: *Left panel:* Eccentricity and semi-major axis of the extrasolar planets discovered around MS stars (black dots) and giant stars (magenta circles). The dashed line shows the value of $a = 0.5$ au. *Right panel:* Orbital period versus stellar mass. The dashed lines represent the region of $10 \leq P_{\text{orb}} \leq 100$ days. The position of Kepler-432 b is marked with a green triangle in both panels.

Following [Montet et al. \(2014\)](#), for example, the detected RV acceleration $\dot{\gamma} = 0.44 \text{ m s}^{-1} \text{ d}^{-1}$ requires a perturbing object in a circular orbit at $a \sim 1$ and $a \sim 3$ au for masses of 1 and $10 M_{\text{Jup}}$, respectively, consistent with the HEM scenario. We consider it unlikely that spot-induced variability might be the source of the RV drift because no emission in the core of the Ca H and K lines is detected in the FIES co-added spectrum. Furthermore, [McQuillan et al. \(2013\)](#) found no significant modulation in the *Kepler* light curve of Kepler-432, which suggests that this is a magnetically quiet star. A second companion in the system is thus the best explanation for the observed RV drift.

2.4.3 Comparison with other works

In a contemporaneous study, [Ciceri et al. \(2015\)](#) also confirmed the planetary nature of Kepler-432 b. They obtained a large set of RV measurements, also with CAFE, but covering a much larger time-span (~ 425 days). However, their RV uncertainties are much larger than ours (\sim

60 m s^{-1}), and that is why they could not detect the signature of the RV linear trend that we see in our data. Additionally, they concluded that the planet might survive the RGB evolution of its host star, but this was based on the assumption that the tidal interaction during the giant evolution can be neglected. We arrived at a different conclusion as it will be discussed in the following section.

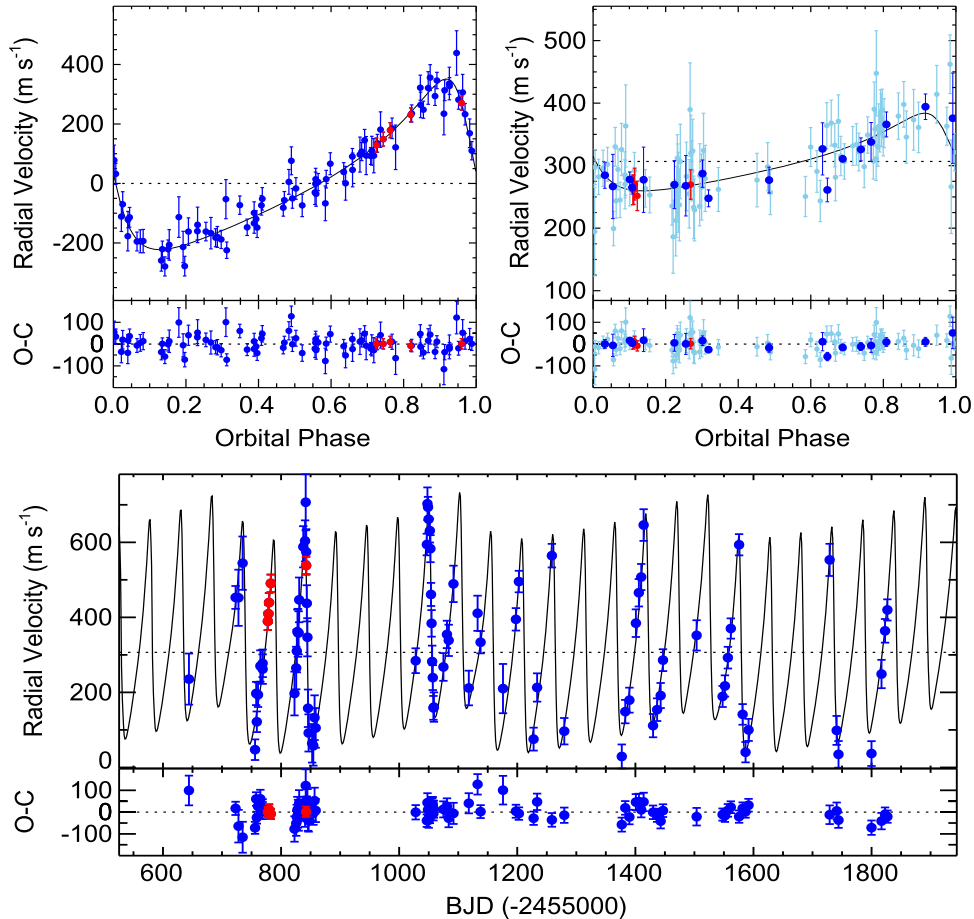


Figure 2.4: The upper plots show the RV signal caused by Kepler-432 b (left) and Kepler-432 c (right), while the bottom plot is the combined RV time series. Red colors represent data obtained with FIES and blue colors with TRES. For Kepler-432 c, the light blue color is the individual RVs and the dark blue is the binned data. Figure taken from [Quinn et al. \(2015\)](#).

A posterior publication of [Quinn et al. \(2015\)](#) also studied the Kepler-432 system. They observed the giant star with the Tillinghast Reflector Echelle Spectrograph (TRES; [Furész 2008](#)) and obtained 84 RV observations during a time-span of ~ 3 years (see Fig. 2.4). Because of this large monitoring they were able to detect the signal of an additional companion, Kepler-432 c, having a minimum mass $\sim 2.6 M_{\text{Jup}}$ orbiting at a minimum distance of ~ 1.2 au. This result is in agreement with the RV linear trend that we detected in our data and confirm the presence of second

planet in the system. [Quinn et al. \(2015\)](#) also performed a complete asteroseismic analysis of Kepler-432 that allowed them to constrain with a high probability the inclination of the stellar spin – with respect to the line-of-sight – to a value of 90_{-8}^{+0} deg. This means that most likely there is no misalignment between the star spin and the orbital axis of Kepler-432 b. If the planet migrated inward through the HEM mechanism (as discussed in Sec. 2.4.2), then we might expect that both the eccentricity and the mutual inclination to grow. They suggested that the planet has re-aligned its orbit (after it gravitationally migrated inward) due to tidal or magnetic interaction with the giant host. As discussed before, we did not find any strong indication pointing to a magnetically active star, but this possibility cannot be fully excluded.

Another mechanism to explain the apparent spin-orbit alignment is the migration of the transiting planet via coplanar high-eccentricity migration (CHEM), as recently proposed by [Petrovich \(2015\)](#) to explain the origin of aligned hot Jupiters. However, this requires that the outer planet, Kepler-432 c, is also aligned with the inner planet, which is not known at the moment. Additionally, CHEM predicts the formation of many hot Jupiters, but almost no warm Jupiter, like Kepler-432 b ([Petrovich 2015](#)). We also note that a recent publication of [Antonini et al. \(2016\)](#) studied the dynamical constraints on the formation of hot and warm Jupiters with close companions. They concluded that most of the Jupiter planets with companions, including Kepler-432 b, would be dynamical unstable if the inner planet is thought to have formed at distances of $\gtrsim 1$ au from its host star; evidence that goes against the formation of Kepler-432 b via high-eccentricity migration.

2.4.4 Post-main-sequence evolution

Kepler-432 b is a massive planet ($M_p = 5.84 \pm 0.05 M_{\text{Jup}}$) and is one of the few members found to orbit a giant star at a distance closer than $a = 0.5$ au (Fig. 2.3). Although the current sample is not statistically significant, the discovery of Kepler-432 b confirms that close-in planets around intermediate-mass giant stars do exist. Given the short dissipation time-scale of protoplanetary disks, gravitational interaction seems to be the favorite migration channel for close-in planets of intermediate-mass stars. It is, however, unclear at the moment if their paucity might be ascribed by an enhanced tidal dissipation and subsequent engulfment during an early stage of the RGB, or maybe a product of an observational bias.

Several studies have computed the planetary orbit evolution during the post MS phase for stars more massive than the Sun ([Villaver & Livio 2009](#); [Kunitomo et al. 2011](#); [Villaver et al. 2014](#)). For instance, [Villaver & Livio \(2009\)](#) has taken into account several mechanisms that may influence the orbital separation between the planet and the host star as the star evolves off the MS, like the mass changes of both star and planet, the gravitational and frictional drag, and the tidal

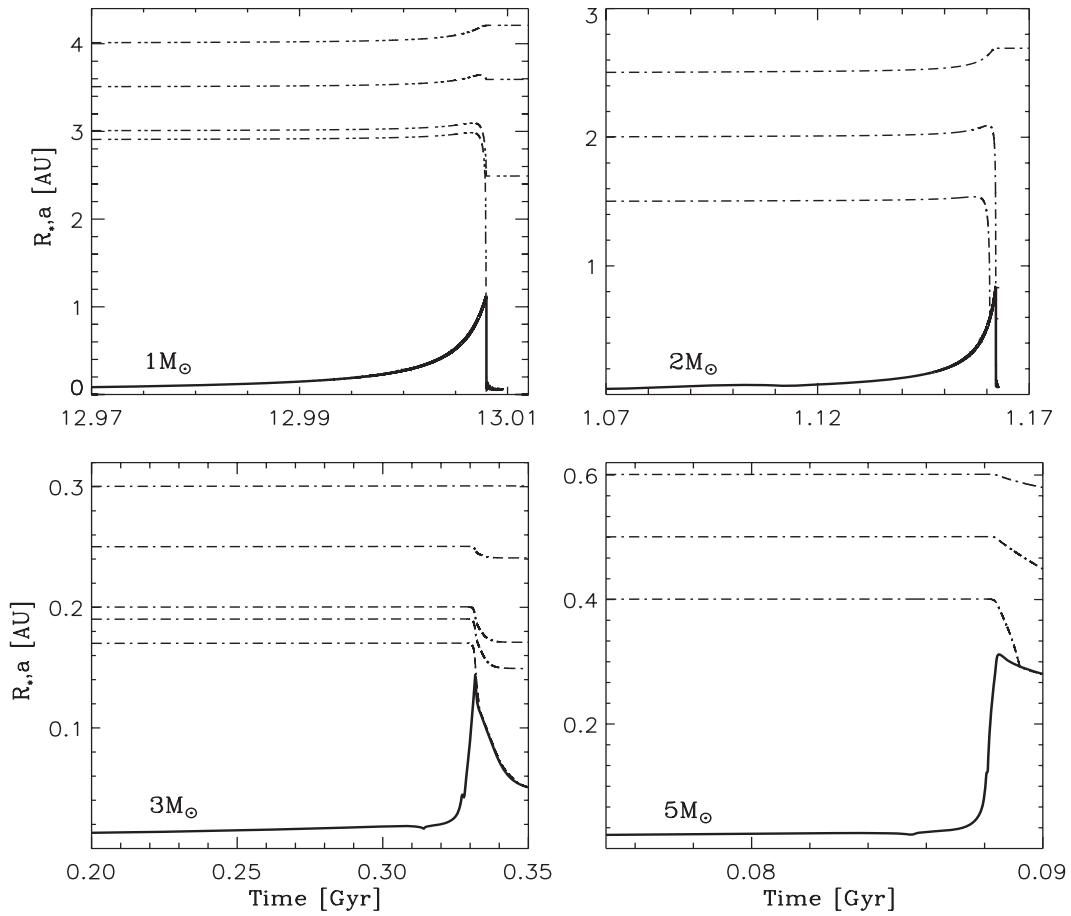


Figure 2.5: Evolution of the stellar radius (solid line) during the RGB and the semi-major axis (dash-dotted line) of a $1 M_{\text{Jup}}$ planet. Different MS stellar masses are also shown, and the set of dashed lines are the orbits for different initial values for the semi-major axis. Figure taken from [Villaver & Livio \(2009\)](#).

interaction. They concluded that short-period planets are swallowed by their host stars as a result of the increased star-planet tidal interaction during the RGB phase. Additionally, they found that the tidal capture radius increases for more massive planets and decreases with increasing stellar mass. They also predict a critical semi-major axis below which planets are engulfed by their host star. The expected values for a star as massive as Kepler-432 are much higher than the current semi-major axis ($a = 0.303 \pm 0.007$ au) of Kepler-432 b (see Fig. 2.5). The same holds true for the values predicted by [Kunitomo et al. \(2011\)](#) and [Villaver et al. \(2014\)](#). This implies that Kepler-432 b will not survive the RGB stellar phase and will be swallowed by its host star before it reaches the tip of the RGB.

2.5 Summary

We spectroscopically confirmed the planetary nature of the transiting candidate Kepler-432 b, derived a planetary mass of $M_p = 5.84 \pm 0.05 M_{\text{Jup}}$, and found that the orbit is eccentric ($e = 0.478 \pm 0.004$). Kepler-432 b is one of the few warm Jupiter planets found to orbit and also transit a giant star. The semi-major axis $a = 0.303 \pm 0.007$ au and eccentricity of the planet suggest that some kind of migration mechanism must have operated (or is operating now) to bring the planet to its current position. In this context, we discussed the high-eccentricity migration scenario as a plausible mechanism for the formation of this system. This possibility, although not directly verifiable with the currently available data, would account for the high eccentricity and small semi-major axis of the planet, although a recent study put into question the effectiveness of HEM to form warm Jupiters with close companions ([Antonini et al. 2016](#)). More investigation is needed to reach a definitive conclusion about the origin of Kepler-432 b.

We also detected a significant radial velocity trend in our data pointing towards the presence of an additional outer body in the system. This was subsequently confirmed by [Quinn et al. \(2015\)](#) that detected the signal of a third Jupiter-mass planet orbiting at a minimum distance of 1.2 au from the host giant star. Although our discovery confirms that close-in ($a \lesssim 0.5$ au) giant planets can exist around giant stars, more detections are needed to properly characterize the population of these objects around post-MS stars. According to current post-MS evolutionary models, Kepler-432 b will not survive the RGB phase and will be engulfed by its host star. The enhanced tidal interaction during this stage is most likely the responsible for the absence of planets around evolved clump giants.

The transiting hot Jupiter Kepler-91 b

This Chapter presents the detailed characterization and independent confirmation of the hot Jupiter planet Kepler-91 b.¹

3.1 Context

The population of planets around giant stars has grown significantly in the past years thanks to dedicated radial velocity surveys that aimed at observing giant and subgiant stars evolving off the main-sequence (e.g., [Döllinger et al. 2009](#); [Sato et al. 2013](#); [Reffert et al. 2015](#)). Among other things, they have demonstrated an apparent lack of close-in planets ($a < 0.5$ au) around giant stars (see, e.g., [Sato et al. 2008](#); [Jones et al. 2014](#)). This observational property has been now challenged with the recent discovery of several close-in planets orbiting around evolved stars with $a < 0.5$ au (e.g., [Ortiz et al. 2015](#); [Ciceri et al. 2015](#); [Grunblatt et al. 2016](#); [Niedzielski et al. 2016b](#)).

The unveiling of this warm planet population around giant stars has been mainly possible thanks to the discoveries of transiting planets around subgiants and red-giant-branch stars observed by *Kepler* ([Borucki et al. 2010](#)) and, more recently, by the *K2* mission ([Howell et al. 2014](#)). The detailed characterization of these systems is possible through asteroseismology that allows the determination of very precise stellar parameters (e.g., [Lillo-Box et al. 2014a](#); [Quinn et al. 2015](#)). Additionally, close-in planets around evolved stars can be used to test different inflation mechanisms proposed to explain the anomalously large radii of transiting planets ([Lopez & Fortney](#)

¹The Chapter is a version of an article currently under revision from co-authors that will be submitted soon to *Astronomy & Astrophysics*.

2016; Grunblatt et al. 2016) as well as the study of the enhanced tidal interaction during the RGB phase between the planet and the host giant (Van Eylen et al. 2016).

Within this group of close-in planets is Kepler-91 b, which is of particular importance since it is one of the two hot Jupiters ($a < 0.1$ au) found to transit a giant star². The planet was first announced by Lillo-Box et al. (2014a) that used the out-of-transit light modulations of *Kepler* photometry to assess the planetary nature of the object. On the other hand, using a similar approach, a previous study of Esteves et al. (2013) had flagged the object as a false positive. Additionally, Sliski & Kipping (2014) has also questioned the planetary nature of the body, as they claimed the asteroseismic stellar density differs significantly from the value derived from the transit light curve alone. However, recent RV observations have demonstrated that Kepler-91 b is indeed a hot Jupiter planet transiting a giant star (Lillo-Box et al. 2014a; Barclay et al. 2015; Sato et al. 2015).

Unfortunately, despite the extensive orbital coverage in Lillo-Box et al. (2014a), the uncertainty of their RV measurements are large, being of the order of ~ 90 m s⁻¹, while the RV semi-amplitude of the planet is ~ 80 m s⁻¹. In the case of the study of Barclay et al. (2015), they achieved smaller RV uncertainties (~ 20 m s⁻¹), but the orbital sampling is rather poor. The same applies to the RV observations made by Sato et al. (2015) that, despite having small errors, mostly covers half of the orbital phase. As Kepler-91 b provides a unique opportunity for studying the evolution of planetary systems after the host star leaves the main-sequence, it is of critical importance to constrain its orbital and physical properties as best as possible.

In this Chapter, we provide an improved orbital solution for the Kepler-91 system by using our own high-resolution spectra together with the publicly available RV data of the star. We model together the RV data and the transit photometry, including the effects of the out-of-transit modulations, to constrain the orbital and physical parameters of the planet with high accuracy. The chapter is organized as follows: In Section 3.2 we describe our radial velocity follow-up of Kepler-91 and our FIES and CAFE observations. Section 3.3 presents the spectral analysis of the giant star and the derived spectroscopic parameters. In Section 3.4 we describe the RV and transit modelling of the data, including the out-of-transit modulation of the light curve. In Section 3.6 we analyze the physical properties of the hot Jupiter planet Kepler-91 b, and discuss about the population of close-in planets around evolved stars. Finally, in Section 3.7, we present our conclusions.

²The other is the recently discovered planet EPIC 211351816.01 (Grunblatt et al. 2016)

3.2 High-resolution spectroscopic follow-up

We observed Kepler-91 with CAFE (Aceituno et al. 2013) spectrograph and FIES (Frandsen & Lindberg 1999; Telting et al. 2014), following a similar strategy than for the observations of Kepler-432. Between June and October 2014, we acquired 9 spectra with CAFE ($R \sim 62000$) and also 9 with FIES ($R \sim 67000$). Three or two consecutive exposures of 1200–1800 seconds were taken per epoch observation to remove cosmic ray hits. We traced the RV drift of the instruments by acquiring long-exposed ($T_{\text{exp}} = 60\text{--}80$ sec) ThAr spectra right before and after each epoch observation. The spectra were reduced using IRAF and IDL standard routines, which include bias subtraction, flat fielding, order tracing and extraction, and wavelength calibration. The radial velocities were derived via multi-order cross-correlation with the RV standard star HD 3765, for which we adopted an heliocentric radial velocity of -63.3 km s^{-1} , as measured by Udry et al. (1999).

3.3 Spectroscopic parameters

We co-added separately the FIES and CAFE data to get two combined spectra of higher S/N ratio and performed the spectral analysis using two different codes.

The first analysis is based on an IDL software suite that uses synthetic model spectra to iteratively fit features that are sensitive to different photospheric parameters. We calculated the synthetic spectra with the code SPECTRUM (Gray & Corbally 1994) using ATLAS9 models (Castelli & Kurucz 2004). Microturbulent (v_{micro}) and macroturbulent (v_{macro}) velocities were derived following Hekker & Meléndez (2007). We primarily used the wings of the Balmer lines ($H\alpha$ and $H\beta$) to estimate the effective temperature (T_{eff}) and measured the surface gravity ($\log g$) from the Mg I 5167, 5173, and 5184 Å, Ca I 6122, 6162, and 6439 Å, and the Na I D lines. We simultaneously fitted different spectral regions to measure the metal abundance [M/H]. The projected rotational velocity $v \sin i$ was determined by fitting the profile of about 100 isolated metal lines.

The second analysis uses the spectral analysis package SME (Valenti & Piskunov 1996; Valenti & Fischer 2005; Piskunov & Valenti 2016). For a set of given stellar parameters, SME calculates synthetic spectra of stars and fits them to observed high-resolution spectra using a χ^2 minimizing procedure. In order to calculate the synthetic spectra, SME makes use of grids of pre-calculated models. The grid of models we adopted for Kepler-91 was produced in Vienna using the ATLAS9 code (Heiter et al. 2002). Some of the models were later recomputed specifically for SME. The grid contains 5 456 models and covers the range of effective temperature (T_{eff}) from 4000–10 000 K in steps of 200 K. The range for the surface gravity ($\log g$) is 2–5 (cgs) with a step of

Table 3.1: Stellar parameters of Kepler-91.

Parameter	Value
Effective temperature T_{eff} (K)	4480 ± 90
Spectroscopic surface gravity $\log g$ (\log_{10} dex)	2.87 ± 0.17
Metallicity [M/H] (dex)	0.10 ± 0.09
Microturbulent velocity v_{micro} (km s^{-1})	2.0 ± 0.5
Macroturbulent velocity v_{macro} (km s^{-1})	3.8 ± 0.5
Projected rotational velocity $v \sin i$ (km s^{-1})	3.0 ± 1.0
Stellar mass M_{\star} (M_{\odot}) ¹	1.31 ± 0.10
Stellar radius R_{\star} (R_{\odot}) ¹	6.30 ± 0.16
Age (Gyr) ¹	4.86 ± 2.13

¹ Data from [Lillo-Box et al. \(2014a\)](#)

0.2 (cgs). The metal content is ± 1.0 , ± 0.5 , ± 0.3 , ± 0.2 , ± 0.1 and 0 dex. The microturbulence velocity, v_{micro} , in the model grid is set to 0.0 km s^{-1} , and the mixing length parameter is 0.9. We fitted the same spectral features used by the first code. We measured the microturbulence and macroturbulent velocities letting SME to solve for them.

The two analyses provided consistent results well within the error bars, regardless of the method and spectrum used. We used the weighted means of the two sets of results. The values adopted for the stellar mass and radius are taken from [Lillo-Box et al. \(2014a\)](#) that modeled the individual frequencies of oscillation in the light curve of Kepler-91, providing the most accurate results. The spectral parameters of Kepler-91 are listed in Table 3.1.

3.4 Transit and radial velocity modeling

3.4.1 Overview

We model the *Kepler*-observed photometry jointly with the radial velocity datasets. The light curve model includes transits, secondary eclipses, phase variations (using a simple Lambertian model), thermal emission (constant), Doppler boosting, and ellipsoidal variations. The RV model includes the RV signal due to Kepler-91 b, instrument-specific zeropoints, and a constant acceleration term accounting for a possible long-period companion in the system.

3.4.2 Data

3.4.2.1 Kepler long cadence photometry

The *Kepler* long-cadence (LC, $T_{\text{exp}} = 1765.46$ sec) photometry for Kepler-91 covers the quarters 1-17 ($Q_1 - Q_{17}$) from 13 May 2009 to 11 May 2013. No short-cadence data is available. The LC data contain 223 transits. We use the PDC-MAP light curves for the analysis.

3.4.2.2 Radial velocity observations

The radial velocity data consist of our FIES and CAFE observations (described in Section 3.2) combined with RVs taken with the High Dispersion Spectrograph (HDS; [Noguchi et al. 2002](#)) presented in [Sato et al. \(2015\)](#) and observations made with the High-Resolution-Spectrograph (HRS; [Tull 1998](#)) presented in [Barclay et al. \(2015\)](#).

3.4.3 Log posterior density

The non-normalized log-posterior probability density is

$$\begin{aligned} \log P(\theta|D) = & \log P(\theta) + \log P(F|\theta) + \\ & \log P(V_{\text{FIES}}|\theta) + \log P(V_{\text{HRS}}|\theta) + \\ & \log P(V_{\text{CAFE}}|\theta) + \log P(V_{\text{HDS}}|\theta) \end{aligned} \quad (3.1)$$

where F is the *Kepler* photometry; V are the radial velocity dataset from FIES, HRS, CAFE, and HDS; θ is the parameter vector; and D stands for the combined dataset. The first term is the log-prior probability density, and the five remaining terms are the likelihoods for the photometry and RV data.

The log-likelihoods are calculated assuming normally distributed white noise. The likelihood for the photometry is

$$\begin{aligned} \log P(F|\theta) = & -\frac{N_D}{2} \log(2\pi) - N_D \log(\sigma_D) \\ & - \sum_{i=1}^{N_D} \left(\frac{D_i - M(t_i, \vec{\theta})}{\sigma_D} \right)^2, \end{aligned} \quad (3.2)$$

where N_D is the number of datapoints, σ_D is an uncertainty (error) term, M is the model, and t_i is the mid-observation time. The photometry data use a single unconstrained average error term

that is estimated jointly with the rest of the model parameters. The likelihood for a single RV dataset is

$$\begin{aligned} \log P(V_I|\theta) = & -\frac{N_D}{2} \log(2\pi) - \sum_{i=1}^{N_D} \log \sqrt{\sigma_i^2 + \sigma_I^2} \\ & - \sum_{i=1}^{N_D} \left(\frac{D_i - M(t_i, \vec{\theta})}{\sqrt{\sigma_i^2 + \sigma_I^2}} \right)^2, \end{aligned} \quad (3.3)$$

where V_I are the radial velocities for instrument I , σ_i is the error estimate for a single datapoint, and σ_I is an additional instrument-specific error term estimated from the data.

3.4.4 Radial velocity model

The radial velocities for instrument I are modelled as

$$V_I = Z_I + K [\cos(\omega + \nu) + e \cos \omega] + \dot{\gamma}t, \quad (3.4)$$

where Z_I is the instrument-specific RV zeropoint, K is the RV semi-amplitude, e is the eccentricity, ω is the argument of periastron, ν is the true anomaly, t is time, and $\dot{\gamma}$ is a constant acceleration term.

3.4.5 Light curve model

The light curve model presents the flux normalized to a baseline level F_{bl} as

$$F = \frac{T(z, k, \vec{u})(F_{ev} + F_{db}) + E(z, k)(F_{pr} + F_{pe})}{F_{bl}}, \quad (3.5)$$

where T is the transit shape model, z is the normalized planet-star centre distance, k is the planet-star radius ratio, \vec{u} is the limb darkening coefficient vector, $E(z, k)$ is the eclipse shape model, F_{pr} and F_{pe} are the scattered and emitted fluxes from the planet, respectively, F_{ev} is the ellipsoidal variation model, F_{db} is the Doppler boosting, and F_{bl} is the flux baseline.

We use the quadratic transit model by [Mandel & Agol \(2002\)](#) as implemented in the *PyTransit* package by [Parviainen \(2015\)](#).³ The transit model is supersampled (six sub-samples per exposure) to avoid the effects due to long exposure time ([Kipping 2010](#)).

³<https://github.com/hpparvi/PyTransit>

3.4.5.1 Reflected and emitted flux

The total flux from the planet is modeled as the sum of the reflected and emitted flux multiplied by the eclipse function. That is,

$$F_p = k^2 E(z, k) \left(\frac{r A_B}{a_s^2} \Phi(\alpha) + \frac{B(T_p, \lambda)}{B(T_\star, \lambda)} \right), \quad (3.6)$$

where $E(z, k)$ is the eclipse shape function, r is the inverse of the phase integral (here we choose $r = 1.5$), A_B the Bond albedo, k the radius ratio, a_s the scaled semi-major axis (semi-major axis divided by the stellar radius), Φ the phase function, α the phase angle, B the spectral radiance given by Planck's law, T_p the planet's brightness temperature, T_\star the effective stellar temperature, and λ the effective wavelength. We use the Lambert's phase function

$$\Phi(\alpha) = \frac{\sin \alpha + (\pi - \alpha) \cos \alpha}{\pi}, \quad (3.7)$$

and we assume a constant brightness temperature. The eclipse shape is modelled using the uniform-disk model with *PyTransit*.

3.4.5.2 Ellipsoidal variations

We model the ellipsoidal variations using the approach adopted by [Lillo-Box et al. \(2014a\)](#), see [Pfahl et al. 2007](#) for more details). The flux variation due to the ellipsoidal variations are

$$F_{ev} = -\frac{\alpha_e M_p}{a_s^3 M_\star} \left(\frac{1 + e \cos \nu}{1 - e^2} \right)^3 \sin^2 i \cos 2\alpha, \quad (3.8)$$

where e is the eccentricity, ν the true anomaly, i the inclination, M_p the planet mass, M_\star the stellar mass, and

$$\alpha_e = 0.15 \frac{(15 + u)(1 + g)}{3 - u}, \quad (3.9)$$

where u and g are the limb darkening and gravity darkening coefficients, respectively.

3.4.5.3 Doppler boosting

We model the Doppler boosting following the approach by [Lillo-Box et al. \(2014a\)](#), that is

$$F_{db} = A_b (\sin(\nu + \omega + \pi/2) + e \cos \omega), \quad (3.10)$$

where the Doppler boosting amplitude A_b is approximated as

$$A_b = \frac{(3 - G)K}{c}, \text{ where } G = \frac{e^x(3 - x) - 3}{e^x - 1}, \quad x = \frac{hc}{k_B \lambda T_\star}, \quad (3.11)$$

K is the RV semi-amplitude, h is the Planck constant, c is the speed of light in vacuum, k_B is the Boltzmann constant, λ is the effective wavelength (fixed to 575 nm, as in Lillo-Box et al. 2014a), and T_\star is the effective stellar temperature.

3.4.6 Parameterization and priors

We parametrize the model using 24 parameters listed in Table 3.2. We use the limb darkening parametrization introduced by Kipping (2013), where the mapping from the sampling parameters a_1 and b_2 to quadratic limb darkening coefficients u and v is done as

$$u = \sqrt{a_1}2b_2, \quad v = \sqrt{a_1}(1 - 2b_2). \quad (3.12)$$

This sampling parametrization allows us to marginalize over the physically acceptable quadratic limb darkening coefficient space.

3.4.7 Numerical methods

The transits were modelled using *PyTransit* (Parviainen 2015). The sampling was carried out using *emcee* (Foreman-Mackey et al. 2013) a Python implementation of the affine invariant MCMC sampler by Goodman et al. (2010). The sampler was initialized using a population of parameter vectors clumped around the local posterior maximum using *PyDE*,⁴ a Python implementation of the Differential Evolution global optimization algorithm (Storn & Price 1997). The analysis uses the set of packages build around SciPy and NumPy (van der Walt et al. 2011): IPython (Perez & Granger 2007), Pandas (McKinney 2010), matplotlib (Hunter 2007), seaborn,⁵ PyFITS,⁶ and F2PY (Peterson 2009).

3.4.8 Derived parameters

3.4.8.1 Bond albedo

The Bond albedo, A_B , is derived from the phase curve amplitude F_{pr} as

$$A_B = \frac{F_{\text{pr}}}{r} \left(\frac{a_s}{k} \right)^2, \quad (3.13)$$

⁴Available from github.com/hpparvi/PyDE.

⁵stanford.edu/~mwaskom/software/seaborn

⁶PyFITS is a product of the Space Telescope Science Institute, which is operated by AURA for NASA

where a_s is the scaled semi-major axis, r the inverse of the phase integral, and k the planet-star radius ratio.

3.4.8.2 Brightness temperature

The brightness temperature, T_p , is derived from the emitted flux estimate F_{pe} using

$$F_{pe} = k^2 \frac{B(T_p, \lambda)}{B(T_\star, \lambda)} = k^2 \frac{\exp(hc/\lambda k_B T_\star) - 1}{\exp(hc/\lambda k_B T_p) - 1}, \quad (3.14)$$

which gives us

$$T_p = \frac{hc}{\lambda k_B \ln \left(1 + k^2 \frac{\exp(hc/\lambda k_B T_\star) - 1}{F_{pe}} \right)}. \quad (3.15)$$

3.4.8.3 Planetary mass from ellipsoidal variation

Since we parametrize the ellipsoidal variation using the planet-star mass ratio, the planetary mass is obtained directly from the assumed stellar mass by using Equation 3.8.

3.5 Results

The fitted parameters of the RV and transit model are shown in Table 3.3, together with the derived physical properties of the planet Kepler-91 b. We included in our model a RV linear trend to account for the presence of a potential companion in the system. To assess if the introduction of this parameter is justified, we use the Bayesian information criterion (BIC; Schwarz 1978; Liddle 2004, 2007), which rewards better-fitting models, but penalizes models that are overly complex. When comparing two models, the one with the lowest BIC is preferred. The BIC is defined by

$$\text{BIC} = -2 \ln \mathcal{L}_{\max} + k_p \ln N \quad (3.16)$$

where \mathcal{L}_{\max} is the maximum likelihood for a particular model, k_p is the number of parameters and N the number of data points. We calculated the BIC for a model with and without a RV linear trend included. The derived values are $\text{BIC}_{\text{trend}} = -361$ and $\text{BIC}_{\text{no trend}} = -336$, which gives $\Delta\text{BIC} = 25$. This provides strong positive evidence in favor of the model with the RV linear trend. Moreover, the posterior distribution of the linear RV trend value is significantly non-zero

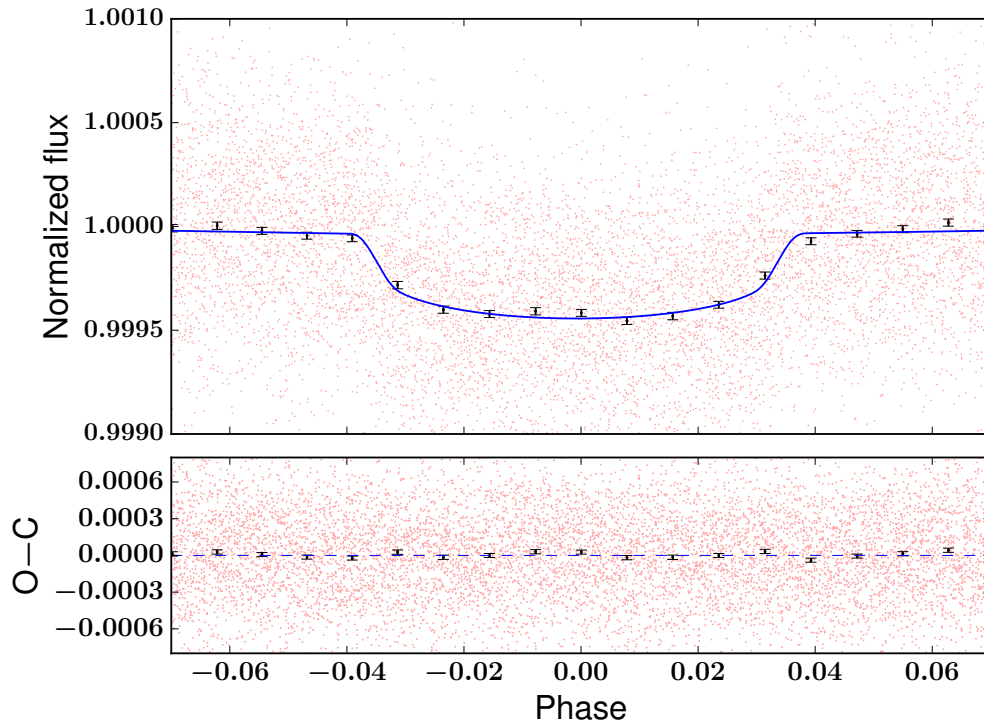


Figure 3.1: The upper panel shows the phase-folded light curve (red points) centered at the mid-transit time, together with the best-fit transit model (blue solid line). The data were binned (black points) with 500 observed points per bin. The lower panel shows the residuals from the transit model.

(see Fig. B.1 of Appendix B), and evolves nicely when more RV data sets are introduced. We then conclude that the RV trend of $\dot{\gamma} = -0.0523_{-0.0093}^{+0.0098} \text{ m s}^{-1} \text{ d}^{-1}$ is most likely real and caused by an additional body in the system.

Figure 3.1 shows the transit light curve of Kepler-91 centered at the mid-transit time, together with the residuals from the fit. Additionally, Fig. 3.2 plots the Kepler-91 light curve including the effects of the out-of-transit modulations together with the RV dataset of FIES, CAFE, HRS and HDS, and the respective best-fit models to the data.

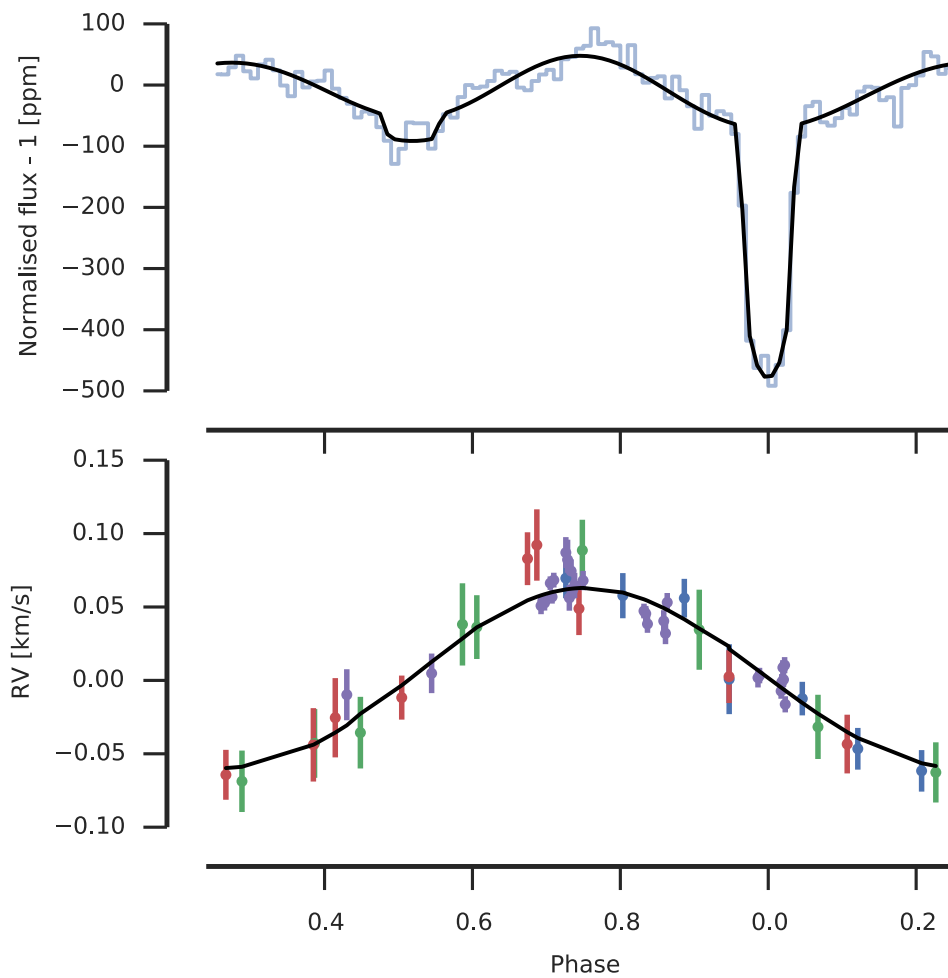


Figure 3.2: The upper panel shows the phase-folded and binned *Kepler* light curve (blue line) and the model including the effects of reflection/emission from the planet, ellipsoidal variations and Doppler beaming (black line). The lower panel plots the FIES (blue), CAFE (green), HRS (red), and HDS (purple) radial velocity dataset with the best-fit Keplerian model (black line).

Table 3.2: Model parameterization and priors.

Name	Unit	Priors
Mid-transit time	d	$U(t_0 - 0.02, t_0 + 0.02)$
Period	d	$N(p_0, 0.001)$
Area ratio	R_\star^2	$U(0.016^2, 0.025^2)$
Stellar density	g cm^{-3}	$N(0.0073, 10^{-4})$
Impact parameter		$U(0, 1)$
Sampler linear limb darkening		$U(0, 1)$
Sampler quadratic limb darkening		$U(0, 1)$
Average LC error		$U(0.0001, 0.0006)$
Photometry baseline		$U(0.999, 1.001)$
Reflected amplitude		$U(0, 6 \times 10^{-5})$
Emission amplitude		$U(0, 5 \times 10^{-5})$
$\sqrt{e} \cos \omega$		$U(-0.3, 0.3)$
$\sqrt{e} \sin \omega$		$U(-0.3, 0.3)$
EV mass ratio ¹	M_\star	$U(2 \times 10^{-4}, 7 \times 10^{-3})$
RV semi-amplitude	km/s	$U(0, 0.1)$
FIES baseline	km/s	$N(-62.06, 0.02)$
CAFE baseline	km/s	$N(-62.28, 0.02)$
HRS baseline	km/s	$N(-0.01, 0.02)$
HDS baseline	km/s	$N(-0.03, 0.02)$
FIES add. error	km/s	$U(0, 0.01)$
CAFE add. error	km/s	$U(0, 0.01)$
HRS add. error	km/s	$U(0, 0.01)$
HDS add. error	km/s	$U(0, 0.01)$
Linear RV trend	km/s/d	$U(-0.01, 0.01)$

¹ EV refers to ellipsoidal variation.

Table 3.3: Orbital parameters of Kepler-91 system.

Model parameter	Value
Planet orbital period P (day)	6.246694 ^{+0.000028} _{-0.000030}
Planetary mid-transit epoch T_0 (BKJD) ¹	136.389935 ^{+0.004090} _{-0.003648}
Stellar density ρ_\star (g/cc)	0.0069 ^{+0.0003} _{-0.0003}
Planet-to-star area ratio R_p^2/R_\star^2	0.000472 ^{+0.000048} _{-0.000029}
Impact parameter b	0.875 ^{+0.007} _{-0.008}
Sampler linear limb darkening a_1	0.539 ^{+0.148} _{-0.125}
Sampler quadratic limb darkening b_2	0.323 ^{+0.373} _{-0.236}
$\sqrt{e} \cos \omega$	0.154 ^{+0.015} _{-0.019}
$\sqrt{e} \sin \omega$	-0.066 ^{+0.060} _{-0.053}
Average photometric error σ_{LC}	0.000380 ^{+0.000001} _{-0.000001}
Photometry baseline F_{bl}	0.999992 ^{+0.000006} _{-0.000006}
Reflected flux from the planet F_{pr}	23.826 ^{+5.599} _{-5.814}
Emitted flux from the planet F_{pe}	13.211 ^{+6.920} _{-6.445}
Planet-to-star mass ratio M_{ev}	0.000873 ^{+0.000296} _{-0.000125}
Radial velocity semi-amplitude K (km s ⁻¹)	0.061 ^{+0.003} _{-0.003}
FIES zero-point z_{FIES} (km s ⁻¹)	-62.048 ^{+0.005} _{-0.005}
FIES error term σ_{FIES} (km s ⁻¹)	0.004 ^{+0.003} _{-0.003}
CAFE zero-point z_{CAFE} (km s ⁻¹)	-62.279 ^{+0.008} _{-0.007}
CAFE error term σ_{CAFE} (km s ⁻¹)	0.004 ^{+0.004} _{-0.003}
HRS zero-point z_{HRS} (km s ⁻¹)	-0.010 ^{+0.007} _{-0.007}
HRS error term σ_{HRS} (km s ⁻¹)	0.0051 ^{+0.003} _{-0.003}
HDS zero-point z_{HDS} (km s ⁻¹)	-0.033 ^{+0.003} _{-0.003}
HDS error term σ_{HDS} (km s ⁻¹)	0.007 ^{+0.001} _{-0.002}
Radial velocity linear trend $\dot{\gamma}$ (m s ⁻¹ d ⁻¹)	-0.0523 ^{+0.0098} _{-0.0093}
Derived parameters	
Planet-to-star radius ratio R_p/R_\star	0.0217 ^{+0.0011} _{-0.0007}
Scaled semi-major axis a/R_\star	2.423 ^{+0.035} _{-0.035}
Orbit eccentricity e	0.0306 ^{+0.0064} _{-0.0047}
Argument of periastron ω (deg)	-23.145 ^{+20.898} _{-17.648}
Orbital inclination i (deg)	69.075 ^{+0.482} _{-0.492}
Linear limb darkening coefficient u	0.472 ^{+0.511} _{-0.337}
Quadratic limb darkening coefficient v	0.252 ^{+0.374} _{-0.531}
Planet mass M_p (M _{Jup})	0.67 ^{+0.06} _{-0.06}
Planet radius R_p (R _{Jup})	1.369 ^{+0.096} _{-0.086}
Planet mass from EV (M _{Jup})	1.117 ^{+0.397} _{-0.216}
Brightness temperature T_b (K)	2752 ⁺¹³⁷ ₋₁₈₈
Bond albedo A_B	0.194 ^{+0.053} _{-0.050}

¹ BKJD is the time system used by *Kepler* and is defined by the Barycentric Julian Date (BJD) - 2454833.

3.6 Discussion

3.6.1 Physical properties of the planet

Kepler-91 b is a sub-Jupiter giant planet with a mass of $M_p = 0.67^{+0.06}_{-0.06} M_{\text{Jup}}$ and a radius of $R_p = 1.369^{+0.096}_{-0.086} R_{\text{Jup}}$ yielding a planetary density of $\rho_p = 0.26^{+0.06}_{-0.06} \rho_{\text{Jup}}$. The planet is not expected to possess a large core given the modest amount of metals in its host giant star ($[\text{Fe}/\text{H}] = 0.10 \pm 0.08$ dex). As lower planet core masses increases the planet radius (Guillot et al. 2006; Enoch et al. 2012) and Kepler-91 b presents a moderate radius anomaly of $R \sim 0.1$ as defined by Laughlin et al. (2011), we used the models of Fortney et al. (2007) for a coreless planet – interpolated to the insolation and age of Kepler-91 b – to estimate a radius of $1.118 R_{\text{Jup}}$ for Kepler-91 b. This is more than 2σ smaller than the measured radius of the giant planet, thus the planet is slightly inflated. Fig. 3.3 shows the radius-mass relation for all the transiting hot Jupiters defined to have masses of $0.1 < M_p < 2 M_{\text{Jup}}$ ⁷. The planets with inflated radii concentrate between 0.3 - $2 M_{\text{Jup}}$ with a peak around $1 M_{\text{Jup}}$.

Several mechanisms have been proposed to explain the large radii of transiting exoplanets such as kinetic heating (Guillot & Showman 2002), tidal heating (Bodenheimer et al. 2001, 2003), enhanced atmospheric opacities (Burrows et al. 2007), semi convection (Chabrier & Baraffe 2007) and more recently Ohmic heating (Perna et al. 2010; Batygin & Stevenson 2010; Wu & Lithwick 2013). Kinetic and Ohmic heating are tightly related to the stellar irradiation received by the planet. It has become clear that there is a correlation between the inflated planetary radii of hot Jupiters and the stellar incident flux (Weiss et al. 2013; Lopez & Fortney 2016) whereas this correlation is absent for moderately irradiated planets with incident fluxes of $\lesssim 2 \times 10^8 \text{ erg s}^{-1} \text{ cm}^{-2}$ (Miller & Fortney 2011; Demory & Seager 2011). Kepler-91 b is a highly irradiated planet with $\langle F \rangle = (4.00 \pm 0.31) \times 10^9 \text{ erg s}^{-1} \text{ cm}^{-2}$ and is expected that the previous two mechanisms might have contributed to some extent to the inflation of its radius. Figure 3.4 shows the relation between the planet radii and the equilibrium temperature for the transiting hot Jupiters. Color coded is the incident flux on the planets. It is clear that higher levels of irradiation (closely related to the planet equilibrium temperature) leads to larger planet radii. The position of Kepler-91 b in the plot shows that it is within the hot Jupiters with the highest levels of irradiation, and thus the highest equilibrium temperature.

With a radius anomaly of $R \sim 0.1$ and an equilibrium temperature of $T_{\text{eq}} = 2186 \pm 16 \text{ K}$, Kepler-91 b is far below the relation of $R \propto T_{\text{eq}}^{1.4}$ found by Laughlin et al. (2011) for a sample of 90 transiting planets (see their Figure 2). It is expected that Ohmic heating should yield a higher dependence on temperature of $R \propto T_{\text{eq}}^{2.66}$ (Laughlin et al. 2011), implying that this is not the main

⁷Data acquired from <http://www.exoplanets.org>

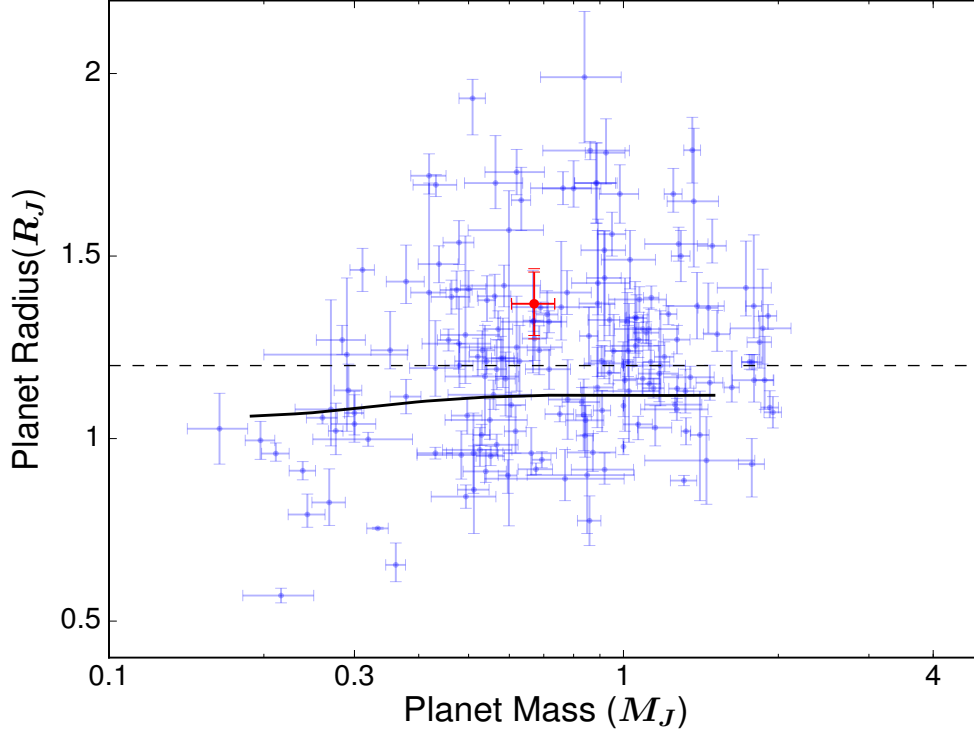


Figure 3.3: Planetary radius as a function of planet mass for all the transiting planets with $0.1 < M_p < 2 M_{\text{Jup}}$. Also shown is the model from Fortney et al. (2007) for a coreless planet interpolated to the insolation and age of Kepler-91 b (black solid line). The black dashed line marks the approximate limit of $R_p \sim 1.2 R_{\text{Jup}}$ defining an inflated planet (Lopez & Fortney 2016). The position of Kepler-91 b is shown in red color. The radius of the planet is more than 2σ above the predicted value from the Fortney et al. model.

source of inflation for the radius on Kepler-91 b. On the other hand, kinetic heating might lead to a smaller dependence with temperature in the form of $R \propto T_{\text{eq}}^{0.67}$, suggesting that this mechanism might be a relevant source of additional heat to inflate the planet radius. This result agrees with the findings of Enoch et al. (2012) for a larger sample of transiting planets in which they find a weaker dependence of the radius with effective temperature ($R_p \propto T_{\text{eq}}^{0.9}$) for Jupiter-mass planets suggesting that kinetic heating is mainly responsible for the inflated radii of the planets in the sample. However, nor kinetic heating or any of the previously mentioned mechanisms can explain the totality of inflated exoplanet radii (Fortney & Nettelmann 2010; Lecante et al. 2010; Perna et al. 2012), thus more complex models and also observations are necessary for a full understanding of this phenomenon.

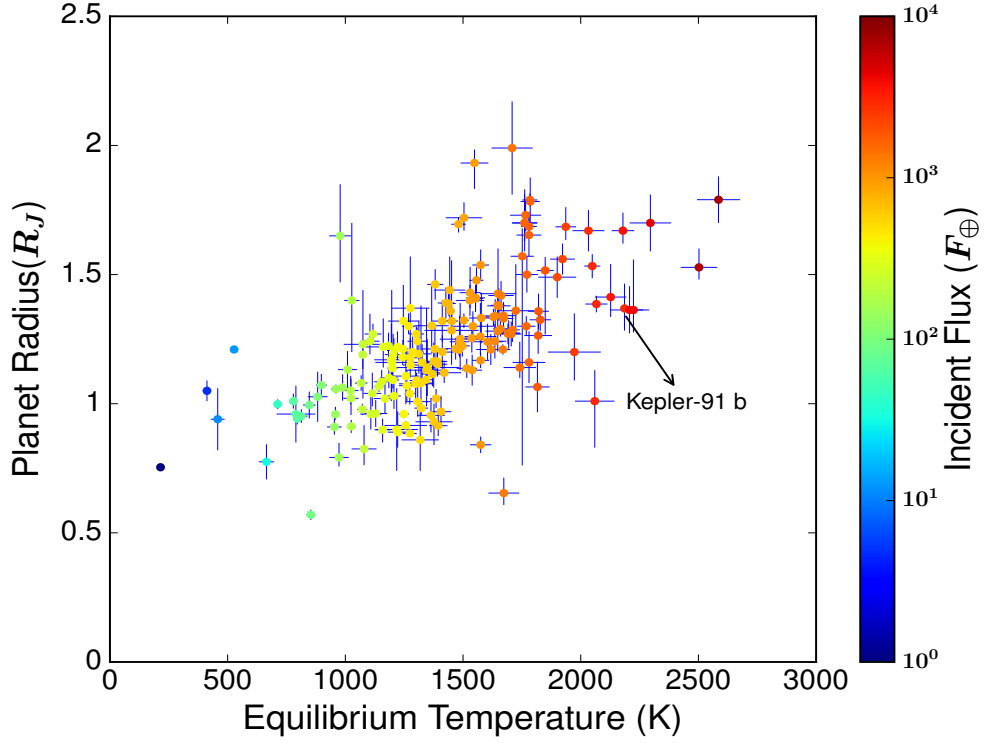


Figure 3.4: Planetary radius as a function of the equilibrium temperature for all the transiting hot Jupiters. The current incident flux on the planets is color coded. There is an evident correlation between the flux received by the planet and its radius. Kepler-91 b is a highly irradiated planet with an equilibrium temperature of $T_{\text{eq}}=2186 \pm 16$ K that falls well within the trend observed for the rest of hot Jupiters.

3.6.2 Eccentricity

The implementation of our MCMC fitting code uses a parametrization of the form $\sqrt{e} \cos \omega$ and $\sqrt{e} \sin \omega$. This scaling allows the parameter space to be explored efficiently at small eccentricities (Ford 2006), and ensures a uniform prior on e . We derived an eccentricity of $e = 0.0306^{+0.0064}_{-0.0047}$, which is small, but significant at the 6σ level. The non-zero eccentricity of Kepler-91 b has been suspected before (Lillo-Box et al. 2014a; Barclay et al. 2015) and is somehow intriguing (see Fig. 3.5). For such a close-in planet, the orbit should have already been fully circularized due to tidal interactions between the planet and the host giant star. The circularization timescale is given by (Adams & Laughlin 2006):

$$\tau_{\text{circ}} \approx 1.6 \text{ Gyr} \left(\frac{Q_p}{10^6} \right) \left(\frac{M_p}{M_J} \right) \left(\frac{M_*}{M_\odot} \right)^{-1.5} \left(\frac{R_p}{R_J} \right)^{-5} \left(\frac{a}{0.05 \text{ au}} \right)^{6.5} \quad (3.17)$$

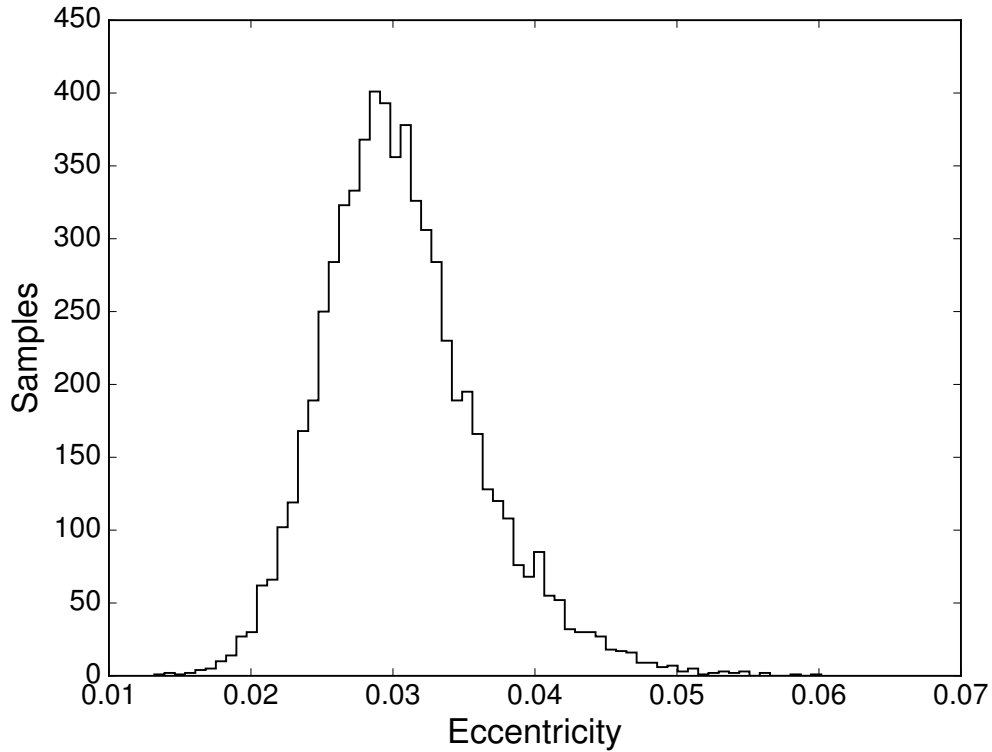


Figure 3.5: Posterior distribution for the orbital eccentricity of the planet Kepler-91 b. The derived eccentricity is small, but significant at the 6σ level, and we can rule out with a high probability a circular orbit.

where Q_p is the tidal dissipation parameter. The value of Q_p is poorly constrained within the range $Q_p = 10^5 - 10^6$ (Goldreich & Soter 1966; Peale 1999; Meibom & Mathieu 2005). More recently, Quinn et al. (2014) estimated a value of $\log Q_p = 6.14^{+0.41}_{-0.25}$ for hot Jupiters. Assuming this value for the tidal quality factor we estimate a circularization timescale of $\tau_{circ} = 1.8 \pm 0.7$ Gyr; much smaller than the age of the system $t_{age} = 4.86 \pm 2.13$ Gyr. Adopting smaller values for Q_p implies even lower values for τ_{circ} . A non-zero orbital eccentricity might be a tracer of the migration history of the planet, but as $\tau_{circ} < t_{age}$ is difficult to link the eccentricity to primordial migration. Other possibilities to explain the eccentricity of hot Jupiters are tidal interaction with the central star (e.g., Dobbs-Dixon et al. 2004), secular perturbation from an additional object (e.g., Takeda & Rasio 2005) or resonant interaction with another planet in the system (e.g., Ribas et al. 2008).

The case of a Jupiter-mass planet in a low-order mean motion resonance (MMR) configuration ($P_2 < 30$ days) is hard to reconcile with our data as we should have been able to detect its RV signal. Additionally, a massive body locked in these MMRs might have induced transit timing variations in the light curve of Kepler-91 b, which is not observed in the data (Holczer et al. 2016). The RV linear trend of $0.0523 \text{ m s}^{-1} \text{ d}^{-1}$ requires a hypothetical massive planet

($\sim 1 M_{\text{Jup}}$) in a circular orbit with a period of ~ 1870 days (~ 3 au); far too large for a MMR. For a saturn-mass planet ($\sim 0.3 M_{\text{Jup}}$), however, we are only sensitive to 1:2 and 3:2 MMR as longer periods for a resonant planet are below the RV detection limit of $\sim 19 \text{ m s}^{-1}$.

The small circularization timescale derived for Kepler-91 b argues against tidal heating for explaining the eccentricity of the planet. However, this calculation depends on the tidal quality factor, Q_p , which is not known in detail for each particular planet. In fact, the only planet for which Q_p is known is Jupiter (Lainey 2009). This value depends on the internal structure of planets as well as the frequencies and amplitudes of tides, and it is likely that it may differ from planet to planet. Theoretical studies of dissipation of dynamical tides in rotating giant planets have shown that the tidal Q values can have large fluctuations up to $\sim 10^9$ depending on the spin rate and internal structure of the planet (Ogilvie & Lin 2004; Wu 2005). Moreover, Matsumura et al. (2008) studied the origin of the eccentricities of close-in planets showing that a large fraction of the transiting eccentric planets can be explained if $10^5 \lesssim Q_p \lesssim 10^9$. For the case of Kepler-91 b, in order to have $\tau_{\text{circ}} \approx t_{\text{age}}$ a value of $Q_p \sim 10^{6.5}$ is required, which is within 1σ of the tidal dissipation value estimated by Quinn et al. (2014) for hot Jupiters. A larger value of Q_p in Kepler-91 b might serve as a natural explanation for the eccentricity of the planet, but also for its slightly inflated radius, as tidal heating might dissipate in the interior of the planet, hence expanding its radius (Bodenheimer et al. 2001, 2003; Gu et al. 2003).

Another possibility for pumping up the eccentricity of Kepler-91 b is the perturbation of the orbit by an unseen companion via Kozai-type oscillations (Kozai 1962; Lidov 1962). If the mutual inclination angle between the two bodies is large ($i \gtrsim 40^\circ$) the Kozai mechanism might become relevant. Such configuration may result from planet-planet scattering after the dissipation of the protoplanetary disk (e.g., Chatterjee et al. 2008; Nagasawa et al. 2008). Given the relatively low orbital inclination of $i = 69.08^\circ$, a hypothetical planet perturbing the eccentricity of Kepler-91 b could have inclinations of $\lesssim 30^\circ$ complicating the detection for low planetary masses. On the other hand, if the observed RV trend of $0.0523 \text{ m s}^{-1} \text{ d}^{-1}$ is being caused by an additional planet in the system, this object might be the responsible for inducing an oscillation in Kepler-91 b eccentricity. However, this possibility cannot be confirmed with the available data and additional observations are needed to better assess the nature of this trend.

3.6.3 Close-in planets around evolved stars

Figure 3.6 shows the semi-major axis of planets around MS host (black points) and red giant stars (red circles) as a function of the stellar radius. Also, plotted in green are the close-in planets discovered around subgiant stars (defined to have $R_\star < 4 R_\odot$ and $3.5 < \log g < 4$). It is clear that when compared to MS host, giant stars show a scarcity of planets in close-in orbits

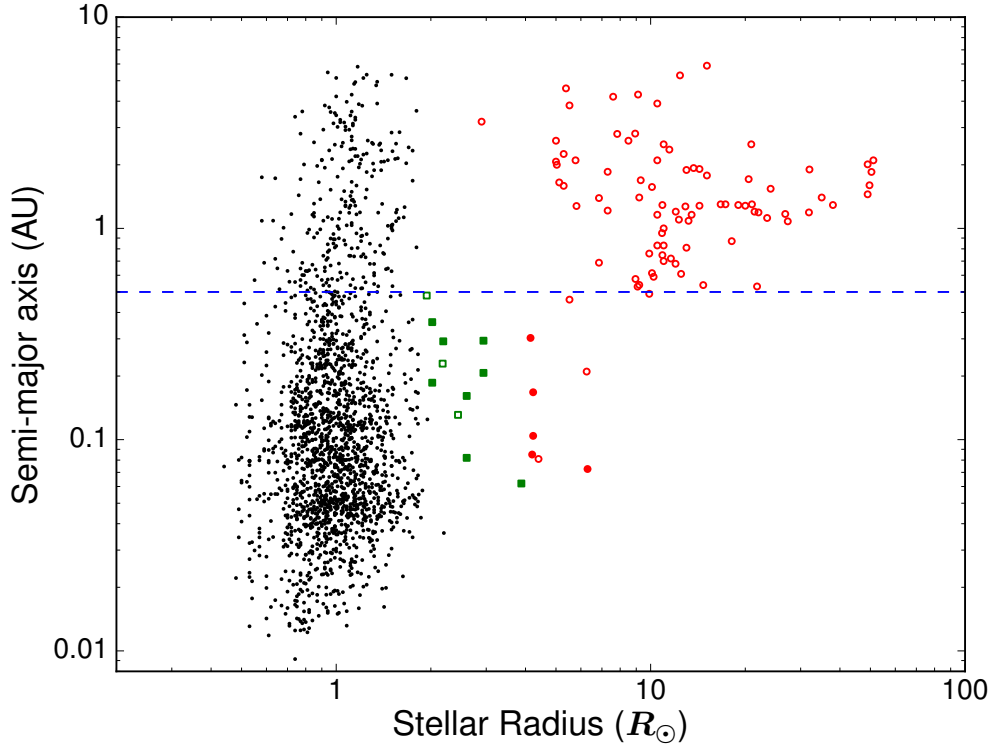


Figure 3.6: Semi-major axis of planets around MS (black dots), giant (red circles) and subgiant stars (with $a < 0.5$ au, green squares) as a function of the host-star radius. The blue dashed line marks the value of $a = 0.5$ au to define a close-in planet. Transiting planets are highlighted with filled symbols. The *Kepler* mission alone (including K2) has discovered 65% of the close-in planets around evolved stars.

($a < 0.5$ au). In fact, Kepler-91 b is the only gas giant hot Jupiter planet ($a < 0.1$ au) found to orbit a star with $R_{\star} > 6 R_{\odot}$. This dearth of close-in planets around evolved stars has been noted before by RV surveys (e.g., Johnson et al. 2007; Sato et al. 2008) and currently there are two different explanations: close-in gas giant planets are not formed around intermediate-mass stars in the first place, owing to the differences in the structure of the protoplanetary disk with respect to low-mass stars (Kretke et al. 2009). Alternatively, if they do form, they don't easily migrate inwards, owing to the short dissipation timescale of the disk (Burkert & Ida 2007; Currie 2009). The second possibility is that these close-in planets do migrate inward, but are tidally engulfed by their host star during the later stages of stellar evolution, as a result of the stronger star-planet tidal interaction, which is proportional to R_{\star}^5 (Villaver & Livio 2009; Kunitomo et al. 2011; Schlaufman et al. 2013; Villaver et al. 2014).

An interesting trend can be observed in Fig. 3.6: all of the planet-hosting giant stars are in a relatively early phase of the post-MS evolution. That is, they are just evolving off the MS or ascending through the RGB. On the other hand, there are no close-in planets discovered around more evolved red giants with radii of $R_{\star} \gtrsim 10 R_{\odot}$. This suggests that the absence of close-in

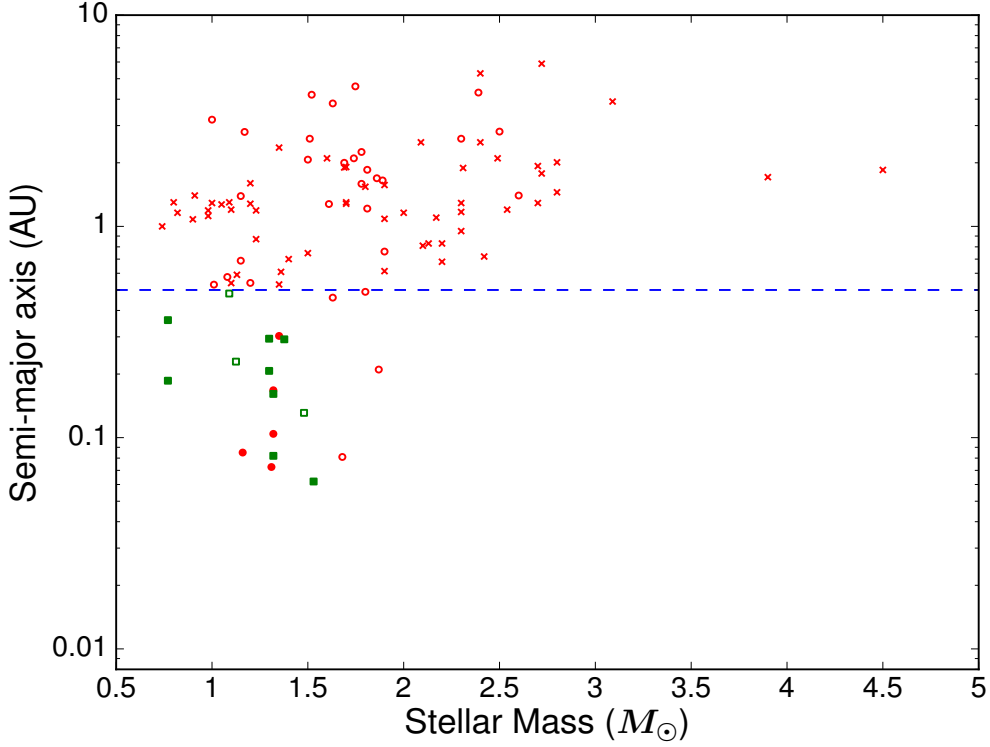


Figure 3.7: Semi-major axis of planets around giant (red symbols) and subgiant stars (with $a < 0.5$ au, green squares) as a function of the host-star mass. The blue dashed line marks the value of $a = 0.5$ au to define a close-in planet. Transiting planets are highlighted with filled symbols. The giant stars with a radius larger than $10 R_{\odot}$ are marked with a cross.

planets in stars with $R_{\star} \gtrsim 10 R_{\odot}$ is due to the planetary engulfment during the RGB phase. This is reinforced by the fact that there seems to be no significant difference between the masses of the giant stars with close-in planets and the masses of planet-hosting giants with $a > 0.5$ au and $R_{\star} \gtrsim 10 R_{\odot}$ (see Fig. 3.7). For the case of Kepler-91 b, we can estimate the timescale of engulfment due to tides following [Schlaufman et al. \(2013\)](#):

$$\tau_{dec} = 10 \text{ Gyr} \frac{Q_{\star}/k_{\star}}{10^6} \left(\frac{M_{\star}}{M_{\odot}}\right)^{0.5} \left(\frac{M_p}{M_J}\right)^{-1} \left(\frac{R_{\star}}{R_{\odot}}\right)^{-5} \left(\frac{a}{0.06 \text{ au}}\right)^{6.5} \quad (3.18)$$

where Q_{\star} is the tidal quality factor of the star and k_{\star} is the Love number. As with the tidal quality factor for the planet, Q_p , the value of Q_{\star} is largely unknown, particularly for giant stars. If we assume the standard value of $Q_{\star}/k_{\star} = 10^6$, we estimate a tidal decay time of $\tau_{dec} \approx 6$ Myr for Kepler-91 b. Additionally, all the hot gas-giant planets ($a < 0.1$ au) have tidal decay times of $\lesssim 120$ Myr, implying that they will be engulfed during the RGB phase of their host stars. On the

other hand, for the warm gas-giants ($0.1 < a < 0.5$ au), their fate may vary depending on each particular case and detailed modeling is necessary to drive a definitive conclusion about them.

3.6.4 Implications for planet migration

Besides Kepler-91 b, eight planets in seven systems have been found to orbit red giant stars (defined to have $R_{\star} > 4 R_{\odot}$ and $\log g < 3.5$) with a semi-major axis of $a < 0.5$ au : 8 Umi b (Lee et al. 2015), HIP 67851 b (Jones et al. 2015a), HD 102956 b (Johnson et al. 2010), TYC 3667-1280 b (Niedzielski et al. 2016b), Kepler-56 b,c (Steffen et al. 2013; Huber et al. 2013b), Kepler-432 b (Ortiz et al. 2015; Ciceri et al. 2015; Quinn et al. 2015) and EPIC 211351816.01 b (Grunblatt et al. 2016). The fact that we are starting to unveil this population of warm planets, mainly thanks to the discovered transiting planets (see Fig. 3.6), implies that these objects migrated, most likely through gravitational scattering, to reach their current positions. This is provided that we accept the common belief that giant planets form beyond the ice line and then migrated inward to reach their current positions.

It has been suggested before that hot and warm Jupiters can form via high-eccentricity migration: an external perturber induces an eccentricity oscillation in the orbit of the planet followed by efficient tidal dissipation which causes the orbit of the inner planet to shrink during periastron passages (Wu & Lithwick 2011; Dong et al. 2014; Petrovich & Tremaine 2016). Recently, Lillo-Box et al. (2016b) showed that the close-in planets around evolved stars (including giants and subgiants) tend to also have a companion in the system. That is, there seems to be a prevalence of multiplanetary systems around evolved stars hosting close-in planets. This observational evidence gives support to the idea that gravitational migration may be the responsible for the orbits of close-in planets around evolved stars. However, several recent studies have suggested that hot and also warm Jupiters can form *in situ* by core accretion from originally low-mass closely packed planets (Lee et al. 2014; Batygin et al. 2015; Boley et al. 2016; Huang et al. 2016). Additionally, Schlaufman & Winn (2016) found that hot Jupiters are just as likely than warm Jupiters to have long-period Jupiter-mass companions inside the water-ice line, which is not expected if hot Jupiters are produced via high-eccentricity migration (e.g., Mustill et al. 2015). This does not agree with previous studies of *Kepler* planet candidates showing that Jupiter-like planets are less likely to have additional planets in the system than more distant planets (Latham 2011; Steffen et al. 2012). A testable expectation of *in situ* formation according to Batygin et al. (2015) is that hot Jupiters should frequently be accompanied by additional low-mass planets with periods shorter than ~ 100 days. Our RV data of Kepler-91 is only sensitive to detect Saturn-mass ($\sim 0.3 M_{\text{Jup}}$) planets for periods shorter than ~ 17 days, thus we cannot exclude the presence of lower mass planets or even Saturn-like planets with periods greater than 17 days. Future RV observations

are encouraged to assess the nature of the RV trend that we observe in the data and to investigate the presence of any low-mass planet that might still remain elusive in the system.

3.7 Summary

We have used our high precision RV data of the giant star Kepler-91, together with additional publicly available RV measurements, to provide an improved orbital solution for the Kepler-91 system. We model the RV jointly with the transit photometry taking into account the out-of-transit modulation imprinted in the light curve of the star by the giant planet. Particularly, we derived a planet mass of $M_p = 0.67_{-0.06}^{+0.06} M_{\text{Jup}}$ for the hot Jupiter and a planet radius of $R_p = 1.37_{-0.09}^{+0.08} R_{\text{Jup}}$ showing that the planet is slightly inflated.

We derived a significant non-zero eccentricity of $e = 0.0306_{-0.0047}^{+0.0064}$ that is in conflict with the circularization time expected for such a close-in planet. A larger value of the planet dissipation factor, Q_p , than the one usually assumed for giant planets might be able to explain the non-zero eccentricity of the orbit by means of tidal heating. This could somehow also contribute to explain the slightly inflated radius of Kepler-91 b. Alternatively, an undetected additional companion in the system might be responsible for pumping up the eccentricity of the hot Jupiter. We have detected a RV linear trend of $0.0523 \text{ m s}^{-1} \text{ d}^{-1}$ that can be generated by a companion in the system, but more measurements are needed to fully constrain the origin of this trend.

Kepler-91 b is part of the growing number of close-in planets discovered around giant stars. Furthermore, it is the only hot Jupiter found to transit an RGB star with $R_\star > 6 R_\odot$. We estimated that the planet will be tidally engulfed by its host star in ~ 6 Myr. A similar fate expect the rest of the hot Jupiters ($a < 0.1$ au) orbiting evolved stars (giants and subgiants). This may be an indication that close-in planets orbiting evolved stars experience an increased planet-star tidal interaction at the latter stages of the RGB phase, being consequently swallowed by their hosts. On the other hand, as all of the detected close-in planets around giant stars are in a relatively early phase of the giant stellar evolution, they (for now) have avoided being engulfed by their host stars. This suggests that the tidal interaction at this early stage of the giant evolution is not that strong as previously thought. Additionally, as the number of close-in planets around evolved hosts continue to increase, it may be that an observational bias could be partially responsible for the lack of short-period planets around evolved stars.

The detection of close-in planets around giant stars is difficult both with the transit – small planet-to-star radius ratio – and the RV method – intrinsic stellar oscillations. However, data from Kepler has started to unveil this population of objects that had remain elusive to RV surveys in the past. It has also been demonstrated that the signal of the these massive close-in planets can

be detected with the RV technique besides the intrinsic jitter expected for more evolved stars. Although the detection of low-mass planets is still difficult, this invites us to be optimistic about next generation instrumentation aimed to detect exoplanets in the near future. For example, the next space transit missions TESS ([Ricker et al. 2014](#)) and CHEOPS ([Broeg et al. 2013](#)) will be sensible to detect the transit of a Jupiter-like planet around a star with a radius of $10 R_{\odot}$, thus we can expect several new close-in planets around giant stars coming from these missions. Combining transit data with asteroseismology has the potential to provide the best characterized systems that will allow the investigation of this population of close-in planets in great detail.

The S-type planet HD 59686 Ab in an eccentric close binary

This Chapter presents the discovery and characterization of a system composed of a close-separation eccentric binary harboring the circumstellar planet HD 59686 Ab. The Chapter is a version of the article [Ortiz et al. \(2016\)](#).

4.1 Context

Since the discovery of the first extrasolar planet around a solar-like star by [Mayor & Queloz \(1995\)](#), more than 3000 exoplanets have been confirmed ([Schneider et al. 2011](#))¹. Of these planets, about 75% have been discovered by the transit method, which has greatly benefited from the data obtained with the *Kepler* Space Telescope ([Borucki et al. 2010](#)). Moreover, in 2014 alone, 715 new planets in 305 systems were detected by *Kepler*, almost doubling the number of exoplanets known at that time ([Lissauer et al. 2014](#); [Rowe et al. 2014](#)), and more recently, [Morton et al. \(2016\)](#) have confirmed nearly 1280 new transiting *Kepler* planets based on probabilistic validation methods. Most of the remaining 25% of planets have been found using the radial velocity technique. The spectral characteristics of solar-type main-sequence stars are favorable for RV measurements, which has made these stars the targets of the majority of the RV planet searches. However, a growing number of research groups are successfully searching for planets around evolved subgiant and giant stars (e.g., [Döllinger et al. 2009](#); [Johnson et al. 2010, 2011](#);

¹<http://www.exoplanet.eu>

Sato et al. 2013; Jones et al. 2015a,b; Niedzielski et al. 2015; Reffert et al. 2015; Wittenmyer et al. 2016).

There are currently 95 known planetary companions orbiting around giant stars, of which 46% have been published during the past three years². Giant stars allow us to access more massive stars than those typically observed on the MS. Early MS stars are normally avoided in RV planet searches as they rotate faster and have too few absorption lines for reliable high-precision RV determinations. On the other hand, evolved stars, such as K giants, have suitable and less broadened absorption lines for RV measurements, low rotational velocities, and much higher masses than late-type MS stars. Additionally, K-giant RV surveys also allow investigating how planetary systems evolve after the host star leaves the MS (Villaver & Livio 2009; Kunitomo et al. 2011; Villaver et al. 2014).

Of the known extrasolar planets, about 7% orbit in multiple star systems³, although this number suffers from an observational bias as most of the exoplanet surveys systematically avoid binary stars in their samples. For K-giant stars specifically, only four out of 72 known stars harboring planets are members of stellar multiple systems: 11 Com (Liu et al. 2008), γ^1 Leo (Han et al. 2010), 91 Aqr (Mitchell et al. 2013), and 8 UMi (Lee et al. 2015). Finding planets in multiple star systems allows us to learn more about the processes of planetary formation and evolution. This is particularly important, since $\sim 50\%$ of the MS stars in our solar neighborhood are members of binaries or multiple systems (Duquennoy & Mayor 1991; Raghavan et al. 2010). The frequency of these planets may have a strong influence on the overall global frequency of extrasolar planets, allowing us to study the efficiency of planet formation mechanisms. Moreover, if there is any difference in the properties of planets in binary systems with respect to planets orbiting single stars, this may unveil effects caused by additional companions in stellar systems (Desidera & Barbieri 2010; Roell et al. 2012).

The majority of known planets in binary systems are in S-type orbits (circumstellar planets), meaning that the planet orbits around one member of the binary pair (e.g., Howard et al. 2010; Buchhave et al. 2011; Anderson et al. 2014), as opposed to P-type configurations (circumbinary planets), where the planet orbits both stars beyond the binary orbit (e.g., Doyle et al. 2011; Orosz et al. 2012a,b; Welsh et al. 2012; Bailey et al. 2014). Most of the known S-type planets reside in wide-separation binaries ($a_B \gtrsim 100$ au) where the influence of the stellar companion on the formation process of the inner planet can probably be neglected. However, there are some interesting systems detected in close-separation binaries in which the stellar companion is located at roughly 20 au: Gliese 86 (Queloz et al. 2000), γ Cep (Hatzes et al. 2003), HD 41004 (Zucker et al. 2004), and HD 196885 (Correia et al. 2008). The existence of planets in tight binary systems ($a_B \lesssim 20$ au) presents a serious challenge to current planet formation theories (Hatzes

²<http://www.lsw.uni-heidelberg.de/users/sreffert/giantplanets.html>

³<http://www.univie.ac.at/adg/schwarz/multiple.html>

& Wuchterl 2005; Rafikov 2005). Moreover, supporting the theoretical expectation, Wang et al. (2014) found evidence that planet formation is effectively suppressed in binary systems with separations of less than 20 au.

In this chapter, we report the discovery of a planet orbiting the giant star HD 59686, which we refer to as HD 59686 A, and which is part of a close-separation binary system with $a_B = 13.56$ au. The chapter is organized as follows: In Sect. 4.2 we describe our sample selection and observations. Section 4.3 presents the stellar properties of the star and the Keplerian fit to the RV data from the Lick observatory. In Sect. 4.4 we validate the planetary hypothesis for the RV variations in HD 59686 A using infrared RVs taken with CRILES, spectral activity indicators, and the available photometry. In Sect. 4.5 we describe the high-contrast imaging observations of HD 59686 A obtained at the Large Binocular Telescope (LBT) to image the stellar companion, including reduction of the data and constraints on the stellar companion to the giant star. In Sect. 4.6 we discuss the properties of the HD 59686 system, focusing on the nature of the stellar companion and the implications for the formation of planets in tight binaries. Finally, in Sect. 4.7 we present our conclusions.

4.2 Observations

We have continuously monitored the RVs of 373 G- and K-giant stars for more than a decade, resulting in several published planet detections (Frink et al. 2002; Reffert et al. 2006; Quirrenbach et al. 2011; Mitchell et al. 2013; Trifonov et al. 2014). Typical masses in our sample are between $\sim 1\text{--}3 M_\odot$ and we reached RV precisions of $\sim 5\text{--}8 \text{ m s}^{-1}$. Among other results, we have found the first planet around a giant star (Frink et al. 2002) and showed that red giants with masses greater than $\sim 2.7 M_\odot$ host very few giant planets with an occurrence rate lower than 1.6% (Reffert et al. 2015).

The original selection criteria aimed at observing 86 bright K-giant stars ($V \leq 6$ mag) that were not variable or part of multiple stellar systems. Later in the survey, 93 new stars were added to the sample by imposing less stringent constraints regarding the photometric stability. Finally, in 2004, we added 194 G and K giants with bluer colors ($0.8 \leq B - V \leq 1.2$) with the aim of reducing the intrinsic RV jitter (e.g., Frink et al. 2001; Hekker et al. 2006). The inclusion of these stars allowed us to probe higher masses to test whether more massive stars host more massive planetary companions. More details on the selection criteria and on the giant star sample can be found in Frink et al. (2001) and Reffert et al. (2015).

The RV observations of HD 59686 A were carried out using the Hamilton Échelle Spectrograph (Vogt 1987) fed by the 0.6 m Coudé Auxiliary Telescope (CAT) of the Lick Observatory (Cali-

foria, USA). The Hamilton spectrograph covers the wavelength range 3755–9590 Å and has a resolution of $R \sim 60\,000$. The data were acquired and reduced using the iodine cell approach as described by [Butler et al. \(1996\)](#). We currently have 11–12 years of data for our original set of K-giant stars, of which HD 59686 A is a member. In total, we have 88 RV measurements for HD 59686 A throughout this period of time. The Lick RVs along with their formal uncertainties are listed in Table C.1 of Appendix C. Typical exposure times were 20 min, and the signal-to-noise ratios for these observations are typically about 120–150. The resulting RV measurements have a median precision of $\sim 5.6 \text{ m s}^{-1}$. This value is below the RV jitter of $16.4 \pm 2.9 \text{ m s}^{-1}$ expected for HD 59686 A based on scaling relations (see [Chaplin et al. 2009](#); [Kjeldsen & Bedding 2011](#)). Additionally, using our K-giant sample, we have obtained an empirical relation for the expected RV jitter as a function of color (see [Frink et al. 2001](#); [Trifonov et al. 2014](#)) given by

$$\log(\text{RV jitter [m/s]}) = (1.3 \pm 0.1)(B - V) + (-0.04 \pm 0.1), \quad (4.1)$$

where $(B - V)$ is the color index. Using this relation, we expect an intrinsic RV jitter of $26.5 \pm 9.2 \text{ m s}^{-1}$ for HD 59686 A. This value is consistent at the 1.1σ level with the result derived from scaling relations.

4.3 Results

4.3.1 Stellar properties

The stellar properties of the giant star HD 59686 A are given in Table 4.1. HD 59686 A is a slightly metal-rich star with $[\text{Fe}/\text{H}] = 0.15 \pm 0.1$ dex ([Hekker & Meléndez 2007](#)). To derive the stellar mass, we interpolated between the evolutionary tracks ([Girardi et al. 2000](#)), stellar isochrones, and metallicities using a trilinear interpolation scheme. This approach commonly allows two possible solutions depending on the evolutionary status of the star, namely red giant branch or horizontal branch (HB). By taking the evolutionary timescale, that is, the speed with which the star moves through that portion of the evolutionary track, as well as the initial mass function into account, probabilities were assigned to each solution. The derived mass of HD 59686 A is $M_{\star} = 1.9 \pm 0.2 M_{\odot}$ and the star was found to have a 89% probability of being on the HB. If it were instead on the RGB, then it would have a mass of $2.0 \pm 0.2 M_{\odot}$, thus the mass is not affected within the uncertainties. More details on the method, including the stellar parameters of all K-giant stars in our Doppler survey, can be found in [Reffert et al. \(2015\)](#).

The angular diameter of HD 59686 A was first calculated by [Merand et al. \(2004\)](#), using absolute spectro-photometric calibration from IRAS and 2MASS observations. They derived a diameter

Table 4.1: Stellar parameters of HD 59686 A.

Parameter	Value
Apparent magnitude m_v (mag) ¹	5.45
Absolute magnitude M_v (mag)	0.52 ± 0.06
Near-infrared magnitude K (mag) ²	2.92 ± 0.30
Color index $B - V$ (mag) ¹	1.126 ± 0.006
Effective temperature T_{eff} (K) ³	4658 ± 24
Surface gravity $\log g$ (cm s ⁻²) ³	2.49 ± 0.05
Metallicity [Fe/H] (dex) ⁴	0.15 ± 0.1
Stellar mass M_{\star} (M_{\odot}) ³	1.9 ± 0.2
Stellar radius R_{\star} (R_{\odot}) ³	13.2 ± 0.3
Parallax (mas) ¹	10.33 ± 0.28
Distance (pc)	$96.8 \pm \begin{smallmatrix} 2.7 \\ 2.6 \end{smallmatrix}$
Age (Gyr) ³	1.73 ± 0.47
Spectral type	K2 III

¹ Data from Hipparcos: [van Leeuwen \(2007\)](#)

² Data from 2MASS: [Skrutskie et al. \(2006\)](#)

³ [Reffert et al. \(2015\)](#)

⁴ [Hekker & Meléndez \(2007\)](#)

of 1.29 ± 0.02 mas, which at the Hipparcos distance of $96.8^{+2.7}_{-2.6}$ pc gives a value for the radius of $13.4 \pm 0.4 R_{\odot}$. Later, [Baines et al. \(2008a\)](#) used the Center for High Angular Resolution Astronomy (CHARA) interferometric array ([ten Brummelaar et al. 2005](#)) to measure an angular diameter of 1.106 ± 0.011 mas, deriving a radius of $11.62 \pm 0.34 R_{\odot}$. Our estimate of the stellar radius for HD 59686 A of $R_{\star} = 13.2 \pm 0.3 R_{\odot}$ agrees well with the value derived by [Merand et al. \(2004\)](#) and is slightly higher than the one obtained by [Baines et al. \(2008a\)](#).

4.3.2 Keplerian orbits

We fitted Keplerian orbits to the RV data of HD 59686 A. The uncertainties were derived through bootstrapping (using 5 000 bootstrap replicates) by drawing synthetic samples from the original RV dataset with data replacement (see [Press et al. 1992](#)). We fitted for two companions in the system, to which we refer as HD 59686 Ab and HD 59686 B.

In total, the Keplerian fit for HD 59686 Ab and HD 59686 B has 11 free parameters: the orbital period P , argument of periastron ω , RV semi-amplitude K , mean anomaly M_0 , and eccentricity

Table 4.2: Orbital parameters of the HD 59686 system.

Parameter	HD 59686 Ab	HD 59686 B
P (days)	$299.36^{+0.26}_{-0.31}$	11680^{+234}_{-173}
M_0 (deg) ¹	301^{+26}_{-85}	259^{+3}_{-1}
e	$0.05^{+0.03}_{-0.02}$	$0.729^{+0.004}_{-0.003}$
ω (deg)	121^{+28}_{-24}	$149.4^{+0.2}_{-0.2}$
K (m s ⁻¹)	$136.9^{+3.8}_{-4.6}$	4014^{+10}_{-8}
$m \sin i$ (M _{Jup})	$6.92^{+0.18}_{-0.24}$	$554.9^{+1.2}_{-0.9}$
a (au)	$1.0860^{+0.0006}_{-0.0007}$	$13.56^{+0.18}_{-0.14}$

¹ This parameter is the value of the mean anomaly at the first observational epoch $t_0 = 2451482.024$ JD.

e for each of the companions, and an arbitrary zero-point offset. The RVs of HD 59686 A are shown in Fig. 4.1 along with the best Keplerian fit to the data. We also plot the individual signals of the planet HD 59686 Ab and the stellar object HD 59686 B. Error bars are included in all the plots.

The best-fit orbital parameters for the planetary and stellar companions are given in Table 4.2. It is worth mentioning that K-giant stars exhibit intrinsic RV variability, known as stellar jitter. Therefore we decided to add in quadrature a jitter of 19.83 m s^{-1} , coming from the rms of the residuals around the fit, to our formal RV errors, which scaled down the χ^2_{red} to a value of 1 (without jitter, $\chi^2_{\text{red}} = 11.7$). The rms of the residual RVs, after subtracting the best Keplerian fit that includes the jitter, is 19.49 m s^{-1} . This result is consistent with the intrinsic scatter expected from K-giant stars (Eq. 4.1, see also [Hekker et al. 2008](#)) and is within 1.1σ from the value derived using scaling relations.

Figure 4.2 shows a generalized Lomb-Scargle (GLS) periodogram ([Zechmeister & Kürster 2009](#)) of HD 59686 A RVs. The top panel shows the results for the RV data, while the middle and bottom panels show the periodogram for the residuals after subtracting the stellar and stellar+planetary signals, respectively. The false-alarm probabilities (FAPs) were calculated by replacing the original RVs with randomly scrambled data through bootstrapping. We computed the GLS periodogram 1 000 times for this new dataset and calculated how often a certain power level is exceeded just by chance. The estimated FAPs of 0.1%, 1%, and 5% are shown in the plot as the horizontal dotted, dashed, and dash-dotted blue lines, respectively.

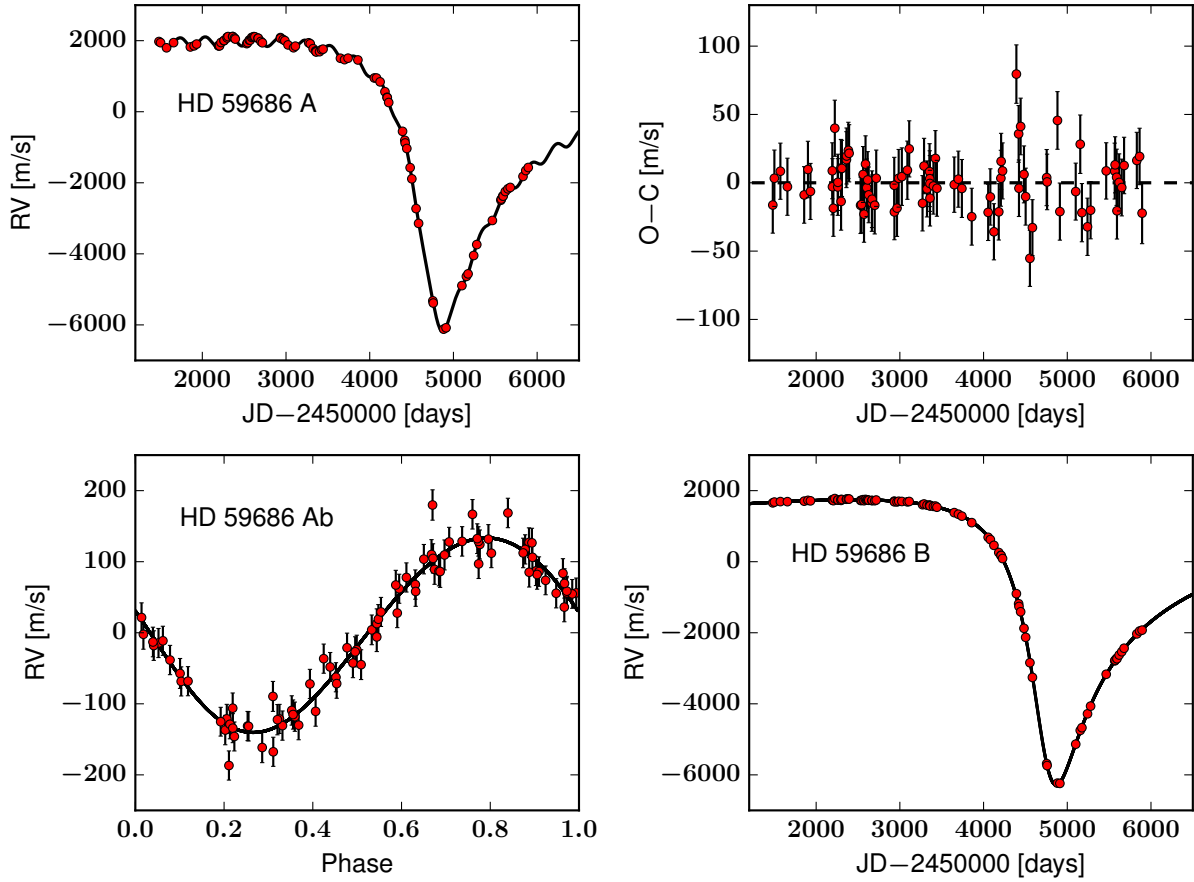


Figure 4.1: Radial velocity measurements of the HD 59686 system. Note that a jitter of 19.83 m s^{-1} was added in quadrature to the formal RV uncertainties, and this is reflected in the plot. *Upper left:* Lick RVs together with the best Keplerian fit to the data. *Upper right:* RV residuals from the fit. *Lower left:* Phased RV variations and Keplerian fit for the $\sim 7 M_{\text{Jup}}$ planet HD 59686 Ab after subtracting the signal of the stellar companion. *Lower right:* RV data and Keplerian fit for the $\sim 0.5 M_{\odot}$ stellar object HD 59686 B after subtracting the planetary signal.

The top panel shows one significant peak in the GLS periodogram at ~ 5000 days, which is approximately the length of time over which HD 59686 A has been observed. This wide peak represents the long period of HD 59686 B ($P = 11680_{-173}^{+234}$ days), for which one complete orbit has not been observed yet. However, we are able to set tight constraints on the binary period as the eccentricity of the orbit is very high. The second strongest peak is at ~ 340 days, very roughly matching the best Keplerian fit for the planetary companion ($P = 299.36_{-0.31}^{+0.26}$ days). The third largest peak at ~ 400 days is an alias period that disappears when the signal of the stellar companion is removed from the data. This is shown in the middle panel where the strength of the signal due to the planet increases significantly, and another alias period also appears at around

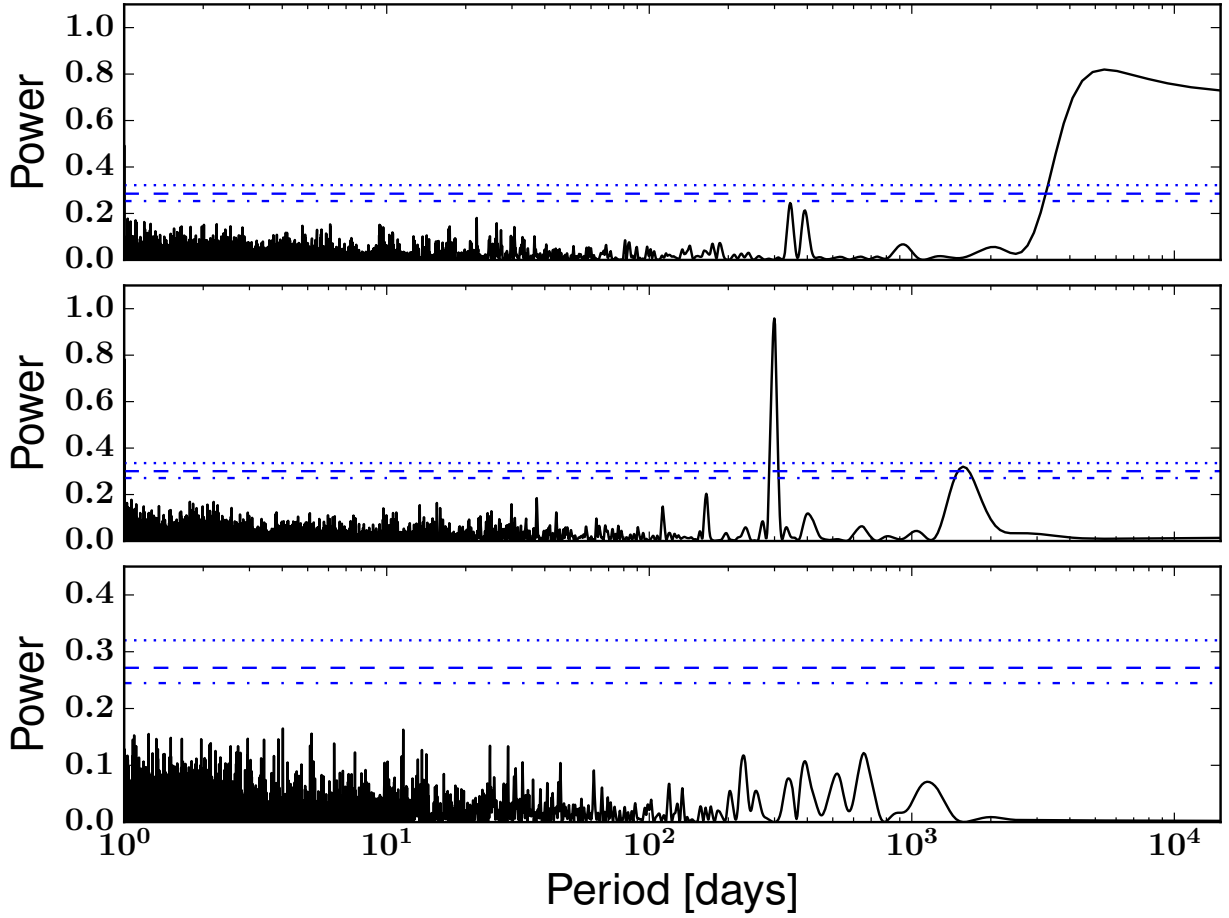


Figure 4.2: *Top:* GLS periodogram of the RV data of HD 59686 A. The significant peaks at ~ 5000 and ~ 340 days represent the orbits of the stellar and planetary companions, respectively. The 5000-day period is the time frame of our observations, therefore it is much shorter than the actual stellar period. The dotted, dashed, and dash-dotted lines show FAPs of 0.1%, 1%, and 5%, respectively. *Middle:* Periodogram of the residual RVs after the signal due to the stellar companion is removed from the data. Now the peak due to the planetary companion becomes much stronger and the alias period at ~ 400 days disappears. Additionally, another alias period appears at ~ 1700 days. *Bottom:* Periodogram of the residual RVs after subtracting the orbital fit (stellar+planetary companions); it shows no significant peaks.

1700 days. After the planetary companion is subtracted, this peak disappears and no significant periodicities are observed in the signal of the RV residuals.

By adopting a stellar mass of $M_{\star} = 1.9 \pm 0.2 M_{\odot}$, we derived a minimum mass of $6.92^{+0.18}_{-0.24} M_{\text{Jup}}$ for HD 59686 Ab and a value of $554.9^{+1.2}_{-0.9} M_{\text{Jup}}$ for HD 59686 B. The mass for HD 59686 B is equivalent to $\sim 0.53 M_{\odot}$, which immediately places this companion in the stellar regime; it cannot be a massive planet or a brown dwarf. The planet orbits the giant star at a distance of $a_p = 1.0860^{+0.0006}_{-0.0007}$ au, while the semi-major axis of the stellar companion is $a_B = 13.56^{+0.18}_{-0.14}$ au.

Furthermore, the orbit of HD 59686 B is very eccentric ($e = 0.729^{+0.004}_{-0.003}$), which may have played an important role in the formation and/or evolution of the inner planet, as we discuss in Sect. 6.

4.4 Validating the planetary signal

4.4.1 Rotational modulation

Stellar surface phenomena such as star spots, plages, or convection modulated by stellar rotation may generate low-amplitude RV variations that can mimic planetary signatures. To investigate such false-positive scenarios, we determined the stellar rotation of HD 59686 A. [Hekker & Meléndez \(2007\)](#) estimated the projected rotational velocity of HD 59686 A to be $v \sin i = 4.28 \pm 1.15 \text{ km s}^{-1}$. Using our estimate of the stellar radius ($R_{\star} = 13.2 \pm 0.3 R_{\odot}$), we determine an upper limit for the rotation period of HD 59686 A of $P_{rot}(\sin i_{\star})^{-1} = 156.03 \pm 39.35$ days. This means that any low-amplitude RV variations generated by surface phenomena that are modulated by stellar rotation cannot have periods longer than ~ 195 days. Therefore, it is unlikely that the periodic signal ($P = 299.36^{+0.26}_{-0.31}$ days) is generated by stellar rotation.

[Massarotti et al. \(2008\)](#) estimated a slightly lower value for the projected rotational velocity of 3.8 km s^{-1} for HD 59686 A, which implies $P_{rot}(\sin i_{\star})^{-1} = 175.74 \pm 46.42$ days (assuming 1 km s^{-1} error in $v \sin i$), consistent with the results of [Hekker & Meléndez \(2007\)](#) and with the above statement. On the other hand, [Carlberg et al. \(2012\)](#) calculated a value of $v \sin i = 0.93 \pm 0.41 \text{ km s}^{-1}$ for the K-giant, implying $P_{rot}(\sin i_{\star})^{-1} = 718 \pm 495$ days. However, this result has large uncertainties and, as discussed by the authors, their estimates of $v \sin i$ show significant systematic differences when compared to values derived in the literature. Specifically, their estimates of $v \sin i$ are systematically lower than those reported in other studies (see Fig. 6 of [Carlberg et al. 2012](#)), which can be accounted for by an overestimation of the macroturbulence velocity, particularly in the slow-rotation regime.

Regardless of the above considerations, to test the hypothesis that the $299.36^{+0.26}_{-0.31}$ day period may be caused by stellar activity, like long-period pulsations for example, we checked infrared RVs, all available photometry, and spectral activity indicators as described in the following sections.

4.4.2 Infrared radial velocities

It is recognized that intrinsic stellar activity, such as cool spots, can create RV variations in giant stars that can mimic the presence of companions (e.g., [Hatzes & Cochran 2000](#); [Hatzes et](#)

al. 2004). This poses an additional challenge for validating the interpretation of a periodic RV change as a bona fide planet, when compared to inactive MS stars. Moreover, some giant stars are known to be pulsating stars, which show several modes of pulsation with varying amplitudes and frequencies (De Ridder et al. 2009; Huber et al. 2010; Christensen-Dalsgaard et al. 2012; Stello et al. 2013). In the case of radial pulsations, the stellar surface moves away and toward the observer, which induces periodic RV variations.

The pulsation frequencies of a star are closely related to its density and temperature, as these control the speed at which sound waves can propagate. Using the scaling relation of Kjeldsen & Bedding (1995), we calculated the period of the pulsation with maximum amplitude using our derived values of the radius, mass, and effective temperature, which yielded a value of 0.31 days for HD 59686 A. Although this calculation is not ideal for giant stars, it should give a reasonable estimate of the pulsation period with the largest amplitude. This value is orders of magnitudes below the RV oscillations seen in our data.

It is possible, though unlikely, that some pulsation exists in HD 59686 A with a much lower frequency, but large enough amplitude to be detectable in our data, which could be the source of the RV oscillations we observe. Non-radial pulsations are much more complicated to model, and they can display an arbitrary number of amplitudes and periods for different modes. However, it is not expected that the RV amplitude of the pulsations in the visible waveband match the amplitude in the infrared, since the photometric variations of pulsating stars are wavelength dependent (e.g., Percy et al. 2001, 2008). On the other hand, if the RV oscillations are due to a companion, then the infrared and visible RV variations should be consistent with each other.

In 2012 and 2013, Trifonov et al. (2015) obtained infrared RVs of HD 59686 A using the Cryogenic high-resolution InfraRed Echelle Spectrograph (CRIRES; Käufel et al. 2004) at the Very Large Telescope (VLT), in Chile. Their CRIRES spectra have a resolution of $R \sim 100\,000$ and cover the wavelength range 1.57–1.61 μm . Details of the CRIRES observations and the reduction process, including the measured RVs for HD 59686 A, can be found in Trifonov et al. (2015).

We obtained the RV offset between the CRIRES and Lick velocities for HD 59686 A by fitting the CRIRES and Lick RVs keeping all the orbital parameters fixed. Figure 4.3 shows the CRIRES RV data (with the RV offset applied) together with the best Keplerian fit to the Lick data. The infrared RVs match the Keplerian model obtained from the optical data. This should in general not be the case if the RV variations were due to large amplitude stellar pulsations. Moreover, the scatter around the fit of $\sim 59 \text{ m s}^{-1}$ is consistent with the relatively large uncertainties⁴ of the CRIRES RVs that are on the order of $\sim 45 \text{ m s}^{-1}$.

⁴To be consistent with the optical fit, a jitter of 19.83 m s^{-1} was added to the formal CRIRES RV uncertainties.

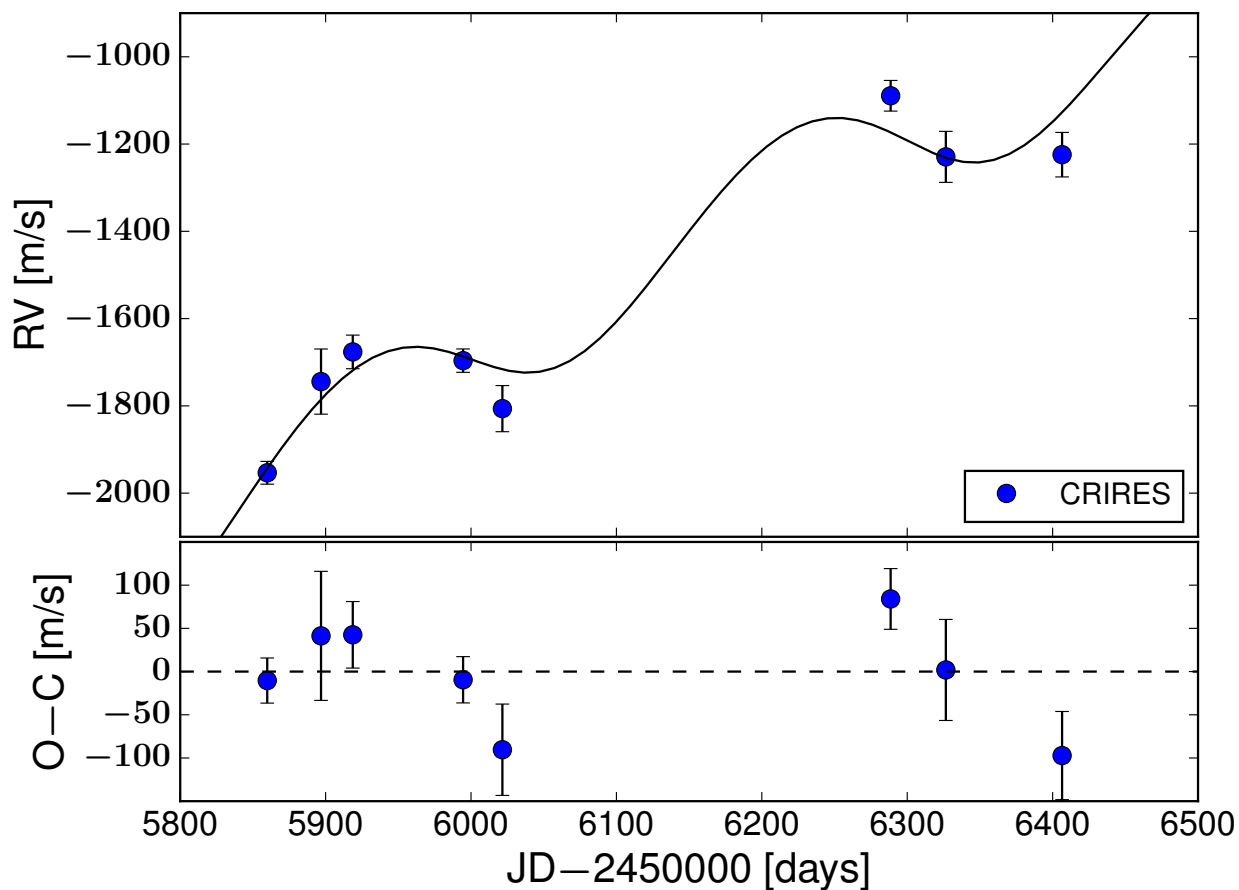


Figure 4.3: *Upper panel:* CRILES infrared RV measurements of HD 59686 A. The black solid line shows the best Keplerian fit obtained from the Lick data alone. *Bottom panel:* Residuals of the CRILES RVs from the optical fit. The value of the rms is $\sim 59 \text{ m s}^{-1}$, which is consistent with the large infrared RV errors. The mean error of the CRILES data, with a jitter of 19.83 m s^{-1} added in quadrature, is $\sim 45 \text{ m s}^{-1}$.

An additional test can be made by fitting only the CRIRES data to derive the RV semi-amplitude, K_{IR} . Following [Trifonov et al. \(2015\)](#), we first subtracted the signal of the stellar companion from the CRIRES data. As the presence of HD 59686 B is clearly detected in the system, it is fair to assume that the RV signal due to this star is consistent in the optical and infrared data sets. Then, we performed a Keplerian fit to the CRIRES RVs keeping all parameters fixed (the parameters obtained from the Lick RVs) with the exception of the RV semi-amplitude and RV zero point. We derived a value of $K_{IR} = 206.0 \pm 29.1 \text{ m s}^{-1}$. The RV semi-amplitude of $K_{opt} = 136.9^{+3.8}_{-4.6} \text{ m s}^{-1}$ from the optical RVs is within 2.25σ from the IR value. If we calculate $\kappa = K_{IR}/K_{opt}$, as in [Trifonov et al. \(2015\)](#), then we obtain a value of $\kappa = 1.50 \pm 0.22$, but we note that the calculated error might be underestimated as the error on the fitting of the stellar component is not taken into account. This result shows that the near-IR signal is not flat or of a smaller amplitude than the optical one, which we would expect for a spot or pulsations; the amplitude of pulsations decreases with increasing wavelength in pulsating giant stars ([Huber et al. 2003](#); [Percy et al. 2008](#)). We also have only a handful of moderately precise IR RVs and in addition, a stellar jitter of about 20 m s^{-1} for HD 59686 A, but we observe that the optical and near-IR phases are consistent, which is not necessarily expected for pulsations. This means that most likely the signal is real and caused by the gravitational perturbation of a companion in the system.

4.4.3 Photometry

The ASAS-3 Photometric V-band Catalog ([Pojmański 1997, 2001](#)) contains 290 best-quality measurements (grade A) of HD 59686 A collected over seven years between December 13, 2002 (HJD = 2452621.84) and November 24, 2009 (HJD = 2455159.78). Unfortunately, HD 59686 A is a very bright target ($V=5.45$) and exceeds the ASAS-3 V-band saturation limit with the used exposure times (180 seconds). The high dispersion of the ASAS-3 V-band photometric measurements of HD 59686 A (peak-to-peak amplitude of 0.784 mag, mean value $\bar{V} = 5.74 \pm 0.19 \text{ mag}$) and the mean value of the errors (38.5 mmag) ensure that HD 59686 A saturates the ASAS-3 detector.

The only unsaturated photometry for HD 59686 A was acquired by the Hipparcos mission ([ESA 1997](#)) between March 16, 1990 and March 10, 1993 (2447966.9 – 2449057.2 JD), more than six years before first RV observations of HD 59686 A. The Hipparcos data set consists of 96 measurements with 5.6 mmag mean error, 5.6 mag mean value, and a standard deviation of 5.5 mmag, similar to the mean error of the measurements. As shown in the bottom panel of Fig. 4.4, no significant periodic signal was found in the photometry of these data. Additionally, we can use the Hipparcos data to investigate whether a hypothetical spot might have produced a noticeable photometric variation. We derived the spot filling factor that would be required to generate the

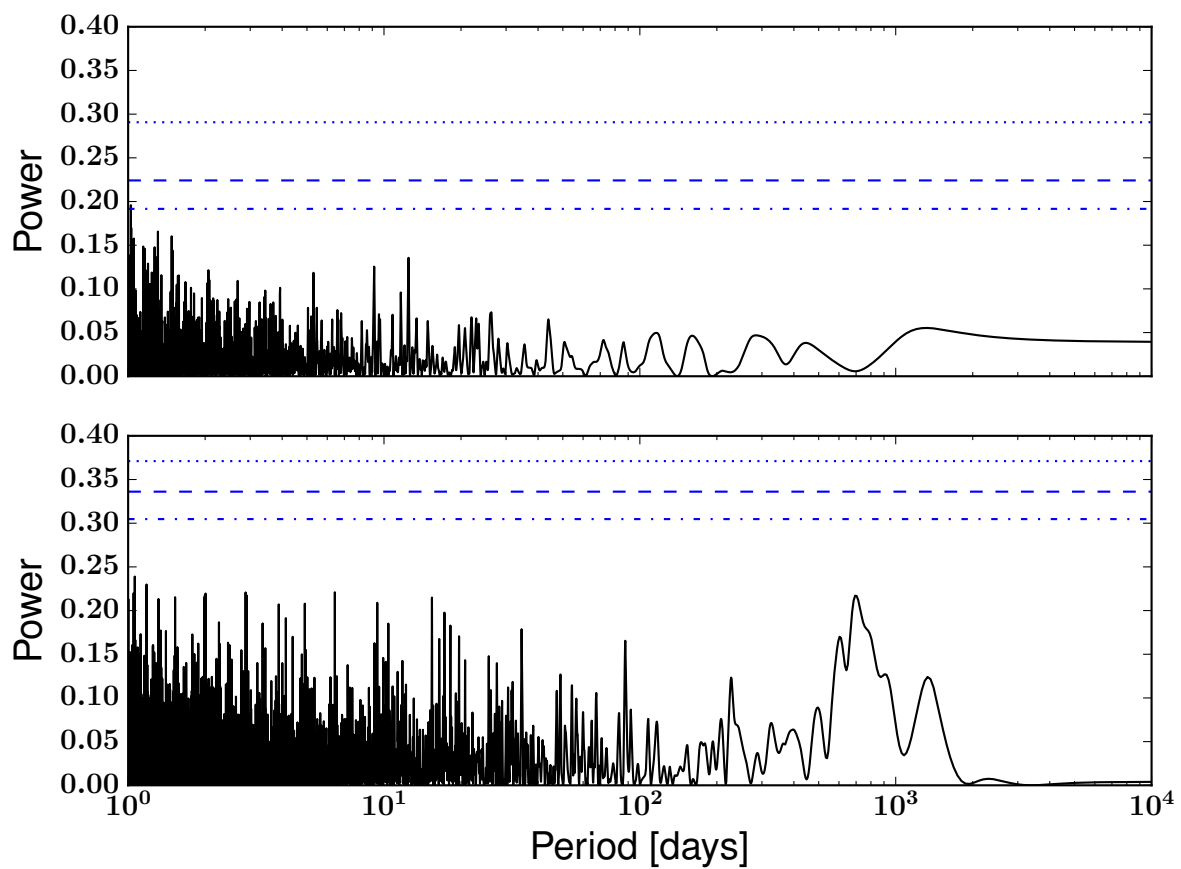


Figure 4.4: *Upper panel:* GLS periodogram of the $H\alpha$ index measurements of HD 59686 A. *Bottom panel:* GLS periodogram of the Hipparcos V-band photometry of HD 59686 A. The dotted, dashed, and dash-dotted lines in both panels show FAPs of 0.1%, 1%, and 5%, respectively, obtained by bootstrapping. No significant periodicities are found in the data.

observed RV amplitude of $\sim 137 \text{ m s}^{-1}$ using the relation found by [Hatzes \(2002\)](#) for cool spots on sun-like stars. We obtained a spot filling factor of $f = 0.1$, meaning that 10% of the stellar surface must have been covered by spots to produce the large RV variation seen in the data. Using this value for the filling factor, the expected photometric variability is $\Delta m = 0.078 \text{ mag}$ for a temperature difference of $\Delta T = 1200 \text{ K}$ between the spot and the stellar photosphere. This level of variation is one order of magnitude above the observed dispersion seen in the Hipparcos data. The same is true for a wide range of temperature differences of typical star spots ranging from $\Delta T = 200 - 1200 \text{ K}$ (e.g., [Biazzo et al. 2006](#); [O’Neal 2006](#)).

Nevertheless, hypothetical surface structure phenomena might mimic the presence of an exoplanet. For example, [Hatzes & Cochran \(2000\)](#) investigated the possible existence of a macroturbulent spot to explain the RV variation of Polaris. Given the right conditions, this dark spot might cause a large RV oscillation without a significant photometric variation. However, the values of, for example, the magnetic field and the difference between the velocity of the macroturbulent spot and the surrounding surface must be exceptionally well fine-tuned to produce an RV variation of hundreds of m/s. In addition, if a macroturbulent spot causes the RV changes in HD 59686 A, then it must have been long-lived and maintained a constant and consistent effect during at least 12 years. The same is true for long-lived long-period non-radial pulsations, which is not necessarily expected. Thus, although we cannot completely discard this scenario, a giant planet orbiting the star HD 59686 A appears as the most plausible interpretation of our data.

4.4.4 Spectral activity indicators

Since the RV measurements of HD 59686 A were acquired using the iodine-cell method, it is difficult to perform precise bisector measurements of spectral lines as the stellar spectra are affected by I_2 lines. Instead of this, we performed an analysis of the $H\alpha$ line, which is located in the central region of one of the Hamilton spectrograph orders and is known to be a good indicator of stellar activity. We measured the $H\alpha$ index using the approach presented by [Kürster et al. \(2003\)](#). However, we broadened the width of the window centered on $H\alpha$, from $\pm 15 \text{ km s}^{-1}$ used by [Kürster et al. \(2003\)](#) for Barnard’s star to $\pm 45.68 \text{ km s}^{-1}$ ($\pm 1 \text{ \AA}$) recently used by [Hatzes et al. \(2015\)](#) for Aldebaran. As reference windows we used spectral regions that extend from -250 and -650 km s^{-1} and from 250 and 650 km s^{-1} . The upper panel of Fig. 4.4 shows the GLS periodogram of the $H\alpha$ index measurements. As for the Hipparcos photometry, no significant signal exist in the $H\alpha$ index of HD 59686 A. Figure 4.5 presents the $H\alpha$ index against the time of each RV observation of HD 59686 A and as a function of the RV variation induced by the planet HD 59686 Ab (without the contribution of the stellar companion). The plot shows no correlation between these RVs and the $H\alpha$ index. Moreover, we measured a Pearson correlation coefficient of $r = 0.06$ with a p -value=0.58. This analysis corroborates that the $299.36^{+0.26}_{-0.31}$ day period in

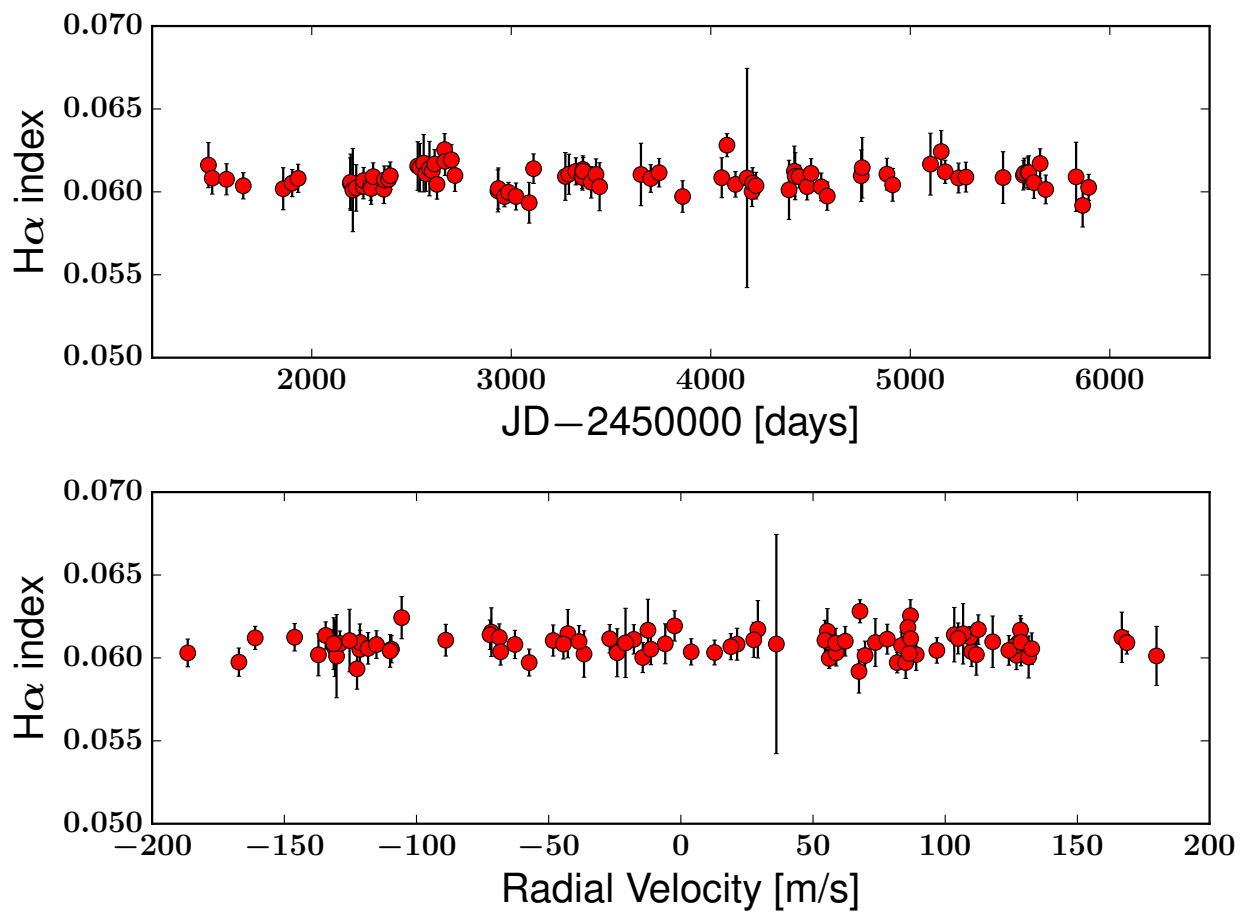


Figure 4.5: *Upper panel:* H α index measurements at the time of each RV observation of HD 59686 A. *Bottom panel:* H α index measurements as a function of the RVs due to the planetary companion HD 59686 Ab, that is, with the stellar component subtracted from the data. No significant correlation is seen in the data, which corroborates that a giant planet is part of the system.

the RV curve of HD 59686 A is most likely generated by the gravitational pull of a planetary companion.

It is worth to note, however, that HD 59686 A shows some similarities to carbon-enhanced metal-poor (CEMP) stars (see [Beers & Christlieb 2005](#); [Masseron et al. 2010](#); [Placco et al. 2014](#)) in the sense that these are evolved giants, they reside in binary systems, and the secondary is very likely a white dwarf (provided that HD 59686 B is confirmed to be a white dwarf). Recently, [Jorissen et al. \(2016a\)](#) has identified low-amplitude RV variations superimposed on the binary trend in 3 CEMP stars in a sample of 13. They show periods of about one year and RV semi-amplitudes of hundreds of m/s. [Jorissen et al. \(2016b\)](#) discussed the origin of the RV variations of one system in particular, HE 0017+005, and suggested that this may be due to pulsations in the envelope of the giant star. Unfortunately, the spectral types of the stars from Jorissen et al. are not well established. The authors assumed that all the stars have masses of $\sim 0.9 M_{\odot}$, and it is likely that these very metal-poor stars are in a different stage of the stellar evolution than HD 59686 A, which we expect to be on the HB with a 89% probability (see [Reffert et al. 2015](#)). In particular, the $\log g$ values of the RV-variable CEMP stars seems to be much lower than that of HD 59686 A (see [Jorissen et al. 2016b](#)), which makes pulsations much more plausible for those stars. Even if pulsations should be confirmed as the correct interpretation of the RV variations observed in CEMP stars, this will probably not be the case for HD 59686 A because all the available observational evidence at hand (e.g., $H\alpha$ index, photometry, infrared RVs) supports the planetary hypothesis, unless some exotic not-yet-observed surface macroturbulent structure or long-lived long-period non-radial pulsation was taking place in HD 59686 A for more than a decade, which we consider unlikely. Nevertheless, there is much that we do not know about long-period stellar oscillations in giant stars, and we cannot fully exclude such phenomena.

4.4.5 Discarding a hierarchical triple star system

Another possibility that can mimic planets in binary systems are hierarchical triple systems in which the observed RV signals are caused by another star orbiting the binary companion instead of a planet orbiting the primary star. For instance, [Schneider & Cabrera \(2006\)](#) and [Morais & Correia \(2008\)](#) studied the effects on the RV measurements of a star orbited by a pair in a close circular orbit in a triple star system. They concluded that the effect of the binary is approximately weaker than ~ 1 m/s in the RV semi-amplitude and can only mimic a low-mass Earth- or Saturn-like planet. Later, [Morais & Correia \(2011\)](#) extended their work to triple star systems on eccentric orbits, showing that the binary effect is stronger than in the circular case. However, the magnitude of the RV semi-amplitude is still about a few meters per second and cannot account for the large variation that we see in the RV data of HD 59686 A ($K \sim 137 \text{ m s}^{-1}$). Furthermore, we can estimate the effect that a binary star system with a total mass of $\sim 0.5 M_{\odot}$ with a period of ~ 300

days can generate in the RV semi-amplitude (using Eq. 37 of [Morais & Correia 2011](#)). For reasonable values of the amplitudes of the frequency terms induced by a hypothetical third star in the system, we obtained a value of the RV semi-amplitude mimicking a planet ranging from $\sim 1\text{--}5\text{ m s}^{-1}$, that is, more than an order of magnitude smaller than what we observe in our data. We therefore conclude that a hidden star orbiting the stellar object HD 59686 B is not the cause of the observed RV variations in the system.

4.5 High-contrast images

4.5.1 Previous search for stellar companions in HD 59686 A

HD 59686 A has been examined before for stellar companions. [Roberts et al. \(2011\)](#) found a visual component separated by $5.61''$. Assuming a face-on circular orbit, this corresponds to a minimum separation of $\sim 519\text{ au}$. If this component were a physical companion, then the separation would lead to an orbital period far too large to be visible in our data. [Baines et al. \(2008b\)](#) have also observed HD 59686 A using the CHARA interferometer. They performed fits to the diameter of several stars and found that single stars were consistently fit with low values of χ^2 , while the presence of a stellar companion created a systematic behavior in the residuals, resulting in a high χ^2 value. They saw no such systematic behavior in the fit of HD 59686 A and therefore ruled out a MS companion more massive than G5 V within a field of view of 230 mas ($\sim 23\text{ au}$).

[Baines et al. \(2008b\)](#) also searched for small-separation binaries by looking for separated fringe packets in the data. If a second star were present in the system with a separation of around $10\text{ to }100\text{ mas}$ ($\sim 1\text{--}10\text{ au}$), then two sets of fringe packets would be detected. However, no separated fringe packet was observed for HD 59686 A. This approach relies on the assumption that the angular separation of the two stars is not small and that the position angle is not perpendicular to the projected baseline angle. Most likely, the authors failed to detect HD 59686 B because this star is expected to be much fainter than the giant primary and was probably below the contrast sensitivity of CHARA.

With the aim of investigating the nature of the stellar object HD 59686 B, we acquired high-resolution images of this system as explained in the following sections.

4.5.2 Observations and data reduction

The high-contrast imaging observations of HD 59686 A were carried out on February 9, 2014 using the L/M-band InfraRed Camera (LMIRCam; [Skrutskie et al. 2010](#); [Leisenring et al. 2012](#)) mounted at the Large Binocular Telescope Interferometer (LBTI; [Hinz et al. 2012](#)) on Mt. Graham, Arizona. LMIRCam is a high-resolution camera designed to operate in the 3–5 μm wavelength range. The infrared detector is a 1024×1024 HgCdTe array, with a plate scale of 10.707 ± 0.012 mas/pix ([Maire et al. 2015](#)) and a field of view of $11\times 11''$.

The observations were taken using only the left side of the LBT in pupil-stabilized mode, which further allows the use of angular differential imaging (ADI; [Marois et al. 2006](#)). The core of the PSF was intentionally saturated to increase the signal of the binary companion. Unsaturated exposures with a neutral density filter were also taken for calibrating the photometry. The AO system was locked with 300 modes during the whole duration of our observations. We obtained 205 minutes of on-source integration and $\sim 100^\circ$ of field rotation. A total of 7413 images of HD 59686 A were taken in the L' -band filter ($\lambda_c=3.70$ μm , $\Delta\lambda=0.58$ μm).

To properly subtract the background emission and detector systematics, the star was dithered to two different positions on the detector separated by $4.5''$. Additionally, our reduction steps included dark current subtraction, flatfielding, bad pixel correction, bad image removal, image alignment, and trimming of the data. We were left with a 300×300 pixel datacube of 5487 reduced images. However, during large parts of the observing sequence, weather conditions were not optimal (seeing $>1.5''$), so that we decided to discard 20% of the images based on the measurement of the correlation of each one of the frames with respect to a high-quality reference frame of the sequence. In total, we obtained a datacube of 4389 images.

4.5.3 PSF subtraction

In addition to simple ADI processing, more sophisticated algorithms exist, such as the locally optimized combination of images (LOCI; [Lafrenière et al. 2007](#)) and principal component analysis (PCA; [Amara & Quanz 2012](#); [Soummer et al. 2012](#); [Brandt et al. 2013](#)). They can be used to subtract the light profile of a star to detect possible companions around it. We decided to follow a PCA approach, as it has been shown to produce better contrast performance for small inner working angles (e.g., [Meshkat et al. 2014](#)). The expected binary separation at the time of our observations is small, so that even with the PCA technique it is challenging to detect any signal at all, considering that we do not know the orbital inclination and orientation of the orbit.

To analyze our stack of images, we used the open-source Python package VIP⁵ (Gomez Gonzalez et al. 2016a), which provides a collection of routines for high-contrast imaging processing, including PCA and slight variations of it, such as annular and subannular PCA. The PCA algorithm models the star light as a linear combination of a set of orthogonal basis functions or principal components (PCs) and fits for the PC coefficients in each of the frames in the stack. This means that the parameter that must be set is the number of PCs used to model the PSF in each frame. We started by estimating the optimal number of PCs by inserting a star in each of the images at a small separation from the center of the primary star. We varied the magnitude difference of this fake companion with the central star from $\Delta m=8-11$ mag in steps of 0.5 mag and determined the number of PCs that maximizes the S/N in an aperture of 1 FWHM centered on the coordinates of the fake star after running the PCA. We searched in a grid ranging from 1-200 PCs and found that the highest S/N values were obtained for 10, 38, 77, and 81 PCs. The central saturated core of the PSF (eight-pixel radius) was masked and not considered in the fitting. We show in Fig. 4.6, panels *a* to *d*, the results after running the PCA in the stack of images of HD 59686 A using the previously derived numbers of PCs. No significant signal was found in the residual images.

Additionally, we also performed a local PCA by fitting for the stellar PSF in quadrants of circular annuli of 3 FWHM width around the central star. In this case, the PCA is computed locally in each quadrant, and we applied a parallactic angle rejection of 1 FWHM to discard adjacent frames and avoid self-subtraction of the companion star. The number of PCs was decided automatically in each quadrant by minimizing the residuals after subtracting the PSF. The resulting residual image is shown in panel *e* of Fig. 4.6. As in the full-frame PCA, no significant companion is seen in the plot.

As an alternative to the standard PCA, we also used the new algorithm recently introduced by Gomez Gonzalez et al. (2016b) to subtract the stellar PSF of high-contrast images and enhance the signal of faint companions. The method is named by the authors local low-rank plus sparse plus Gaussian-noise decomposition (LLSG). The main idea of the algorithm is to use a robust PCA approach (see, e.g., Candès et al. 2009) to decompose the stellar image into three components; a low-rank, a sparse, and a Gaussian noise part. The low-rank carries most of the signal from the stellar PSF, the Gaussian noise captures the quasi-static features of the speckle noise, and the sparse component contains the signal of potential faint companions. The most important parameter to set in the LLSG algorithm is the rank, which is equivalent to set the number of PCs in the standard PCA. We chose a rank of 51 as the mean of the optimum number of PCs derived before. We note, however, that varying the rank number does not change the obtained results significantly. The residual image after the LLSG subtraction is shown in panel *f* of Fig. 4.6. Although the quality of the image seems to be much better than in previous images, we did not detect any signal from the binary star HD 59686 B.

⁵<https://github.com/vortex-exoplanet/VIP>

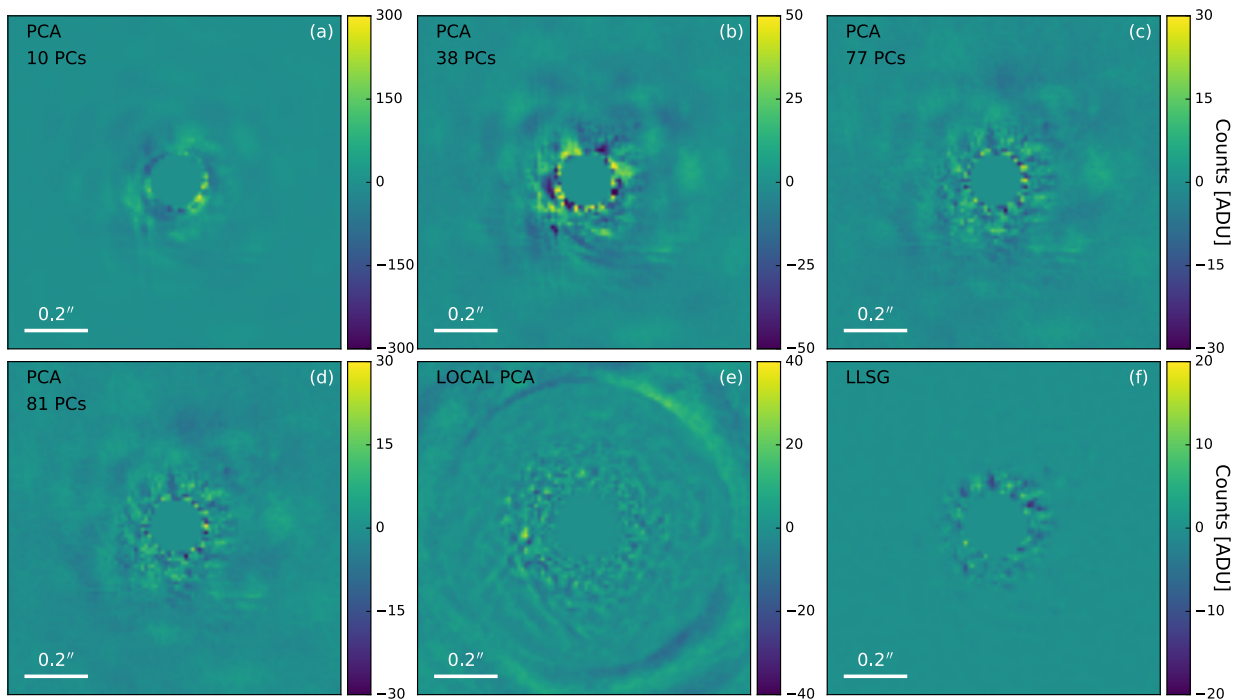


Figure 4.6: High-contrast L' -band LMIRCam images of HD 59686 A. Panels *a*, *b*, *c*, and *d* show the residual images after running the PCA with 10, 38, 77, and 81 principal components. Panel *e* shows the image obtained with a local, subannular PCA approach, and panel *f* presents the residual image after subtracting the stellar PSF using the new LLSG algorithm. No signal of the companion star HD 59686 B is detected in any of the panels.

The obtained results can be explained by (i) the poor weather during some part of the observations, (ii) the small expected angular separation of the companion, and (iii) the probability that the orbit orientation placed the star at a projected separation such that the companion is not visible from Earth at the time of observation.

4.5.4 Contrast curve calculation

Assuming that the orbital configuration is favorable at the observing time and that we are only limited by the contrast of the binary pair and the quality of our images, we can set constraints on the maximum brightness that the companion star could have without being detected in our images. To do that, we injected fake companions of various magnitudes at different distances from the central star. As a fake companion star we used the median-combined PSF of the unsaturated data set and scaled it to different contrast ratios based on the photometry of the unsaturated image of HD 59686 A and taking into account the different exposure times between the saturated and unsaturated frames. The fake stars were then inserted in each of the reduced stack of images, accounting for the change in parallactic angle during the rotation sequence. We then processed these images with the VIP package in the exact same way as before and calculated the $5\text{-}\sigma$ detection limit in terms of S/N at the position of each fake star. We adopted the S/N definition of Mawet et al. (2014) as we are working at distances very close to the center of the star, and the low-pixel statistics applies. We repeated this procedure at four different position angles for each radius and then took the average to minimize random speckle errors.

In Fig. 4.7 we show the 5σ contrast curve of the LBT images as a function of the angular separation from the central star. Our data reach contrasts between $\sim 5\text{--}10$ mag for separations between $\sim 0.16''\text{--}0.24''$ (15.5–23.2 au). We also show the maximum expected binary separation at the observing time of $a_{max} \sim 11.7$ au (black dashed line) and the PSF saturation radius of $r_s \sim 8.3$ au (black dash-dotted line). The expected separation of the binary pair comes from a detailed study of the dynamical stability of the HD 59686 system that constrains the orbital inclination to the range $i \sim 50^\circ\text{--}90^\circ$ (Trifonov et al. 2016, in prep.). For an inclination of 50° , we derived the value of 11.7 au, which translates into $\sim 0.12''$ of angular separation. Adopting higher values for the inclination results in lower values for the binary separation. Unfortunately, the large saturation radius of the LMIRCam images ($\sim 0.085''$) prevents us from deriving reliable values for the 5σ contrast in the region $\lesssim 0.15''$ ($\lesssim 14.5$ au), in which we expect HD 59686 B to reside. Nevertheless, we show in the plot (red solid lines) the expected contrasts for a star of 0.5 and $1 M_\odot$. A G-type star of $1 M_\odot$ or greater is excluded for separations $\gtrsim 17$ au. For lower masses and separations our sensitivity decreases significantly, and we cannot exclude the presence of a star with masses between $0.5\text{--}1 M_\odot$.

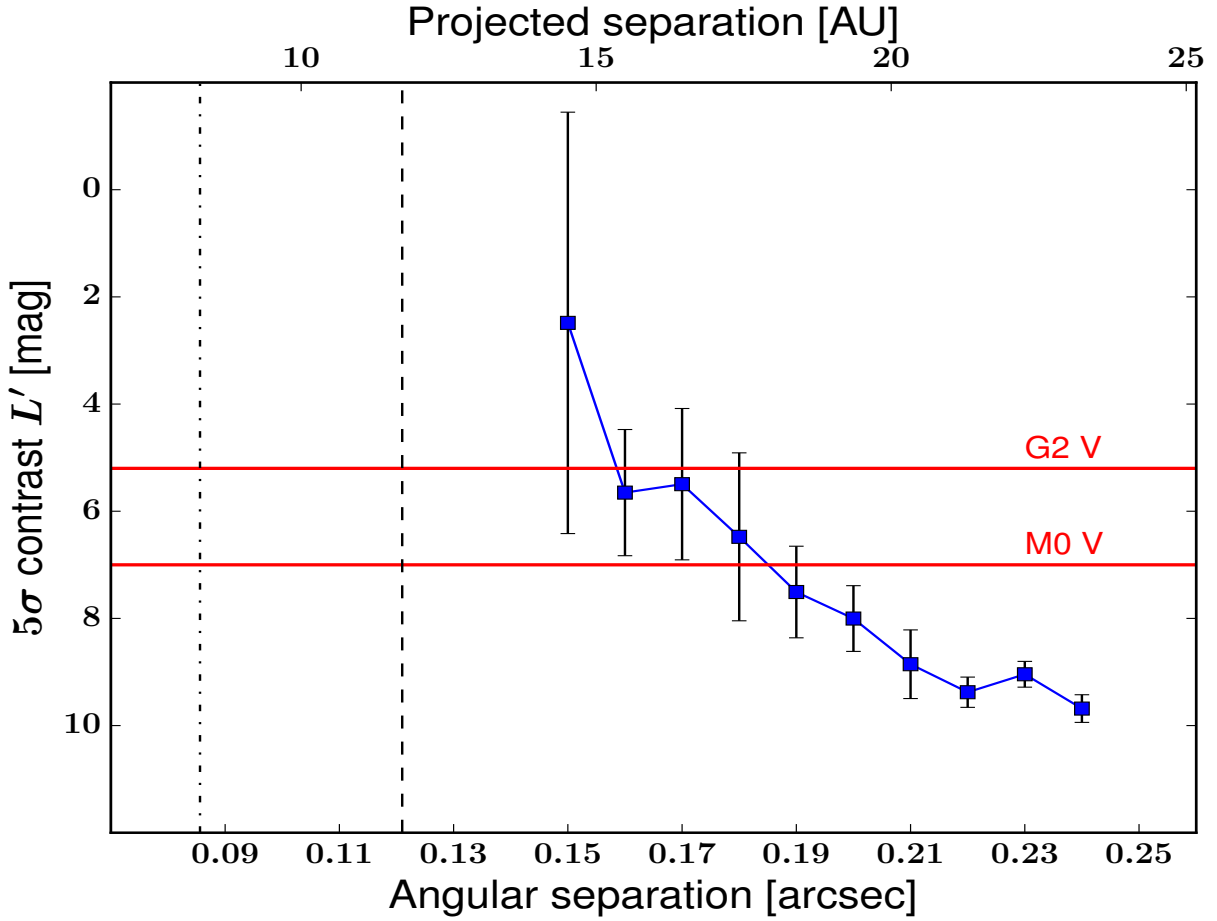


Figure 4.7: $5\text{-}\sigma$ detection limits in terms of the magnitude contrast in the L' -band as a function of the distance from the central star. The black dashed line represents the binary separation upper limit of ~ 11.7 au at the time of the observations. The dash-dotted line marks the saturation radius of $\sim 0.085''$. The red solid lines mark the expected contrasts for a G2 V star of $1 M_{\odot}$ and a M0 V star of $0.5 M_{\odot}$, from top to bottom.

To illustrate the configuration of the binary system, we show in Fig. 4.8 the sky-projected orbit of HD 59686 AB derived from the fitted orbital parameters. The red labels mark the position of each of the stars at certain times (in years). The green symbols highlight the respective locations of HD 59686 A and HD 59686 B in the binary orbit at the time of the LBT observations. The high eccentricity of the binary is clearly visible. Fortunately, both components are moving away from each other at the moment, so that it should become easier to detect HD 59686 B in the coming years. In about ~ 2025 , the system will be in apastron at a minimum separation of roughly $\sim 20\text{--}21$ au assuming an inclination of $i = 90^{\circ}$. For lower values of the inclination the binary separation increases. Future high-resolution observations of this system are highly encouraged to better constrain the nature of the stellar object HD 59686 B.

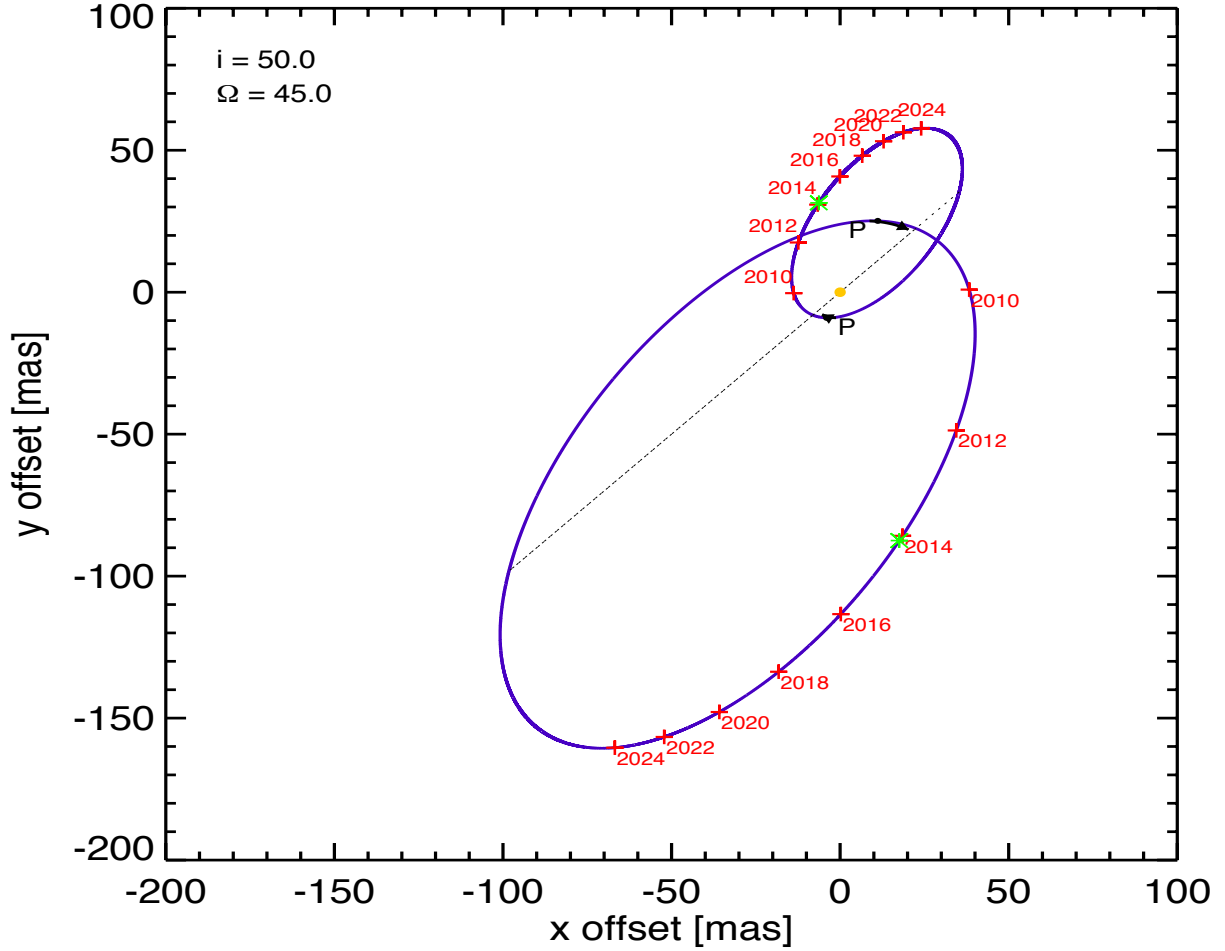


Figure 4.8: Sky-projected orbit of the HD 59686 binary system assuming values of $i = 50^\circ$ and $\Omega = 45^\circ$ for the orbital inclination and longitude of the ascending node, respectively. Labeled in the orbit are the positions of each star as a function of time. The green symbol marks the position of HD 59686 A and HD 59686 B at the time of our LBT observations. The dotted line is the line of nodes, and the letter P denotes the positions of the stars at periastron. The yellow dot marks the center of mass of the system.

4.6 Discussion

4.6.1 HD 59686 Ab: a planet in a close-separation binary

Among the known S-type planets, HD 59686 Ab is very peculiar, mainly because it is part of a close-separation ($a_B = 13.6$ au) and eccentric ($e_B = 0.7$) binary system. Figure 4.9 shows the semi-major axis of the known S-type planets as a function of the binary separation. Planets exist in binaries with a wide range of separations, but it is clear that the majority of them show semi-major axes greater than $a_B \sim 100$ au. HD 59686 AB is, together with ν Octantis (Ramm et al.

2009) and OGLE-2013-BLG-0341LB (Gould et al. 2014), the binary with the closest separation of its stellar components known to harbor a planet.

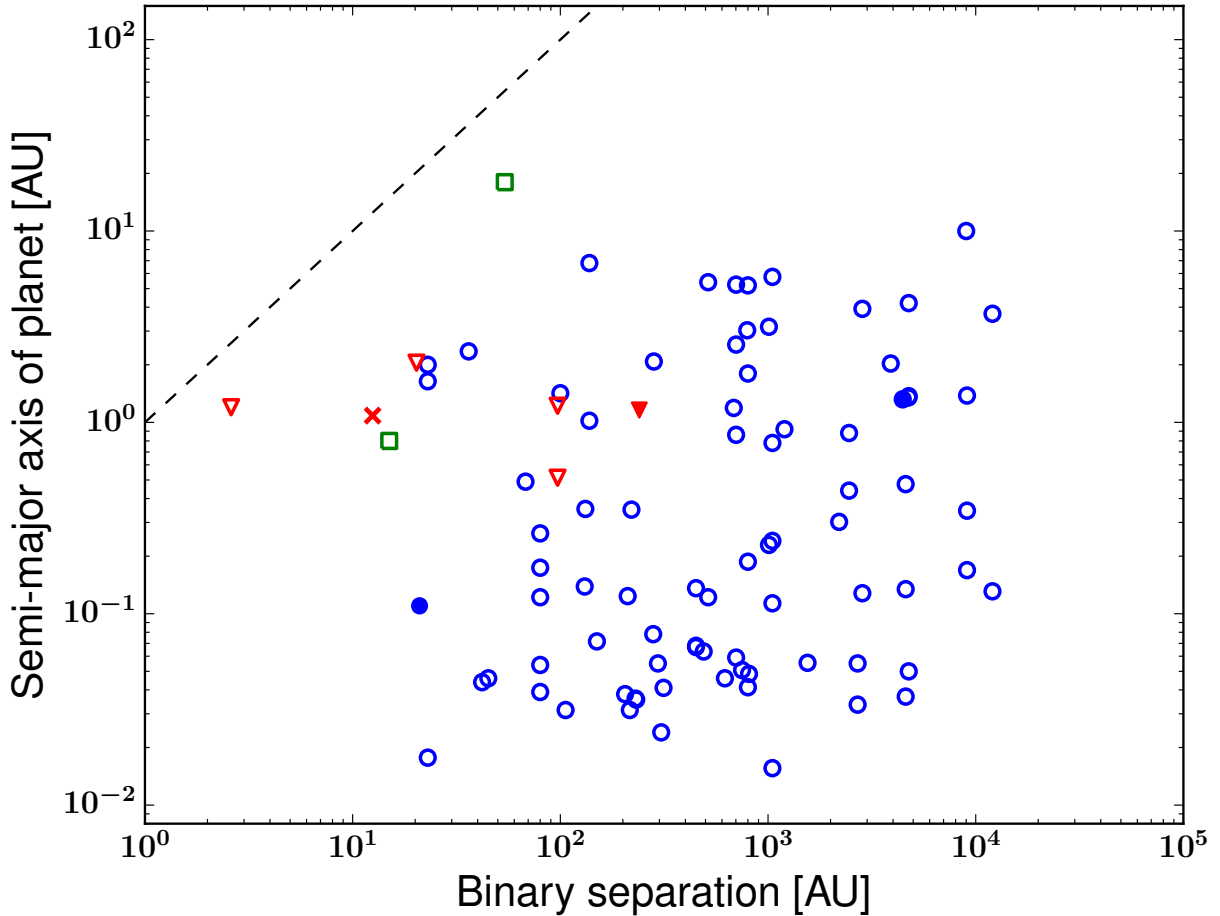


Figure 4.9: Semi-major axis of planetary companions plotted against binary separation for all known planet-hosting binary systems. Shown are binaries with MS (blue circles) and evolved subgiant/giant (red triangles) primary stars as well as two microlensing binaries (green squares), in which the spectral type of the stars is not known. The filled symbols show binaries in which the secondary star is a white dwarf. The position of the HD 59686 system is marked with a red cross. The dashed line marks the 1:1 relation between planet semi-major axis and binary separation. Most of the discovered planets are found in binary stars with separations greater than ~ 100 au.

The microlensing Earth-mass planet OGLE-2013-BLG-0341LB b is orbiting at approximately ~ 0.8 au from its host star, and the microlensing models are compatible with a binary separation of either ~ 10 or 15 au. The case of ν Oct is particularly remarkable, since the separation of the binary pair is only $a_B \sim 2.6$ au and the conjectured planet is orbiting at $a_p \sim 1.2$ au; roughly at half the distance between both stars. Interestingly, similar to HD 59686 AB, the ν Oct system is composed of a single-lined K-giant binary, with a secondary star mass of $\sim 0.55 M_\odot$. Moreover,

the ν Oct system is slightly eccentric: $e \sim 0.25$ (Ramm 2015). As we discussed below, the existence of giant planets in both systems is very hard to explain by traditional theories.

There are two additional systems (not included in the plot) with reported companions at $a \lesssim 20$ au: KOI-1257 (Santerne et al. 2014) and α Cen (Dumusque et al. 2012). KOI-1257 b is a transiting giant planet with a period of $P = 86.6$ days that is part of a binary system with $a_B \sim 5.3$ au. However, the nature of the massive outer companion in the system is unconstrained at present; it could be anything, a planet, a brown dwarf or a stellar object (Santerne et al. 2014). On the other hand, in α Cen AB, the stellar nature of the binary components is well established, but the existence of a terrestrial planet orbiting at ~ 0.04 au has recently been questioned (Hatzes 2013; Rajpaul et al. 2016), implying that most likely there is no planet in the α Cen system. This would make HD 59686 AB, and ν Oct, unique systems in which to study the formation of giant planets in short-separation binaries.

Another striking property of the HD 59686 system is the high eccentricity of the binary pair. With a value of $e_B = 0.729^{+0.004}_{-0.003}$, this is the most eccentric close-separation binary ($a_B \lesssim 20$ au) known to harbor a planet. This implies that, at periastron, both stars are separated by only ~ 3.6 au. The formation of such a system presents a tremendous challenge to current planet formation theories as the smallest binary separation in which giant planets could form is thought to be ~ 20 au (see Haghighipour 2009 and references therein). On the other hand, simulations have shown that terrestrial planets may form in close-separation binaries up to $\sim 0.2q_b$, where q_b is the binary pericenter distance (Quintana et al. 2007). Therefore, this possibility is not directly excluded in the HD 59686 system, as terrestrial planets might have formed up to a distance of ~ 0.7 au from the primary star.

4.6.2 Nature of the stellar object HD 59686 B

With the mass for HD 59686 B constrained in the range $0.53\text{--}0.69 M_\odot$ derived from dynamical simulations, there are two options for this stellar companion: it may be a typical dwarf star or, more interestingly, a white dwarf (WD). The latter possibility is not rare as there are currently three known circumstellar planets orbiting stars with WD companions: GL 86 (Queloz et al. 2000), HD 27442 (Butler et al. 2001), and HD 146513 (Mayor et al. 2004). Interestingly, the system GL 86 AB is also a close-separation binary with a semi-major axis of $a_B = 18.4$ au. With the currently available data we cannot assess the nature of the stellar object HD 59686 B with certainty, but nevertheless, we can investigate whether the WD scenario is plausible given the current orbital parameters and derived masses of the HD 59686 system.

If HD 59686 B is indeed a WD, then its mass must originally have been greater than the mass of HD 59686 A ($1.9 M_\odot$) because it evolved faster to a later stage of the stellar evolution. The

problem now resides in estimating the initial MS mass of HD 59686 B. The initial-final mass relationship (IFMR) for WDs has been a subject of intense research in the past (Weidemann 1977, 1987, 1990; Jeffries 1997). More recently, Kalirai et al. (2009) calibrated a semi-empirical relation for the IFMR using several WDs found in a set of globular clusters in the Milky Way. With this relation we can estimate an initial MS mass for HD 59686 B of $\sim 0.7\text{--}2.3 M_{\odot}$ for WD masses of 0.53 and $0.69 M_{\odot}$, respectively. The latter mass satisfies our initial constraint of $M_B > 1.9 M_{\odot}$. This means that, for the upper limit of our mass estimate, HD 59686 B may have evolved off the MS to end its life as a WD of $\sim 0.69 M_{\odot}$.

To investigate whether this scenario is plausible, we used the detailed binary evolution code BSE (Hurley et al. 2002) to evolve a binary star pair with a set of initial orbital properties. The initial binary masses were set to 2.3 and $1.9 M_{\odot}$. We considered a range of initial periods and eccentricities of $P = 5000\text{--}30000$ days in steps of 100 days and $e = 0.50\text{--}0.99$ in steps of 0.01. The system was then evolved until the stellar types of the two stars were a WD and a HB star. The results of the simulations are shown in Fig. 4.10, where the final periods and eccentricities are plotted for all the different initial orbital configurations that led to a WD-HB pair with similar masses as those observed in the HD 59686 system. The left panel shows the results for a mass-loss prescription given by the traditional Reimers formula for red giants (Reimers 1975). It is clear that no set of initial conditions can reproduce the current orbital properties of the HD 59686 system, namely a period of $P = 11680$ days and eccentricity of $e = 0.729$. Orbits with periods of a few thousands days or less are fully circularized, and the small fraction of systems with a high eccentricity ($e \sim 0.6$) shows very long orbital periods of ~ 50000 days.

The right panel of Fig. 4.10 shows the final periods and eccentricities for the same initial configurations as discussed before, but with an increased mass-loss rate controlled by the enhanced wind parameter B_W . This parameter was first introduced by Tout & Eggleton (1988) to explain the mass inversion of the RS CV binary star Z Her. In this scenario it is assumed that the mass loss is enhanced through tidal interactions with a binary companion. Tidally enhanced stellar winds have been used since then to account for several phenomena related to giant stars in binary systems, such as the eccentricities of barium stars (Karakas et al. 2000; Bonačić et al. 2008), symbiotic channel for SNe Ia progenitors (Chen et al. 2011), morphology of HB stars in globular clusters (Lei et al. 2013), and long-period eccentric binaries with He WD (Siess et al. 2014) and SdB companions (Vos et al. 2015).

The efficiency of the tidally enhanced stellar wind was set to $B_W = 10^4$ by Tout & Eggleton (1988) to fit the observed parameters of Z Her, but this value may vary depending on the specific system considered. The results plotted in the right panel of Fig. 4.10 are for a value of $B_W = 10^4$, but we note that we are able to reproduce the orbital parameters of the HD 59686 system with several values of B_W ranging from $\sim 5000\text{--}10000$. A striking difference with the case of a standard mass loss is that now a considerable fraction of the simulations shows eccentric orbits

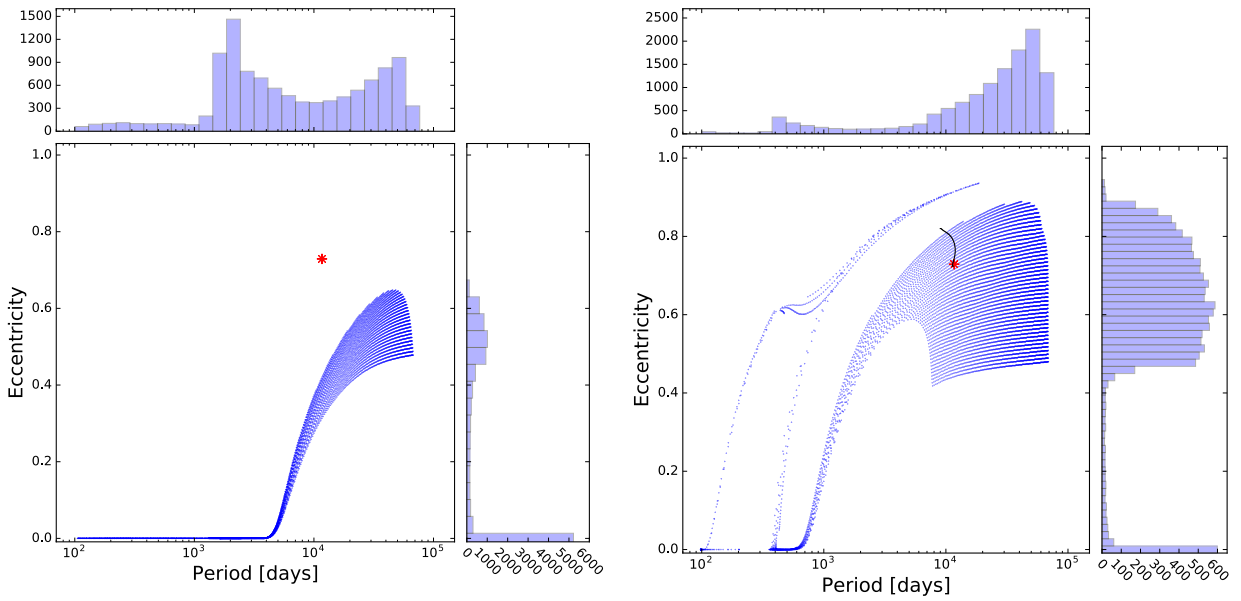


Figure 4.10: Final periods and eccentricities resulting from all simulations that led to the formation of a HB giant star with a WD companion. The initial masses of the stars were 1.9 and $2.3 M_{\odot}$. We also show histograms reflecting the distribution of final periods and eccentricities. The position of the HD 59686 system is marked with a red asterisk. *Left panel:* Results for $B_W = 0$, meaning that the mass loss is treated with the traditional Reimers prescription. It is clear that none of the simulations can reproduce the HD 59686 system. In the majority of the cases the orbit is fully circularized due to tidal interactions during the AGB phase. *Right panel:* Results for an enhanced mass-loss rate ($B_W = 10^4$) showing that a large fraction of initial orbital conditions lead to long-period and eccentric binaries similar to the HD 59686 system. The black solid line marks the period and eccentricity evolution of the model that agrees best with the orbital properties of HD 59686 AB.

in the range ~ 0.40 – 0.85 with periods of a few tens of thousand days, very similar to HD 59686 AB. The model that best reproduces HD 59686 AB (black solid line) has a final eccentricity and period of $e_f = 0.724$ and $P_f = 11555$ days (with initial values of $e_i = 0.82$ and $P_i = 9000$ days), very close to the actual observed values of the HD 59686 system. These results show that the WD scenario for HD 59686 B is plausible, provided that its progenitor passed through an enhanced wind mass-loss phase during the AGB evolution. It is worth mentioning, however, that the previous calculations do not include the presence of a planet in the binary system. If the planet HD 59686 Ab existed before the presumed evolution of the stellar companion HD 59686 B, then the change from MS star to giant star to white dwarf could have affected the evolution of the planetary body.

Regardless of the nature of the stellar object HD 59686 B, the formation of a planet with a stellar companion at 13.6 au with a periastron distance of only 3.6 au presents serious challenges to standard planet formation theories (e.g., [Hatzes & Wuchterl 2005](#)). In the core-accretion model (e.g., [Mizuno 1980](#); [Pollack 1984](#); [Lissauer 1993](#)), giant planets close to their host stars are expected to form beyond the snow line and then migrate inward to reach their current positions. For a mass of $\sim 1.9 M_\odot$ the snow line of HD 59686 A is located at ~ 9.7 au (assuming the model of [Ida & Lin 2005](#)). However, with an eccentric stellar companion at 13.6 au, the protoplanetary disk around the primary star would be truncated at around 1 au or less ([Pichardo et al. 2005](#)), preventing the formation of a giant planet at this separation from the host star ([Eggenberger et al. 2004](#)). Similarly, a formation in situ at $\sim 1 - 2$ au by disk instability (e.g., [Kuiper 1951](#); [Toomre 1964](#); [Boos 2000](#)) is highly unlikely as the required temperature for efficient cooling would be too high for the protoplanetary disk to remain bound to the central star ([Rafikov 2005](#)). Additionally, giant planets are not expected to form by disk instability in binary systems with separations of $a_B \lesssim 20$ au and eccentricities of $e_B \gtrsim 0.4$ ([Jang-Condell 2015](#)).

4.6.3 Possible origin of the planet HD 59686 Ab

With the increasing number of planets found in non-conventional configurations in binary systems, in both P-type and S-type orbits, new mechanisms have been proposed to explain their origin. For instance, [Schleicher & Dreizler \(2014\)](#) developed a model to explain circumbinary planets in the close binary NN Ser from the ejecta of common envelopes. They also extended their model to predict the masses of 12 planetary candidates around post-common envelope binaries (PCEBs) listed by [Zorotovic & Schreiber \(2013\)](#), showing a good agreement in several systems. Additionally, [Perets \(2010\)](#) and [Tutukov & Fedorova \(2012\)](#) have discussed the possibility of forming second-generation (SG) circumstellar planets in evolved binary systems. The main idea of SG planets is that an evolved star transfers mass to its companion, and when the binary separation is small enough, this could lead to the formation of an accretion disk around

the primary star with sufficient mass to form planets. If the stellar object HD 59686 B is confirmed to be a WD, then this scenario appears as an interesting alternative to explain the origin of HD 59686 Ab.

In principle, this system would satisfy several expected observational characteristics from SG planets. As stated by [Perets \(2010\)](#), SG planets are expected to be almost exclusively found in evolved binary systems with compact objects, such as WD or neutron stars. They are also likely to be more massive than normal first-generation planets; with a mass roughly constrained between $\sim 7\text{--}9 M_{\text{Jup}}$, HD 59686 Ab is among the most massive exoplanets detected so far. SG planets could reside in regions of orbital phase space forbidden to pre-existing planets by dynamical arguments. HD 59686 Ab is marked as unstable or on the border of stability by some dynamical criteria ([Holman & Wiegert 1999](#); [Mardling & Aarseth 2001](#)), although detailed N-body integrations allow stability for a certain parameter space including both prograde and retrograde orbital configurations ([Trifonov et al. 2016](#), in prep.). For the prograde case, the bootstrap dynamical test yielded a small sample of long-term stable fits consistent with the bootstrap distributions at the 1 sigma confidence level. These prograde fits are locked in secular resonance with aligned orbital periapsis. The best dynamical fits assuming a retrograde orbit have slightly better quality (smaller χ^2) and are long-term stable. It is worth noting that there is evidence suggesting that the planet in the ν Oct system, that is, the tight binary with $a_B = 2.6$ au and a K-giant primary, is in a retrograde orbit ([Eberle & Cuntz 2010](#); [Goździewski et al. 2012](#); [Ramm 2015, 2016](#)).

Although the SG planet scenario may seem attractive, we cannot discard the possibility that the current configuration of the HD 59686 system may be the result of past dynamical interactions in the native star cluster ([Pfahl & Muterspaugh 2006](#)). In this context, the planet HD 59686 Ab could have formed beyond the snow line around its single host star, and later, through dynamical processes, another binary star may have exchanged one of its stellar members for this single star with the already formed planet. This scenario has been invoked in the past to explain the origin of a giant planet in the system HD 188753 ([Pfahl 2005](#); [Portegies Zwart & McMillan 2005](#)). However, the existence of this planet was recently proved false by [Eggenberger et al. \(2007b\)](#). [Pfahl & Muterspaugh \(2006\)](#) estimated that dynamical interaction in the parent star clusters would deposit giant planets in roughly 0.1% of binary systems with semi-major axis of $a < 50$ au. We note that this value was obtained under several assumptions and it is unlikely that we have detected such a system in our sample, which does not contain a large number of such binaries.

Another similar, albeit slightly different possibility is that the present configuration of the HD 59686 system might have been generated in the past after the formation of the planet HD 59686 Ab was completed. In this scenario, planets can form in wide-separation binary systems that are not hostile for the planet formation process and later, through a close stellar encounter or a perturbation induced by a former third star in the system, the orbital parameters of the system may have

changed to those observed today. This possibility was first suggested by [Marzari & Barbieri \(2007\)](#), who studied the dynamical evolution of triple star systems with a primary star harboring a planet. They found that close stellar encounters or a perturbation of the original triple system may significantly change the binary orbit, leading to more eccentric and tight binaries with planets. Additionally, using numerical simulations, [Martí & Beaugé \(2012\)](#) studied the formation of the planet around γ Cep by stellar scattering and found that around $\sim 1\text{--}5\%$ of fly-by encounters involving planetary systems could lead to planets in close-separation binaries. Although this number is small, we cannot exclude this possibility for the formation of HD 59686 Ab.

4.7 Summary

By obtaining high-precision RVs of the giant star HD 59686 A for more than 12 years, we discovered a clear RV signature most likely caused by a massive ($m_p \sin i = 6.92_{-0.24}^{+0.18} M_{\text{Jup}}$) giant planet, HD 59686 Ab, at a distance of $a_p = 1.0860_{-0.0007}^{+0.0006}$ au from its host star. Additionally, we detected the strong signal of an eccentric ($e_B = 0.729_{-0.003}^{+0.004}$) binary companion, HD 59686 B, orbiting with a semi-major axis of only $a_B = 13.56_{-0.14}^{+0.18}$ au. This makes HD 59686 AB, together with ν Oct, the binary system with the closest separation of its stellar components known to harbor a giant planet. Furthermore, at periastron, the two stars are separated by just 3.6 au; a certainly hostile environment for the formation of any planet in this system.

We acquired high-resolution images of HD 59686 A using LMIRCam at the LBT telescope with the aim of investigating the nature of the stellar object HD 59686 B. We could not directly detect the star, mainly because the small expected angular separation ($\lesssim 0.12''$) from the host star poses great challenges to current PSF-subtraction techniques. It is most likely that the binary companion is a red dwarf star or a white dwarf. The binary system will be at apastron in about 2025, with an expected separation of the binary pair of around $\sim 20\text{--}21$ au. With a favorable orbital configuration it would be possible to detect the companion with a similar strategy as we followed in this work.

Regardless of the nature of the binary companion, the existence of a planet in an eccentric binary with a separation of $\lesssim 15$ au is a challenge for standard planet formation theories, namely core accretion and disk instability. It is expected that massive giant planets form in massive protoplanetary disks with $M_d \gtrsim 10^{-2} M_{\odot}$. In the HD 59686 system, a disk would be tidally truncated at roughly ~ 1 au ([Pichardo et al. 2005](#)), resulting in a disk not massive enough for the formation of giant planets ([Jang-Condell 2015](#)). Additionally, stirring by the tidal field may inhibit the growth of icy grains and planetesimals and also stabilize the disk against fragmentation ([Nelson 2000](#); [Thébaud et al. 2004, 2006](#)). Under these conditions, the in situ formation by disk instability is not a plausible mechanism for giant planet formation. However, [Rafikov & Silsbee \(2015\)](#) have

recently shown that it is possible to form planets within ~ 20 au separation binaries, provided that the protoplanetary disks are massive and only weakly eccentric. It would be interesting to test the validity of this model in the HD 59686 system.

As a different approach to the origin of HD 59686 Ab, we discussed the possibility that this planet could have formed in a second-generation protoplanetary disk, assuming that the stellar object HD 59686 B is a white dwarf. We demonstrated that given the current properties of the system, this scenario is feasible, and discussed its implications regarding the formation of HD 59686 Ab. Although not directly verifiable with the currently available data, the second-generation planet hypothesis is an attractive alternative for the origin of HD 59686 Ab as this system accounts for several observational characteristics for this type of planets (see [Perets 2010](#)). Another mechanism that may explain the origin of the planet, although unlikely and hardly verifiable, is the past exchange of stellar companions through dynamical interaction with the native star cluster.

Our detailed analysis of the extensive RV data set of HD 59686 A supports the hypothesis that planets can exist in close binary systems with separations of $a_B \lesssim 20$ au, contrary to the theoretical expectations ([Whitmire et al. 1998](#); [Nelson 2000](#)) and the recent observational support showing that short-separation binaries are rarely found among *Kepler* planet hosts ([Wang et al. 2014](#)). However, the question of how such planets may have formed remains unanswered as none of the standard theories can satisfactorily explain the origin of HD 59686 Ab. In this context, systems such as HD 59686 and ν Oct may become benchmark objects in the study of planet formation in tight binaries.

Summary and Outlook

5.1 Review of the thesis

We have studied extrasolar planets around evolved stars from different perspectives. First, we have contributed with the discovery and characterization of a close-in transiting planet around an RGB star, and with the detailed analysis and independent confirmation of one, of the only two, hot Jupiters orbiting a giant star. Second, we have discovered one of the few circumstellar planets residing in a close-separation binary system with profound implications for planet formation theories in tight binaries.

In Chapter 2, we presented the discovery of the transiting warm Jupiter planet Kepler-432 b that orbits its giant host every 52 days. Kepler-432 b is only the fifth planet found to transit a giant star. Additionally, with a mass of $M_p = 5.84 \pm 0.05 M_{\text{Jup}}$, it resides in a region with a lack of planets, which makes it a valuable data point for studies of planetary interiors. This is because the planet is not as close to its host star ($a \gtrsim 0.1$ au) to receive extreme levels of irradiation – hence the “warm” and not “hot” Jupiter – and does not present a significantly inflated radius, which further complicates the modeling of giant planet interiors. Also, the detection of this planet around an intermediate-mass star presents evidence against the halted migration scenario that has been proposed before to explain the scarcity of short-period planets around giant stars. On the other hand, it supports the idea that these close-in planets reach their current positions via gravitational migration.

In Chapter 3, we performed a detailed analysis of the Kepler-91 system. The planet Kepler-91 b is of particular importance since it is one of the two hot Jupiter planets discovered around a giant star, and the only one with a stellar host with $R_\star > 6 R_\odot$. We have modeled the transit

light curve of the planet including effects of the out-of-transit modulations, together with our RV observations and the publicly available RV measurements of this star. We derived a mass of $M_p = 0.67^{+0.06}_{-0.06} M_{\text{Jup}}$, that is a factor of two better than previous estimates. We have also derived a significant non-zero orbital eccentricity of $e = 0.0306^{+0.0064}_{-0.0047}$, which is puzzling as the orbits of planets so close to their host stars are expected to be fully circularized. We suggest that this can be due to a smaller tidal dissipation inside the planet than what is typically adopted for hot Jupiters or by the presence of an additional companion. The latter has some ground as we have found an RV linear of $0.0523 \text{ m s}^{-1} \text{ d}^{-1}$ that may be due to an extra body in the system. Nevertheless, more observations are needed to assess its true nature.

In Chapter 4, we presented the discovery and characterization of the S-type planet HD 59686 Ab that is part of a close binary with a separation of its stellar components of $a_B = 13.56^{+0.18}_{-0.14} \text{ au}$. The giant planet has a mass of $m_p \sin i = 6.92^{+0.18}_{-0.24} M_{\text{Jup}}$ and orbits around the primary giant star at a distance of $a_p = 1.0860^{+0.0006}_{-0.0007} \text{ au}$, while the secondary star was found to have a minimum mass of $0.5296^{+0.0011}_{-0.0008} M_{\odot}$; most likely a red or a white dwarf. Also, this is the most eccentric ($e_B = 0.729^{+0.004}_{-0.003}$) close-separation binary known to harbor a planet, which further complicates the explanation of the origin of this planet by traditional theories. Nor the standard core accretion or the disk instability model can account for the formation of HD 59686 Ab. Alternative scenarios include the formation of the planet as a second-generation one, or dynamical interactions in an early phase of the system's lifetime; none of them directly verifiable. It is important to emphasize that HD 59686 Ab is only the second S-type planet found in a binary system in which the separation of its stellar components is less than $\sim 15 \text{ au}$, which makes it an important object for the study of planet formation theories in tight binaries.

In the following sections, I will address some questions arising from this thesis and the possible directions to follow. Afterwards, I will briefly describe some of the current ongoing and future projects in the exoplanet field in general.

5.2 Close-in planets around evolved stars

Origin of the close-in planet population in evolved stars

As shown in Fig. 3.6, the region of $a < 0.5 \text{ au}$ is scarcely populated. These objects may be either members of the tail in the period distribution of planets around massive and intermediate-mass stars, or part of a more numerous group of short-period planets around MS A and F stars that do not survive the RGB phase. The latter scenario implies that these planets form, but they are tidally engulfed by their hosts as soon as the stars ascend the RGB. The two close-in planets

analyzed in this thesis suggest that this explanation can account for the lack of short-period planets observed in red giants that had their first ascent up the giant branch, or that have a radius larger than $\sim 10 R_{\odot}$. On the other hand, examples like Kepler-91 b and EPIC 211351816.01 (Grunblatt et al. 2016) might be suggesting that tidal interactions are not as strong as previously thought (Schlaufman et al. 2013), at least for stars just ascending into the RGB. In addition, in the last few years there has been a growing number of detections of close-in planets both in giant and subgiant stars, mainly thanks to *Kepler* observations. This could also mean that an observational bias may be partly responsible for the paucity of close-in planet around giant stars. Clearly, more detections are needed to reach a definitive conclusion and future large-scale transit surveys targeting evolved stars will greatly contribute to this matter.

Characterization of transiting planets in evolved stars

So far, the population of giant planets around evolved stars has been intensively investigated using the RV technique, but little is known about their transiting counterpart. Transiting giant planets around evolved stars are expected to provide important information about the planet internal composition and structure, as the planet radius and density can be derived, provided that RV observations are also available. The planets presented in this thesis are a first step towards a more complete characterization of transiting planets around giant stars. Looking for warm Jupiters around evolved stars can help to put constraints to models of giant planet formation for moderately irradiated planets. Additionally, it was recently suggested by Lopez & Fortney (2016) to look for possible signs of re-inflation in the radii of gas giants with periods larger than 10 days around post-MS host. This can serve as a way to distinguish between models that explain the large radii of gas giants by depositing a fraction of the incident irradiation into the planet interior and models that simply slow the planet radiative cooling, delaying its contraction. Therefore, important insights about the composition and physical processes in the interior of giant planets can be obtained by the characterization of transiting planets around evolved stars.

How are planetary systems affected by stellar evolution

A crucial part of planetary science is to understand how planets evolve after the host star leaves the MS. So far, the main progress has come from the theoretical side with studies that calculate the orbits of planets in stars with a wide range of initial masses. A crucial prediction from these studies is that tidal interaction can be more important than previously thought (e.g., Villaver & Livio 2009). However, most of these studies lack the observational counterpart and they do not take into account the orbital properties of the planets that have actually been found in evolved stars. A different approach would be to start from the orbital distribution of planets around giant

stars, and then integrate the equations of stellar evolution backward in time to properly constrain the star-planet interaction during the RGB phase. Out of the sample of planets around giant stars, the transiting ones are the most accurately characterized, and it would be desirable to perform such analysis to investigate the influence of the stellar evolution on the properties of these planets.

5.3 Circumstellar planets in binary systems

Origin of S-type planets in close binary systems

Circumstellar planets residing in close-separation binary systems with $a_B \lesssim 20$ au are a challenge for planet formation theories mainly because of the influence that the perturber star can exert at the early stages of planet formation, preventing the growth of planetesimals in the disk around the primary star. The planet HD 59686 Ab presented in this thesis joins ν Oct Ab as the S-type planets with the closest separation of their stellar components. There have been attempts to explain the origin of other S-type planets in binaries with $a_B \approx 20$ au, like for example, γ Cep Ab (e.g., [Kley & Nelson 2008](#)) reaching satisfactory explanations under certain specific conditions. The next logical steps will be to test the validity of such models for planets like ν Oct Ab and HD 59686 Ab to see if they can account for their origin. A complementary approach would also be to test if the recently proposed models of in-situ planet formation (e.g., [Boley et al. 2016](#); [Huang et al. 2016](#)), in which giant planets can form inside the ice line, are a viable alternative to the origin of these systems.

5.4 Future and ongoing exoplanet projects

CARMENES

CARMENES stands for Calar Alto high-Resolution search for M dwarfs with Exoearths with Near-infrared and optical Échelle Spectrographs ([Quirrenbach et al. 2010, 2012](#)). It is a next-generation instrument that started its science operations in January this year (2016) at the 3.5m telescope at the Calar Alto Observatory. It consists of two separated spectrographs covering the wavelength ranges from 0.52–0.96 μm and from 0.96–1.71 μm with a spectral resolution of $R = 82\,000$. Both spectrographs are housed in temperature-stabilized vacuum tanks to enable a long-term RV precision of $\sim 1 \text{ m s}^{-1}$. The science objective of CARMENES is to carry out a survey of ~ 300 M-dwarf stars with the goal of detecting low-mass planets in their habitable zones. The unique simultaneous observations with the visual and near-IR spectrographs will

enable a very detailed study of the activity and temporal variations in active stars, and will be fundamental in the clear distinction between RV signals caused by intrinsic activity and the Doppler reflex motion induced by an unseen planetary companion.

Gaia

The *Gaia* astrometric spacecraft ([Gaia Collaboration 2016](#)) was launched on 19 December 2013, and since then it has been continuously scanning the sky to perform astrometric, photometric, spectrophotometric and spectroscopic measurements. On 14 September 2016 the first public data release (DR1, [Lindergren et al. 2016](#)) was provided containing positions, parallaxes and proper motions for stars in common between the Tycho-2 Catalogue ([Høg et al. 2000](#)) and *Gaia* ([Michalik et al. 2015](#)). The goal of the mission is to observe around one billion objects brighter than $G = 20$ mag including the bright objects down to magnitude 2–3. *Gaia* will address a broad variety of science cases, including the exploration of giant exoplanets in the Milky Way. *Gaia* will be capable of probing a poorly explored area in the parameter space of exoplanetary systems (up to a few au), allowing actual masses (rather than lower limits) to be measured. It is expected that *Gaia* will detect astrometrically on the order of 20,000 Jovian exo-planets ([Sozzetti 2011](#); [Perryman et al. 2014](#)). The nominal survey will last five years, with possibly one year of extension.

ESPRESSO

ESPRESSO stands for Echelle SPectrograph for Rocky Exoplanets and Stable Spectroscopic Observations ([Pepe et al. 2014](#)). It is a next generation high-resolution spectrograph that will operate at the VLT. ESPRESSO will combine efficiency and extreme spectroscopic precision to achieve a gain of two magnitudes with respect to its predecessor HARPS, and an RV precision of around 10 cm s^{-1} . The main science case of the instrument will be the search and characterization of Earth-like planets in the habitable zone of nearby G to M-dwarfs. Additionally, it will also investigate the possible variability of fundamental physical constants and the chemical composition of stars in nearby galaxies. It is expected to start operations in $\sim 2016 - 2017$.

TESS

The Transiting Exoplanet Survey Satellite (TESS; [Ricker et al. 2014](#)) will employ four wide-field optical CCD cameras to monitor at least 200,000 MS dwarf stars looking for slight brightness changes caused by planetary transits. It will be the first space mission intended to survey the

whole sky in the search for transits. The launch of the satellite is due for December 2017 and the expected duration of the mission is two years. The stars monitored by TESS will be 10–100 times brighter than those surveyed by the *Kepler* mission, thus allowing an easier characterization of potential planets with follow-up RV observations. It is expected that TESS will discover thousands of exoplanets in orbit around the brightest stars in the sky. Additionally, TESS will be sensitive to planets with orbital periods of $\lesssim 20$ days in giant star hosts (Campante et al. 2016), thus allowing to probe a parameter space that has remained largely inaccessible to RV surveys for low planetary masses.

PLATO 2.0

The PLANetary Transits and Oscillations of stars (PLATO 2.0; Rauer et al. 2014) mission will search for terrestrial exoplanets in the habitable zone of solar-type stars with the aim of characterizing their bulk properties. It is expected that PLATO 2.0 will start its operations in $\sim 2022 - 2024$, with a mission duration of six years. The instrument consists of 34 small aperture telescopes providing a wide field-of-view of 2232 deg^2 and a photometric magnitude range of 4–16 mag. Asteroseismology will be performed for the bright targets to obtain highly accurate stellar parameters, including masses, radii and ages. PLATO 2.0 will observe up to 1,000,000 stars with the aim of detecting and characterizing hundreds of small planets, and thousands of planets in the Neptune to gas giant regime out to the habitable zone. It will therefore provide the first large scale catalogue of bulk characterized planets with accurate radii, masses, mean densities and ages. Unlike TESS, PLATO 2.0 will address the science case of characterizing rocky planets at intermediate orbital distances ($a > 0.3 \text{ au}$) around solar-like stars, which remains largely unexplored by current observations.

In summary, this and the coming years are an exciting time for exoplanet science with several dedicated surveys currently ongoing and others with plans to start in the near future. The combination of the transit and RV techniques, together with the synergies with asteroseismology, will be of critical importance to the further characterization of Earth-like planets in the habitable zone of their host stars. We are moving to an era in which large numbers of fully characterized Earth-like planets will be available. These planets might become the prime targets for spectroscopic transit follow-up observations of their atmospheres (using, e.g., JWST¹, E-ELT²), and pave the way to the detection of the first tracers of life beyond the Solar System.

¹<http://www.jwst.nasa.gov>

²<http://www.eso.org/e-elt>

Appendix **A**

Radial velocity observations of Kepler-432

Table A.1 lists the FIES (16 observations) and CAFE (11 observations) RVs with their uncertainties, total exposure times, signal-to-noise (S/N) ratios per pixel at 5500 Å, and bisector velocity spans (BVS) of the cross-correlation function. As the FIES uncertainties are around a factor of three smaller, we only provide the measurements of the BVS for the FIES RVs.

Table A.1: CAFE and FIES radial velocity measurements of Kepler-432.

BJD (− 2 450 000)	RV km s ^{−1}	σ_{RV} km s ^{−1}	Exp. Time sec	S/N/pixel @5500 Å	BVS km s ^{−1}
CAFE					
6826.63307	−36.018	0.014	5400	25	–
6827.64045	−36.017	0.029	5400	16	–
6828.62402	−35.976	0.019	5400	22	–
6835.64888	−35.799	0.016	5400	26	–
6836.63077	−35.808	0.017	5400	22	–
6837.63356	−35.820	0.025	5400	16	–
6838.63076	−35.783	0.024	5400	20	–
6839.63282	−35.830	0.017	5400	24	–
6858.56617	−36.314	0.029	5400	18	–
6870.39070	−36.125	0.019	5400	19	–
6906.41528	−36.316	0.023	4500	21	–
FIES					
6841.71887	−35.409	0.008	1800	31	−0.001
6842.71994	−35.512	0.009	1800	30	0.004
6843.71619	−35.610	0.007	1800	33	−0.002
6844.72316	−35.653	0.009	1680	29	−0.001
6854.70204	−35.704	0.006	2400	41	−0.003
6855.69674	−35.693	0.008	2700	44	−0.007
6856.68809	−35.680	0.005	2700	41	−0.002
6860.40078	−35.632	0.008	1800	34	−0.005
6875.41274	−35.418	0.007	2400	36	0.006
6880.52282	−35.327	0.006	2400	44	0.002
6892.55722	−35.223	0.007	2400	35	−0.004
6901.41459	−35.716	0.007	2400	36	−0.006
6902.46355	−35.719	0.007	2400	31	−0.004
6903.52509	−35.704	0.006	2400	38	−0.001
6916.36055	−35.565	0.013	1800	24	0.012
6936.46518	−35.234	0.006	2400	44	−0.001

Radial velocity data of Kepler-91 and posterior samples from the MCMC fitting

Table B.1 lists the CAFE (9 observations) and FIES (9 observations) RVs with their uncertainties, along with the additional RV datasets taken with HRS ([Barclay et al. 2015](#)) and HDS ([Sato et al. 2015](#)). Figure B.1 shows the posterior distributions of the 24 parameters of the MCMC planet model that fits together the RV and photometry data. Similarly, Fig. B.2 plots the posteriors of the physical properties of the planet Kepler-91 b derived from the fitted parameters.

Table B.1: CAFE, FIES, HRS, and HDS radial velocity measurements of Kepler-91.

BJD (- 2 454 833)	RV km s ⁻¹	σ_{RV} km s ⁻¹
CAFE		
1993.459704	-62.357	0.021
1994.459932	-62.324	0.024
1995.443402	-62.252	0.022
2001.568860	-62.251	0.028
2002.581543	-62.201	0.021
2003.569116	-62.255	0.027
2004.571943	-62.321	0.022
2005.567403	-62.352	0.020
2006.566052	-62.332	0.023
FIES		
2008.688714	-61.994	0.014
2009.689587	-62.008	0.013
2010.686171	-62.076	0.011
2011.694059	-62.125	0.014
2021.663522	-62.007	0.015
2022.561960	-62.064	0.024
2023.648498	-62.111	0.014
2369.420687	-62.052	0.017
2382.643678	-62.033	0.018
HRS ¹		
1208.86670891	0.114	0.024
1266.71041653	0.021	0.018
1267.70865078	-0.025	0.020
1268.70698350	-0.046	0.017
1271.68968502	0.067	0.018
1275.69264679	-0.026	0.025
1300.86443801	-0.009	0.027
1358.70858740	0.096	0.018
1382.63282948	0	0.015
HDS ²		
1640.00247	0.0432	0.00461
1640.01719	0.03385	0.00458

1640.03192	0.04526	0.00503
1640.96075	0.01735	0.00736
1640.97549	0.00893	0.00734
1640.99022	0.03004	0.00639
1641.95764	-0.02428	0.00543
1641.97235	-0.02262	0.00503
1641.98708	-0.03946	0.00550
1800.69753	-0.04212	0.01738
2014.93547	0.0423	0.01056
2014.95020	0.03746	0.01363
2014.96513	0.01149	0.00876
2014.98006	0.02977	0.00796
2014.99479	0.01707	0.00612
2015.00952	0.01994	0.00861
2015.08121	0.02325	0.00659
2016.75412	-0.05212	0.00523
2016.76886	-0.0361	0.00506
2016.78360	-0.03447	0.00548
2020.04854	-0.04023	0.01348
2020.97273	0.00573	0.00572
2020.98746	0.00902	0.00473
2021.00219	0.00766	0.00517
2021.84234	0.00214	0.00499
2021.85708	0.00036	0.00525
2021.87181	-0.00669	0.00603
2022.80523	-0.04337	0.00663
2022.81828	-0.04191	0.00528

¹Data from [Barclay et al. \(2015\)](#)

²Data from [Sato et al. \(2015\)](#)

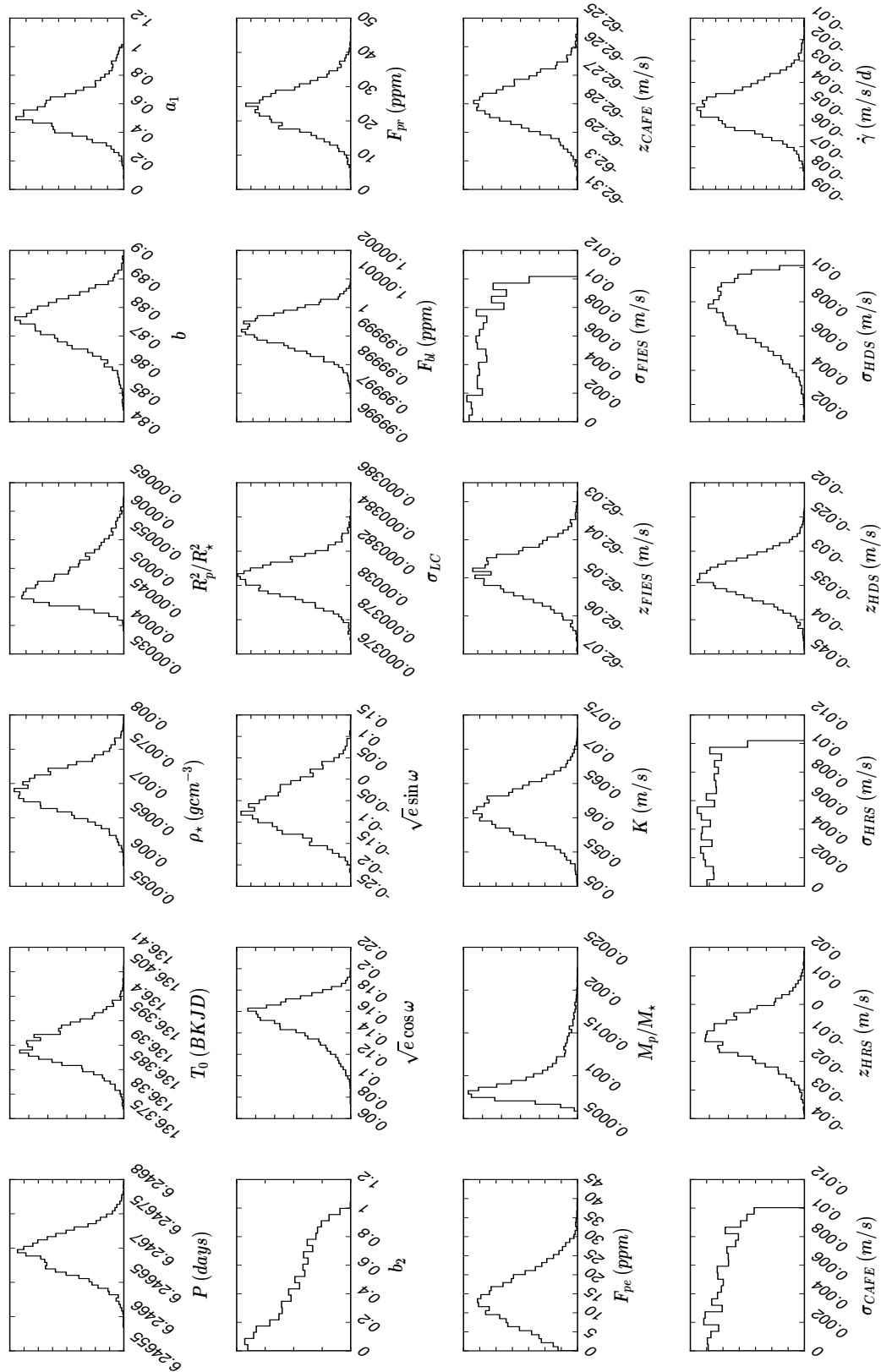


Figure B.1: Histograms of the marginalized posterior distributions of the 24 parameters included in the MCMC planet model.

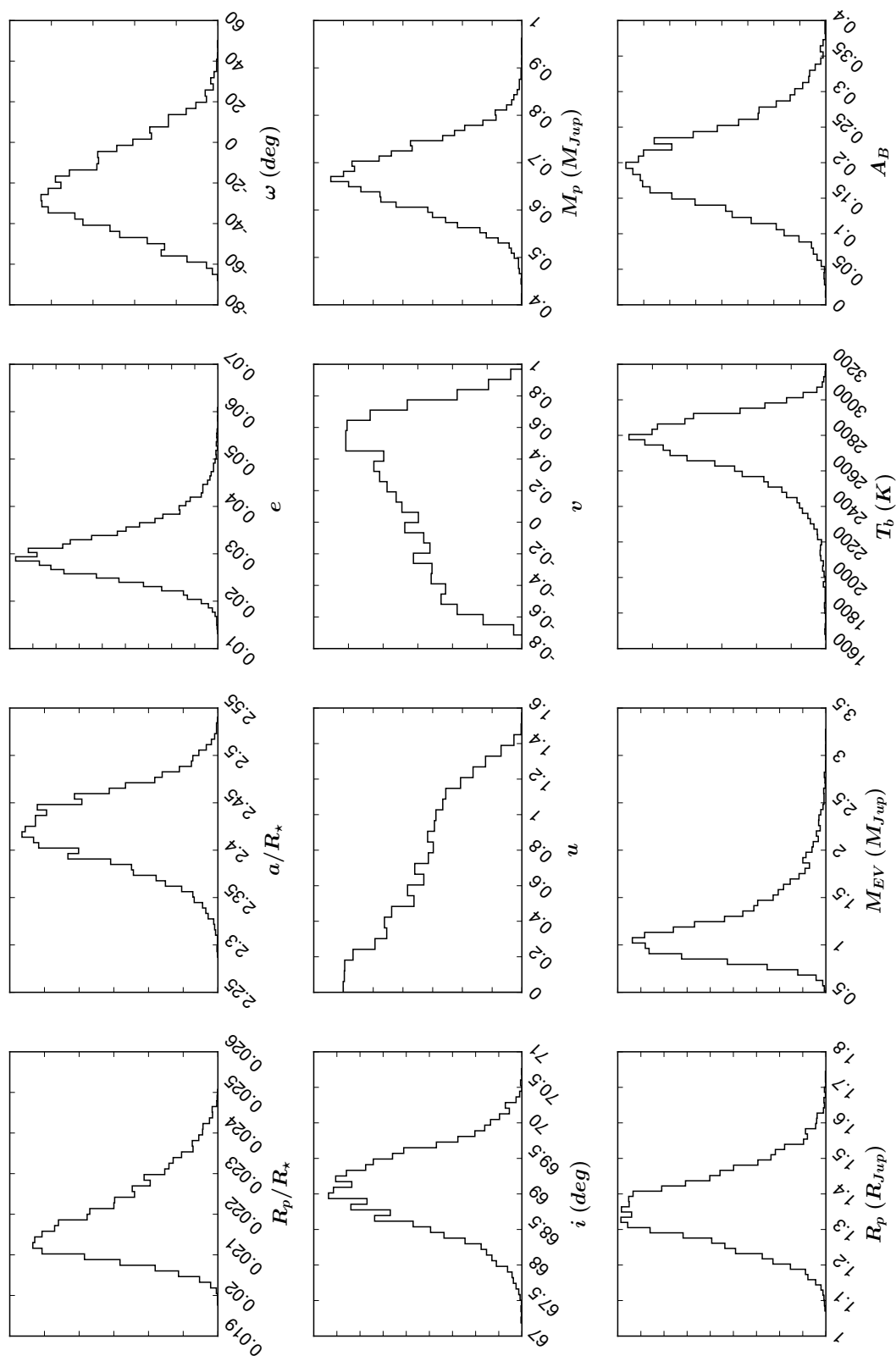


Figure B.2: Histograms of the marginalized posterior distributions of the derived physical parameters of Kepler-91 b.

Appendix **C**

Radial velocity observations of the giant star HD 59686 A

Table C.1 lists the 88 radial velocity measurements of HD 59686 A taken with the Hamilton Échelle Spectrograph.

Table C.1: Radial velocity data of HD 59686 A.

JD (-2 450 000)	RV m s ⁻¹	σ_{RV} m s ⁻¹
1482.024	1975.5	5.5
1500.997	1943.7	5.7
1572.717	1799.5	5.4
1656.661	1944.3	6.6
1856.955	1823.2	5.9
1901.932	1854.8	5.8
1931.824	1903.9	5.2
2193.010	1862.0	5.1
2195.010	1852.7	5.5
2205.951	1853.8	5.3
2222.909	1948.1	5.3
2258.822	1998.8	6.1
2259.878	2005.0	5.5
2295.803	2097.2	6.7
2297.859	2076.3	7.0
2307.741	2115.2	5.4
2361.726	2115.7	5.1
2363.702	2115.1	5.2
2384.682	2072.5	5.5
2393.666	2045.0	6.7
2531.030	1916.7	5.7
2542.027	1945.3	5.6
2560.979	2016.7	5.0
2572.001	2014.8	5.3
2589.985	2090.1	5.9
2603.962	2095.4	7.2
2615.867	2114.1	6.0
2627.828	2109.1	4.8
2665.820	2069.9	5.5
2667.827	2068.8	6.1
2699.701	1978.5	6.9
2717.703	1941.0	5.6
2933.013	2086.3	5.0
2935.001	2066.2	4.6
2965.935	2031.0	6.0

2985.961	2001.6	7.2
3023.847	1880.7	7.1
3089.720	1800.6	7.8
3111.677	1845.3	5.4
3271.031	1940.1	4.1
3289.047	1913.9	4.2
3323.978	1776.1	5.2
3354.815	1709.4	4.9
3356.924	1700.8	4.9
3358.878	1694.5	4.9
3359.926	1682.2	4.7
3400.821	1689.6	5.5
3424.723	1746.7	4.7
3442.692	1760.8	5.0
3650.050	1505.0	4.1
3698.995	1466.1	5.2
3740.995	1507.2	7.5
3858.656	1457.0	6.2
4054.948	950.1	5.5
4081.026	948.6	5.6
4123.846	840.7	5.4
4181.763	562.9	5.7
4206.721	405.5	5.0
4209.692	395.3	5.2
4226.667	259.9	5.2
4392.033	-552.3	8.0
4419.030	-804.5	6.1
4423.056	-880.3	5.9
4443.001	-1034.6	6.0
4482.832	-1574.1	6.4
4502.865	-1888.4	6.4
4553.714	-2726.7	5.3
4583.688	-3142.6	5.2
4754.005	-5322.4	5.4
4758.930	-5384.8	4.5
4882.841	-6119.8	7.2
4911.684	-6081.2	6.6
5101.054	-4894.9	6.4
5154.982	-4634.8	8.0

5174.919	-4564.0	7.8
5241.797	-4046.9	6.8
5278.702	-3739.0	6.7
5465.043	-3060.3	5.6
5566.919	-2490.5	5.0
5571.802	-2458.0	5.3
5589.800	-2371.0	5.5
5593.817	-2375.8	5.8
5619.735	-2246.6	6.6
5650.765	-2170.9	6.2
5678.691	-2131.1	5.8
5831.028	-1821.4	5.5
5863.987	-1656.3	5.8
5893.967	-1570.1	10.3

Acknowledgements

I would like to start thanking my two main advisors, Andreas Quirrenbach and Sabine Reffert, for giving the opportunity to join the IMPRS program around four years ago. Their support and scientific advice has been very important for the successful completion of this PhD thesis. Thank you for the help and support during these years, and for guiding me through this fantastic adventure. A very special thank goes also to Davide Gandolfi, whose staying at the LSW was relatively short, but it was the most fruitful one. A large part of the work presented in this thesis could not have been possible without his valuable contribution. Grazie mille!

Many thanks to the IMPRS coordinator, Christian Fendt, who is always willing to help students with whatever problems they may have. He makes all of us feel welcome, which is greatly appreciated. My stay in Heidelberg has been one of the best experiences of my life, and it has given me so much more than just scientific knowledge, and a PhD! It goes without saying that I am grateful to all the friends that I have found here, who have made my time in Heidelberg a real pleasure. Special thanks goes to (apologies if I forget someone): Agnese, Alejandro, Cristina, Eduardo, Elena, Esteban, Fabián, Fabrizio, Kathy, Luca, Steffi and Mauricio (the less handsome).

I am grateful to Sabine Reffert, Natalia Ortiz (former Kudryavtseva) and Steffi Yen, for taking the time to read and correct some parts of my thesis. I am also thankful to Stefan Brems for a super fast translation of the thesis abstract into German. Danke schön! I thought I was starting to understand some basic German, but after reading the German translation and not understanding a single word, I realize how fool I was!

I am very grateful to my wife Natalia, who I met and married in this wonderful city, for her love, support and understanding. Sin lugar a dudas, Ich hab' mein Herz in Heidelberg verloren.

Por último, pero no por eso menos importante, me gustaría agradecer a mi familia por estar siempre presente, y por demostrarme continuamente su amor incondicional.

Abbreviations and Acronyms

2MASS	Two Micron All Sky Survey
ADI	Angular Differential Imaging
ADU	Analog-Digital Unit
AGB	Asymptotic Giant Branch
ASAS	All Sky Automated Survey
au	Astronomical Unit
BC	Before Christ
BIC	Bayesian Information Criterion
BJD	Barycentric Julian Date
BVS	Bisector Velocity Span
CAFE	Calar Alto Fiber-fed Echelle spectrograph
CAT	Coude Auxiliary Telescope
CARMENES	Calar Alto high-Resolution search for M dwarfs with Exoearths with Near-infrared and optical Echelle Spectrographs
CCD	Charge-Coupled Device
CCF	Cross-Correlation Function
CEMP	Carbon-Enhanced Metal Poor
CHARA	Center for High Angular Resolution Astronomy
CHEM	Coplanar High-Eccentricity Migration

CHEOPS	CHaracterising ExOPlanets Satellite
CoM	Center of Mass
CRIRES	CRyogenic high-resolution InfraRed Echelle Spectrograph
DR	Data Release
E-ELT	European Extremely Large Telescope
ESPRESSO	Echelle SPectrograph for Rocky Exoplanets and Stable Spectroscopic Observations
FAP	False-Alarm Probability
FIES	Fibre-fed Echelle Spectrograph
FTS	Fourier Transform Spectrometer
FWHM	Full Width at Half Maximum
GLS	Generalized Lomb-Scargle
HARPS	High Accuracy Radial velocity Planet Searcher
HB	Horizontal Branch
HDS	High Dispersion Spectrograph
HEM	High-Eccentricity Migration
HJD	Heliocentric Julian Date
IDL	Interactive Data Language
IFMR	Initial-Final Mass Relationship
IR	InfraRed
IRAF	Image Reduction and Analysis Facility
IRAS	InfraRed Astronomical Satellite
JD	Julian Date
JWST	James Webb Space Telescope
KOI	Kepler Objects of Interest
LBT	Large Binocular Telescope
LBTI	Large Binocular Telescope Interferometer
LC	Long-Cadence

LLSG	Local Low-rank plus Sparse plus Gaussian-noise decomposition
LMIRCam	L/M-band InfraRed Camera
LOCI	Locally Optimized Combination of Images
MCMC	Markov-Chain Monte Carlo
MMR	Mean Motion Resonance
MS	Main Sequence
PC	Principal Component
PCA	Principal Component Analysis
PCEB	Post-Common Envelope Binary
PDF	Probability Density Function
PLATO	PLANetary Transits and Oscillations of stars mission
PSF	Point Spread Function
RGB	Red Giant Branch
RV	Radial Velocity
SdB	Subdwarf B star
SG	Second Generation
SNe	Supernovae
SPH	Smoothed Particle Hydrodynamics
TESS	Transiting Exoplanet Survey Satellite
ThAr	Thorium-Argon
TRES	Tillinghast Reflector Echelle Spectrograph
VLT	Very Large Telescope
WD	White Dwarf

Bibliography

- Aceituno, J., Sánchez, S.F., Grupp, F., et al. 2013, *A&A*, 552, A31
- Adamów, M., Niedzielski, A., Villaver, E., et al. 2012, *ApJ*, 754, 15
- Adams, F., & Laughlin, G. 2006, *ApJ*, 649, 1004
- Al-Khalili, J. 2015, *Nature*, Nature Publishing Group, 518, 164
- Anglada-Escudé, A. & Butler, R. P. 2012, *ApJS*, 200, 15
- Antonini, F., Hamers, A. S. & Lithwick, Y. 2016, arXiv:1604.01781
- Amara, A. & Quanz, S. P. 2012, *MNRAS*, 427, 948
- Anderson, D. R., Collier Cameron, A., Delrez, L., et al. 2014, *MNRAS*, 445, 1114
- Astropy Collaboration et al., 2013, *A&A*, 558, A33
- Bailey, V., Meshkat, T., Reiter, M., et al. 2014, *ApJ*, 780, L4
- Baines, E. K., McAlister, H. A., Brummelaar, T. A., et al. 2008a, *ApJ*, 680, 728
- Baines, E. K., McAlister, H. A., Brummelaar, T.A., et al. 2008b, *ApJ*, 682, 577
- Balan, S. T. & Lahav, O. 2009, *MNRAS*, 394, 1936
- Baranne, A., Queloz, D., Mayor, M., et al. 1996, *A&A*, 119, 373
- Barclay, T., Endl, M., Huber, D., et al. 2015, *ApJ*, 800, 46
- Batalha, N. M. 2014, *Proceedings of the National Academy of Science*, 111, 12647
- Batygin, K., & Stevenson, D. J. 2010, *ApJL*, 714, L238
- Batygin, K., Bodenheimer, P. H., & Laughlin, G. P. 2015, arXiv:1511.09157
- Bauer, F. F., Zechmeister, M. & Reiners, A. 2015, *A&A*, 581, 117
- Bayes, T. 1763, *An essay towards solving a problem in the doctrine of chances*. Published posthumously in *Phil. Trans. Roy. Soc. London* 53, 370–418 and 54, 296–325.
- Beckers, J. M. 1976, *Nature*, 260, 227
- Bedding, T. R., Huber, D., Stello, D., et al. 2010, *ApJ*, 713, L176

- Beers, T. C., & Christlieb, N. 2005, *ARA&A*, 43, 531
- Belorizky, D. 1938, *L'Astronomie*, 52, 359
- Benest, D. 1988, *A&A*, 206, 143
- Benest, D. 1993, *Celestial Mechanics and Dynamical Astronomy*, 56, 45
- Bergfors, C., Brandner, W., Daemgen, S., et al. 2013, *MNRAS*, 428, 182
- Biazzo, K., Frasca, A., Catalano, S., et al. 2006, *MSAIS*, 9, 220
- Bieryla, A., Hartman, J. D., Bakos, G., et al. 2014, *AJ*, 147, 84
- Bloemen, S., Marsh, T. R., Østensen, R. H., et al. 2011, *MNRAS*, 410, 1787
- Bodenheimer, P., Lin, D. N. C., & Mardling, R. A. 2001, *ApJ*, 548, 466
- Bodenheimer, P., Laughlin, G., & Lin, D. N. C. 2003, *ApJ*, 592, 555
- Boley, A. C., Granados Contreras, A. P., & Gladman, B. 2016, *ApJL*, 817, L17
- Bonačić, M., Glebbeek, E., & Pols, O. R. 2008, *A&A*, 480, 797
- Bonavita, M. & Desidera, S. 2007, *A&A*, 468, 721
- Bonfils, X., Delfosse, X., Udry, S., et al., *A&A*, 549, 109
- Boss, A. P. 1997, *Science*, 276, 1836
- Boss, A. P. 2000, *ApJ*, 536, 101
- Boss, A. P. 2006, *ApJ*, 641, 114
- Borgniet, S., Lagrange, A.-M., Meunier, N., et al. 2016, arXiv:1608.08257
- Borucki, W. J. & Summers, A. L. 1984, *Icarus*, 58, 121
- Borucki, W. J., Koch, D., Basri, G., et al. 2010, *Science*, 327, 977
- Borucki, W. J., Koch, D. G., Basri, G., et al., 2011, *ApJ*, 736, 19
- Borucki, W.J. 2016, *Rep on Prog in Physics*, 79, 036901
- Bowler, B. P., Johnson, J. A., Marcy, G. W., et al. 2010, *ApJ*, 709, 396
- Bowler, B. P. 2016, *PASP*, 128, 968
- Brandt, T. D., McElwain, M. W., Turner, E. L., et al. 2013, *ApJ*, 764, 183
- Bressan, A., Marigo, P., Girardi, L., et al. 2012, *MNRAS*, 427, 127
- Broeg, C., Fortier, A., Ehrenreich, D., et al. 2013, in *European Physical Journal Web of Conferences*, Vol. 47, *European Physical Journal Web of Conferences*, 03005
- Bromley, B. C. & Kenyon, S. J. 2015, *ApJ*, 806, 98
- Broucke, R. A. 2001, *Celestial Mechanics and Dynamical Astronomy*, 81, 321
- Buchhave, L. A., Bakos, G. A., Hartman, J. D., et al. 2010, *ApJ*, 720, 1118
- Buchhave, L. A., Latham, D. W., Carter, J. A., et al. 2011, *ApJS*, 197, 3
- Burkert, A. & Ida, S. 2007, *ApJ*, 660, 845
- Burrows, A., Hubeny, I., Budaj, J., et al. 2007, *ApJ*, 661, 502

- Butler, R. P., Marcy, G.W., Williams, E., et al. 1996, *PASP*, 108, 500
- Butler R. P., Marcy, G. W., Fischer, D. A., et al. 1999, *ApJ*, 526, 916
- Butler, R. P., Tinney, C. G., Marcy, G. W., et al. 2001, *ApJ*, 555, 410
- Candès, E. J., Li, X., Ma, Y., et al. 2009, *CoRR*, abs/0912.3599
- Cameron, A. G. W. 1978, *Moon and Planets*, 18, 5
- Campante, T., Schofield, M., Kuzslewicz, J. S., et al. 2016, arXiv:1608.01138
- Campbell, B. & Walker, G. A. H. 1979, *PASP*, 91, 540
- Carlberg, J. K., Cunha, K, Smith, V. V., et al. 2012, *ApJ*, 757, 109
- Castelli, F. & Kurucz, R. L. 2004, eprint arXiv: astro-ph/0405087
- Cappetta, M., Saglia, R. P., Birkby, J. L., et al. 2012, *MNRAS*, 427, 1877
- Chabrier, G., & Baraffe, I. 2007, *ApJL*, 661, L81
- Chaplin, W. J., Houdek, G., Karoff, C., et al. 2009, *A&A*, 500, L21
- Chaplin, W. J., & Miglio, A. 2013, *ARA&A*, 51, 353
- Charbonneau D., Brown, T. M., Latham, D. W., et al. 2000, *ApJL*, 529, L45
- Chatterjee, S., Ford, E. B., Matsumura, S., et al. 2008, *ApJ*, 686, 580
- Chen, X., Han, Z. & Tout, C. A. 2011, *ApJL*, 735, L31
- Christensen-Dalsgaard, J. 2012, *ASP Conf. Ser.*, 462, 503
- Ciceri, S., Lillo-Box, J., Southworth, J., et al. 2015, *A&A*, 573, L5
- Cieza, L. A., Padgett, D. L., Allen, L. E., et al. 2009, *ApJ*, 696, L84
- Claret, A. 2003, *A&A*, 401, 657
- Claret, A. 2004, *A&A*, 428, 1001
- Claret, A. & Bloemen, S. 2011, *A&A*, 529, 75
- Claudi, R. 2016, *Methods of Detecting Exoplanets*, *Astrophysics and Space Science Library*, 428
- Collier Cameron, A., Guenther, E., Smalley, B., et al. 2010, *MNRAS*, 407, 507
- Correia, A. C. M., Udry, S., Mayor, M., et al. 2008, *A&A*, 479, 271
- Cuntz, M. 2015, *ApJ*, 798, 101
- Cumming, A., Butler, R. P., Marcy, G. W., et al. 2008, *PASP*, 120, 531
- Currie, T., 2009, *ApJ*, 694, 171
- Cuzzi, J. N., Hogan, R. C., & Shariff, K. 2008, *ApJ*, 687, 1432
- Demory, B.-O., & Seager, S. 2011, *ApJS*, 197, 12
- De Ridder, J., Barban, C., Baudin, F., et al. 2009, *Nature*, 459, 398
- Desidera, S. & Barbieri, M. 2007, *A&A*, 462, 345
- Desidera, S. & Barbieri, M. 2010, *A&A*, 462, 345
- Desidera, S., Carolo, E., Gratton, R., et al. 2011, *A&A*, 533, 90

- Dobbs-Dixon, I., Lin, D. N. C., & Mardling, R. A. 2004, *ApJ*, 610, 464
- Döllinger, M. P., Hatzes, A. P., Pasquini, L., et al. 2009, *A&A*, 505, 1311
- Dong, S., Katz, B. & Socrates, A. 2014, *ApJ*, 781, L5
- Doppler, C. 1842, *Über das farbige Licht der Doppelsterne und einiger anderer Gestirne des Himmels*, Royal Bohemian Society of Sciences
- Doyle, L. R., Carter, J. A., Fabrycky, D. C., et al. 2011, *Science*, 333, 1602
- Duchêne, G. 2010, *ApJ*, 709, 114
- Dumusque, X., Pepe, F., Lovis, C., et al. 2012, *Nature*, 491, 207
- Duquennoy, A. & Mayor, M. 1991, *A&A*, 248, 485
- Dvorak, R. 1986, *A&A*, 167, 379
- Eastman, J., Gaudi, B. S. & Agol, E. 2013, *PASP*, 125, 83
- Eberle J. & Cuntz M. 2010, *ApJ*, 721, L168
- Eggenberger, P., Udry, S., & Mayor, M. 2004, *A&A*, 417, 353
- Eggenberger, A., Udry, S., Chauvin, G., et al. 2007a, *A&A*, 474, 273
- Eggenberger, P., Udry, S., Mazeh, T., et al. 2007b, *A&A*, 466, 1179
- Eggenberger, A. & Udry, S. 2010, Probing the Impact of Stellar Duplicity on Planet Occurrence with Spectroscopic and Imaging Observations, in *Planets in Binary Star Systems*, ed. N.Haghighipour (New York: Springer), 19
- Eggl, S., Haghighipour, N. & Pilat-Lohinger, E. 2013, *ApJ*, 764, 130
- Eggl, S., Pilat-Lohinger, E., Funk, B., et al. 2013, *MNRAS*, 428, 3104
- Endl, M., Kürster, M., & Els, S. 2000, *A&A*, 362, 585
- Endl, M., Cochran, W.D. & Kürster, M. 2006, *ApJ*, 649, 436
- Enoch, B., Collier Cameron, A. & Horne, K. 2012, *A&A*, 540, 99
- ESA 1997, *The Hipparcos and Tycho Catalogues*, ESA SP, 1200
- Espinoza, N. & Jordán, A. 2015, *MNRAS*, 450, 1879
- Esteves, L.J., De Mooij, E.J.W. & Jayawardhana, R. 2013, *ApJ*, 772, 51
- Evans, D. F., Southworth, J., Maxted, P. F. L., et al. 2016, *A&A*, 589, 58
- Fabrycky, D. C., Lissauer, J. J., Ragozzine, D., et al. 2014, *ApJ*, 790, 146
- Faigler, S. & Mazeh, T. 2015, *ApJ*, 800, 73
- Fellgett, P. 1955, *Optica Acta*, 2, 9
- Fischer, D. A., & Valenti, J. A. 2005, *ApJ*, 622, 1102
- Fischer, D. A., Howard, A. W., Laughlin, G. P., et al. 2014, *Protostars and Planets VI*, 715
- Fizeau, A. H. L. 1848, *Effet du mouvement sur le son et la lumière*, Société philomatique de Paris: Extrait des procès-verbaux des séances pendant l'année 1848, Impr. de Cosson, 81-83

- Fizeau, A. H. L. 1870, *Des effets du mouvement sur le ton des vibrations sonores et sur la longueur d'onde des rayons de lumière*, *Annales de Chimie et de Physique*, 19, 211-221
- Ford, E. B. 2006, *ApJ*, 642, 505
- Foreman-Mackey, D., Hogg, D., Lang, D., et al. 2013, *PASP*, 125, 306
- Fortney, J. J., Marley, M. S., & Barnes, J. W. 2007, *ApJ*, 659, 1661
- Fortney, J. J. & Nettelmann, N. 2010, *Space Science Reviews*, 152, 423
- Fragner, M. M., & Nelson, R. P. 2010, *A&A*, 511, A77
- Frandsen, S. & Lindberg, B. 1999, in “Astrophysics with the NOT”, proceedings Eds: Karttunen, H. & Piirola, V., anot. conf, 71
- Fressin, F., Torres, G., Charbonneau, D., et al. 2013, *ApJ*, 766, 81
- Frink, S., Quirrenbach, A., Fischer, D., et al. 2001, *PASP*, 113, 173
- Frink, S., Mitchell, D. S., Quirrenbach, A., et al. 2002, *ApJ*, 576, 478
- Furész, G. 2008, Ph.D. thesis, Univ. Szeged, Hungary
- Gaia Collaboration, 2016, ArXiv e-prints, arXiv:1609.04153
- Galilei, G. 1638 *Discorsi e dimostrazioni matematiche, intorno à due nuove scienze*, Leida, Appresso gli Elsevirii
- Gandolfi, D., Alcalá, J. M., Leccia, S., et al. 2008, *ApJ*, 687, 1303
- Gettel, S., Wolszczan, A., Niedzielski, A., et al. 2012, *ApJ*, 756, 53
- Ghezzi L., Cunha K., Schuler S. C., et al. 2010, *ApJ*, 725, 721
- Giménez, A. 2006, *A&A*, 450, 1231
- Girardi, L., Bressan, A., Bertelli, G., et al. 2000, *A&A*, 141, 371
- Goldreich, P., & Soter, S. 1966, *Icarus*, 5, 375
- Gonzalez, G. 1997, *MNRAS*, 285, 403
- Gomez Gonzalez, C. A., Wertz, O., Christiaens, V., et al. 2016a, VIP, Astrophysics Source Code Library, record ascl:1603.003
- Gomez Gonzalez, C. A., Absil, O., Absil, P.-A., et al. 2016b, arXiv:1602.08381
- Goodman, J. & Weare, J. 2010, *CAMCS*, 5, 65
- Gould, A., Udalski, A., Shin, I.-G., et al. 2014, *Science*, 345, 46
- Gould, A. 2016, *Methods of Detecting Exoplanets*, Astrophysics and Space Science Library, 428
- Goździewski, K., Słonina, M., Migaszewski, C., et al. 2012, *MNRAS*, 430, 533
- Gray, R. O. & Corbally, C. J. 1994, *AJ*, 107, 742
- Gray, D. F. 1997, *Nature*, 385, 795
- Griffin, R. F. 1967, *ApJ*, 148, 465
- Grunblatt, S. K., Huber, D., Gaidos, E. J. et al. 2016, arXiv:1606.05818

- Gu, P.-G., Lin, D. N. C., & Bodenheimer, P. H. 2003, *ApJ*, 588, 509
- Guedes, J. M., Rivera, E. J., Davis, E., et al. 2008, *ApJ*, 679, 1582
- Guenther, E. W., Hartmann, M., Esposito, M., et al. 2009, *A&A*, 507, 1659
- Guillot, T. & Showman, A. P. 2002, *A&A*, 385, 156
- Guillot, T., Santos, N. C., Pont, F., et al. 2006, *A&A*, 453, L21
- Haghighipour, N. 2006, *ApJ*, 644, 543
- Haghighipour, N. & Raymond, S. 2007, *ApJ*, 666, 436
- Haghighipour, N. 2009, arXiv:0908.3328
- Haghighipour N. 2011, *Contemp. Phys.* 52, 40338
- Haghighipour, N. & Kaltenegger, L. 2013, *ApJ*, 777, 16
- Hale, A. & Doyle, L. R. 1994, *Ap&SS*, 212, 335
- Han, I., Lee, B. C., Kim, K. M., et al. 2010, *A&A*, 509, A24
- Hastings, W. K. 1970, *Biometrika*, 57, 97
- Hatzes, A. P., Cochran, W. D., & Johns-Krull, C. M. 1997, *ApJ*, 478, 374
- Hatzes, A. P. & Cochran, W. D., 2000, *AJ*, 120, 979
- Hatzes, A. P. 2002, *Astron. Nachr.*, 323, 392
- Hatzes, A. P., Cochran, W. D., Endl, M., et al. 2003, *ApJ*, 599, 1383
- Hatzes, A. P., Setiawan, J., Pasquini, L., et al. 2004, *ESA pub.*, Vol. 538
- Hatzes, A. P., & Wuchterl, G. 2005, *Nature*, 436, 182
- Hatzes, A. P., Guenther, E. W., Endl, M., et al. 2005, *A&A*, 437, 743
- Hatzes A. P., 2013, *ApJ*, 770, 133
- Hatzes, A. P., Cochran, W. D., Endl, M., et al. 2015, *A&A*, 580, A31
- Heintz, W.D., 1978, *ApJ*, 220, 931
- Heiter, U., Kupka, F., van't Veer-Menneret, C., et al. 2002, *A&A*, 392, 619
- Hekker, S., Reffert, S., Quirrenbach, A., et al. 2006, *A&A*, 454, 943
- Hekker, S. & Meléndez, J., 2007, *A&A*, 475, 1003
- Hekker, S., Snellen, I. A. G., Aerts, C., et al. 2008, *A&A*, 480, 215
- Henry G. W., Marcy, G. W., Butler, R. P., et al. 2000, *ApJL*, 529, L41
- Heppenheimer, T. A. 1978, *A&A*, 65, 421
- Hinz, P. M., Bippert-Plymate, T., Breuninger, A., et al. 2012, in *SPIE Conf. Ser.*, Vol. 8446
- Høg, E., Fabricius, C., Makarov, V. V., et al. 2000, *A&A*, 355, L27
- Holczer, T., Mazeh, T., Nachmani, G., et al. 2016, *ApJS*, 225, 9
- Holman, M. J. & Wiegert, P. A. 1999, *AJ*, 117, 621
- Howard, A. W., Johnson, J. A., Marcy, G. W., et al. 2010, *ApJ*, 721, 1467

- Howard, A. W, Marcy, G. W, Bryson, S. T, et al. 2012. *ApJS*, 201, 15
- Howard, A.W. 2013, *Science*, 340, 572
- Howell, S. B., Sobeck, C., Haas, M., et al. 2014, *PASP*, 126, 398
- Huang C., Wu Y. & Triaud A. H. M. J., 2016, *ApJ*, 825, 98
- Huber, J. P., Bedding, T. R. & O'Toole, S. J. 2003, in *Asteroseismology across the HR Diagram*, ed. M. J. Thompson, Volume 284, 421
- Huber, D., Bedding, T. R., Stello, D., et al. 2010, *ApJ*, 723, 1607
- Huber, D., Bedding, T. R., Stello, D., et al. 2011, *ApJ*, 743, 143
- Huber, D., Ireland, M. J., Bedding, T. R., et al. 2012, *ApJ*, 760, 32
- Huber, D., Chaplin, W.J., Christensen-Dalsgaard, J., et al. 2013a, *ApJ*, 767, 127
- Huber, D., Carter, J. A., Barbieri, M., et al. 2013b, *Sci*, 342, 331
- Hunter, J. D. 2007, *CSE*, 9, 90
- Hurley, J. R., Tout, C. A., & Pols, O. R. 2002, *MNRAS*, 329, 897
- Ida, S., & Lin, D. N. C. 2005, *ApJ*, 626, 1045
- Jackson, B., Barnes, R. & Greenberg, R. 2008, *MNRAS*, 391, 237
- Jang-Condell, H. 2015, *ApJ*, 799, 147
- Jeffreys, H. 1961, *Theory of Probability* (Third edition). Oxford: University Press.
- Jeffreys, H. 1973, *Scientific Inference* (3rd ed.). Cambridge University Press.
- Jeffries, R. D. 1997, *MNRAS*, 288, 585
- Jofré, E., Petrucci, R., Saffe, C., et al. 2015, *A&A*, 574, 50
- Johansen, A., Oishi, J. S., Mac Low, M.-M., et al. 2007, *Nature*, 448, 1022
- Johnson, J. A., Marcy, G. W., Fischer, D. A., et al. 2006, *ApJ*, 652, 1724
- Johnson, J. A., Fischer, D. A., Marcy, G. W., et al. 2007, *ApJ*, 665, 785
- Johnson, J. A., Bowler, B., Howard, A., et al. 2010, *ApJ*, 721, 153
- Johnson, J. A., Payne, M., Howard, A., et al. 2011, *AJ*, 141, 16
- Jones, M. I., Jenkins, J. S., Rojo, P. & Melo, C. H. F. 2011, *A&A*, 536, 71
- Jones, M., Jenkins, J., Rojo, P., et al., 2013, *A&A*, 556, 78
- Jones, M. I., Jenkins, J. S., Bluhm, P., et al. 2014, *A&A*, 566, 113
- Jones, M. I., Jenkins, J. S., Rojo, P., et al. 2015a *A&A*, 573, 3
- Jones, M. I., Jenkins, J. S., Rojo, P., et al. 2015b *A&A*, 580, 14
- Jones, M. I., Jenkins, J. S., Brahm, R., et al. 2016, *A&A*, 590, 38
- Jorissen, A., Van Eck, S., Van Winckel, H., et al. 2016a, *A&A*, 586, A158
- Jorissen, A., Hansen, T., Van Eck, S., et al. 2016b, *A&A*, 586, A159
- Kalirai, J. S., Saul Davis, D., Richer, H. B., et al. 2009, *ApJ*, 705, 408

- Kallinger, T., Hekker, S., Mosser, B., et al. 2012, *A&A*, 541, A51
- Kaltenegger, L. & Haghighipour, N. 2013, *ApJ*, 777, 165
- Kane, M. R. & Gelino, D. M. 2010, *ApJ*, 724, 818
- Karakas, A. I., Tout, C. A. & Lattanzio, J. C. 2000, *MNRAS*, 316, 689
- Käufel, H. U., Ballester, P., Biereichel, P., et al. 2004, *SPIE*, Vol. 5492
- Kipping, D.M. 2010, *MNRAS*, 408, 1758
- Kipping, D.M. 2013, *MNRAS*, 435, 2152
- Kjeldsen, H. & Bedding, T. R., 1995, *A&A*, 293, 87
- Kjeldsen, H. & Bedding, T. R. 2011, *A&A*, 529, L8
- Kley, W. & Nelson, R. P. 2008, *A&A*, 486, 617
- Kley, W. & Haghighipour, N. 2014, *A&A*, 564, 72
- Koch, A. & Woehl, H. 1984, *A&A*, 134, 134
- Kozai, Y. 1962, *AJ*, 67, 591
- Kretke, K., Lin, D., Garaud, P., et al. 2009, *ApJ*, 690, 407
- Kuiper, G. P. 1951, *PNAS*, 37, 1
- Kunitomo, M., Ikoma, M., Sato, et al. 2011, *ApJ*, 737, 66
- Kürster, M., Endl, M., Rouesnel, F., et al. 2003, *A&A*, 403, 1077
- Lafrenière, D., Doyon, R., Marois, C., et al. 2007, *ApJ*, 670, 1367
- Lainey V., Arlot J.-E., Karatekin O., et al. 2009, *Nature*, 459, 957
- Lambert, J. H. 1760, *Photometria sive de mensura de gratibus luminis, colorum umbrae* (Augsburg: Eberhard Klett)
- Laplace, P. S. 1812, *Théorie Analytique des Probabilités*. Paris: Courcier. Reprinted as *Oeuvres Complètes de Laplace 7, 1878–1912*. Paris: Gauthier-Villars
- Larwood, J. D., Nelson, R. P., Papaloizou, J. C. B., et al. 1996, *MNRAS*, 282, 597
- Latham, D. W., Rowe, J. F., Quinn, S. N., et al. 2011, *ApJL*, 732, L24
- Laughlin, G., Crismani, M., & Adams, F. C. 2011, *ApJ*, 729, L7
- Leconte, J., Chabrier, G., Baraffe, I., et al. 2010, *A&A*, 516, A64
- Lee, B.-C., Mkrtychian, D. E., Han, I., et al. 2011, *A&A*, 529, A134
- Lee, E. J., Chiang, E., & Ormel, C. W. 2014, *ApJ*, 797, 95
- Lee B.-C., Park M.-G., Lee S.-M., et al. 2015, *A&A*, 584, A79
- Lei, Z.-X., Chen, X.-F., Zhang, F.-H., et al. 2013, *A&A*, 549, 145
- Leisenring, J. M., Skrutskie, M. F., Hinz, P. M., et al. 2012, in *SPIE Conf. Ser.*, Vol. 8446
- Liddle, A. R. 2004, *MNRAS*, 351, L49
- Liddle, A. R. 2007, *MNRAS*, 377, L74

- Lidov, M. L. 1962, *Planet. Space Sci.*, 9, 719
- Lillo-Box, J., Barrado, D., Moya, A., et al 2014a, *A&A*, 562, A109
- Lillo-Box, J., Barrado, D., Henning, T., et al 2014b, *A&A*, 568, L1
- Lillo-Box, J., Ribas, A., Barrado, D. 2016a, *A&A*, 592, 32
- Lillo-Box, J., Barrado, D. & Correia, A. C. M. 2016b, *A&A*, 589, 124
- Lindgren, L., Lammers, U., Bastian, U., et al. 2016, arXiv:1609.04303
- Lissauer, J. J. 1993, *ARA&A*, 31, 129
- Lissauer, J. J., Ragozzine, D., Fabrycky, D. C., et al. 2011, *ApJS*, 197, 8
- Lissauer, J., Marcy, G., Bryson, S., et al. 2014, *ApJ*, 784, 44
- Liu, Y. J., Sato, B., Zhao, G., et al. 2008, *ApJ*, 672, 553
- Livio, M., & Soker, N. 1983, *AJ*, 125, 12
- Livio, M., & Soker, N. 1984, *MNRAS*, 208, 763
- Lo Curto, G., Pasquini, L., Manescau, A., et al. 2012, *The Messenger*, 149, 2
- Loeb, A., & Gaudi, B. S. 2003, *ApJ*, 588, L117
- Lloyd, J. P. 2011, *ApJ*, 739, 49
- Lloyd, J. P. 2013, *ApJ*, 774, 2
- Lopez, E. D. & Fortney, J. J. 2016, *ApJ*, 818, 4
- López-Morales, M. & Seager, S. 2007, *ApJ*, 667, L191
- Lovis, C. & Mayor, M. 2007, *A&A*, 472, 657
- Loyd R. O. P. & France K. 2014, *ApJS*, 211, 9
- Ma, B., Ge, J., Wolszczan, A., et al. 2016, arXiv:1608.03597
- Maire, A., Skemer, A., Hinz, P., et al 2015, *A&A*, 576, 133
- Maldonado J., Villaver E. & Eiroa C., 2013, *A&A*, 554, A84
- Maldonado, J. & Villaver, E. 2016, *A&A*, 588, 98
- Malmberg, D., de Angeli, F., Davies, M. B., et al. 2007, *MNRAS*, 378, 1207
- Mandel, K. & Agol, E. 2002, *ApJ*, 580, L171
- Marcy, G. & Butler, P. 1992, *PASP*, 104, 270
- Marcy, G. & Butler, P. 1993, *ASP Conf. Ser.*, 47, 175
- Marcy, G. & Butler, P. in *The Bottom of the Main Sequence and Beyond* (ed. Tinney, C.) 98 (Springer, 1994).
- Mardling R. A. & Aarseth S. J. 2001, *MNRAS*, 321, 398
- Marois, C., Lafrenière, D., Doyon, R., et al. 2006, *ApJ*, 641, 556
- Martí, J. G. & Beaugé, C. 2012, *A&A*, 544, 97
- Marzari, F. & Barbieri, M. 2007, *A&A*, 467, 347

- Massarotti, A., Latham, D. W., Stefanik, R. P., et al. 2008, *ApJ*, 135, 209
- Masseron, T., Johnson, J. A., Plez, B., et al. 2010, *A&A*, 509, A93
- Matsumura, S., Takeda, G., & Rasio, F. A. 2008, *ApJ*, 686, L29
- Mawet, D., Milli, J., Wahhaj, Z., et al. 2014, *ApJ*, 792, 97
- Maxted, P. F. L., Marsh, T. R. & Moran, C. K. J. 2000, *MNRAS*, 319, 305
- Mayer, L., Wadsley, J., Quinn, T., et al. 2005, *MNRAS*, 363, 641
- Mayer, L., Boss, A. & Nelson, A. F. 2007, arXiv0705.3182
- Mayor, M. & Queloz, D. 1995, *Nature*, 378, 355
- Mayor, M., Udry, S., Naef, D., et al. 2004, 415, 391
- Mazeh, T. 2008, in *Tidal Effects in Stars, Planets, & Disks*, ed. M.-J. Goupil & J.-P. Zahn (EAS Pub. Series 29; Les Ulis: EDP), 1
- McCabe, C., Duchene, G. & Ghez, A. M. 2003, *ApJ*, 588, 113
- Mckinney, W. 2010, 51, 56
- McQuillan, A., Mazeh, T. & Aigrain, S. 2013, *ApJ*, 775, 11M
- Meibom, S., & Mathieu, R. D. 2005, *ApJ*, 620, 970
- Merand, A., Borde, P. & Coudé du Foresto, V. 2004, *SPIE*, Vol. 5491
- Meshkat, T., Kenworthy, M. A., Quanz, S. P., et al. 2014, *ApJ*, 780, 17
- Meschiari, S. 2014, *ApJ*, 790, 41
- Metropolis, N. & Ulam, S. 1949, *Journal of the American Statistical Association*, 44
- Metropolis, N., Rosenbluth, A. W., Rosenbluth, M. N., et al. 1953, *Journal of Chemical Physics*, 21, 1087
- Michalik, D., Lindegren, L., & Hobbs, D. 2015, *A&A*, 574, A115
- Miglio, A. 2012a, *ASSP*, 26, 11
- Miglio, A., Brogaard, K., Stello, D., et al. 2012b, *MNRAS*, 419, 2077
- Miller, N., & Fortney, J. J. 2011, *ApJ*, 736, L29
- Mitchell, D. S., Reffert, S., Trifonov, T., et al. 2013, *A&A*, 555, 87
- Mizuno, H. 1980, *PThPh*, 64, 544
- Montet, B. T., Crepp, J. R., Johnson, J. A., et al. 2014, *ApJ*, 781, 28M
- Morais, M. H. M. & Correia, A. C. M. 2008, *A&A*, 491, 899
- Morais, M. H. M. & Correia, A. C. M. 2011, *A&A*, 525, 152
- Morris, S. L. 1985, *ApJ*, 295, 143
- Mortier, A., Santos, N. C., Sousa, S. G., et al. 2013, *A&A*, 557, AA70
- Morton, T. D., Bryson, S. T., Coughlin, J. L., et al. 2016, *ApJ*, 822, 86
- Mosser, B., Michel, E., Belkacem, K., et al. 2013, *A&A*, 550, A126

- Mugrauer, M., Neuhäuser, R., & Mazeh, T. 2009, A&A, 494, 373
- Mulders, G. D, Pascucci I. & Apai D. 2015. ApJ, 798, 112
- Müller, T. W. A., & Kley, W. 2012, A&A, 539, A18
- Murphy, M. T., Udem, T., Holzwarth, R., et al. 2007, MNRAS, 380, 839
- Mustill, A. J. & Villaver, E. 2012, ApJ, 761, 121
- Mustill, A. J., Davies, M. B. & Johansen, A. 2015, ApJ, 808, 14
- Nagasawa, M., Ida, S., & Bessho, T. 2008, ApJ, 678, 498
- Nelson, A. F. 2000, ApJ, 537, L65
- Newton, I. 1687, *Philosophiæ Naturalis Principia Mathematica*, Jussu Societatis Regiæ ac Typis Joseph Streater
- Niedzielski, A., Wolszczan, A., Nowak, G., et al., 2015, ApJ, 803, 1
- Niedzielski, A., Deka-Szymankiewicz, B., Adamczyk, M., et al. 2016, A&A, 585, A73
- Niedzielski, A., Villaver, E., Nowak, G., et al. 2016, A&A, 589, L1
- Noguchi, K., Aoki, W., Kawanomoto, S., et al. 2002, PASJ, 54, 855
- Nowak, G. 2013, PhD thesis, Nicolaus Copernicus Univ., Toruń, Poland
- Ogilvie, G. I., & Lin, D. N. C. 2004, ApJ, 610, 477
- O’Neal, D. 2006, ApJ, 645, 659
- Orosz, J. A., Welsh, W. F., Carter, J. A., et al. 2012a, ApJ, 758, 87
- Orosz, J. A., Welsh, W. F., Carter, J. A., et al. 2012b, Science, 337, 1511
- Ortiz, M., Gandolfi, D., Reffert, S., et al 2015, A&A, 573, L6
- Ortiz, M., Reffert, S., Trifonov, T., et al 2016, A&A, 595, A55
- Paardekooper, S.-J., Thébault, P., & Mellema, G. 2008, MNRAS, 386, 973
- Paardekooper, S.-J., & Leinhardt, Z. M. 2010, MNRAS, 403, L64
- Pál, A. 2008, MNRAS, 390, 281
- Parviainen, H. 2015, MNRAS, 450, 3233
- Pasquini, L., Döllinger, M. P., Weiss, A., et al. 2007, A&A, 473, 979
- Peale, S. J. 1999, ARA&A, 37, 533
- Pepe, F., Mayor, M., Delabre, B., et al. 2000, Proc. SPIE, 4008, 582
- Pepe, F., Mayor, M., Galland, F., et al. 2002, A&A, 388, 632
- Pepe, F., Molaro, P., Cristiani, S., et al. 2014, Astronomische Nachrichten, 335, 8
- Pepper, J., Siverd, R. J., Beatty, T. G., et al. 2013, ApJ, 773, 64
- Percy, J. R., Wilson, J. B. & Henry, G. W. 2001, PASP, 113, 983
- Percy, J. R., Mashintsova, M., Nasui, C. O., et al. 2008, PASP, 120, 523
- Perets, H. B. 2010, arXiv:1001.0581

- Perets, H. B., & Kouwenhoven, M. B. N. 2012, *ApJ*, 750, 83
- Perez, F. & Granger, B. 2007, *CSE*, 21
- Perna, R., Menou, K., & Rauscher, E. 2010, *ApJ*, 724, 313
- Perna, R., Heng, K., & Pont, F. 2012, *ApJ*, 751, 59
- Perryman, M. 2011, *The Exoplanet Handbook*, Cambridge University Press; 1 edition
- Perryman, M., Hartman, J., Bakos, G., et al. 2014, *ApJ*, 797, 14
- Peterson, P. 2009, *CSE*, 4, 296
- Petigura, E.A., Marcy, G.W. & Howard, A.W. 2013, *ApJ*, 770, 69
- Petrovich, C. 2015, *ApJ*, 805, 75
- Petrovich, C. & Tremaine, S. 2016, arXiv:1604.00010
- Pfahl, E. 2005, *ApJ*, 635, L89
- Pfahl, E. & Muterspaugh, M. 2006, *ApJ*, 652, 1694
- Pfahl, E., Arras, P. & Paxton, B. 2007, 13
- Pfahl, E., Arras, P. & Paxton, B. 2008, *ApJ*, 679, 783
- Pichardo, B., Sparke, L. S. & Aguilar, L. A. 2005, *MNRAS*, 359, 521
- Pilat-Lohinger, E. & Dvorak., R. 2002, *Celestial Mechanics and Dynamical Astronomy*, 82, 143
- Pilat-Lohinger, E., Funk, B. & Dvorak., R. 2003, *A&A*, 400, 1085
- Pisknuov, N. & Valenti, J. A. 2016, arXiv:1606.06073
- Placco, V. M., Frebel, A., Beers, T. C., et al. 2014, *ApJ*, 797, 21
- Pojmański, G. 1997, *Acta Astron.*, 47, 467
- Pojmański, G. 2001, in *Small Telescope Astronomy on Global Scales*, eds. B. Paczynski, W.-P. Chen, & C. Lemme, *IAU Colloq. 183, ASP Conf. Ser.*, 246, 53
- Pollack, J. B. 1984, *ARA&A*, 22, 389
- Pollack, J. B., Hubickyj, O., Bodenheimer, P., et al. 1996, *Icarus*, 124, 62
- Portegies Zwart, S. F. & McMillan, S. L. 2005, *ApJ*, 633, L141
- Press, W. H., Teukolsky, S. A., Vetterling, W. T., et al. 1992, *Numerical recipes in FORTRAN. The art of scientific computing* (Cambridge University Press)
- Queloz, D. 1995, *New Developments in Array Technology and Applications*, volume 167 of *IAU Symposium*, 221
- Queloz, D., Mayor, M., Weber, L., 2000, *A&A*, 354, 99
- Queloz, D., Henry, G. W., Sivan, J. P., et al. 2001, *A&A*, 379, 279
- Quinn, S. N., White, R. J., Latham, D. W., et al. 2014, *ApJ*, 787, 27
- Quinn, S. N., White, T. R., Latham, D. W., et al. 2015, *ApJ*, 803, 49
- Quintana, E. V., Adams, F. C., Lissauer, J. J., et al. 2007, *ApJ*, 660, 807

- Quirrenbach, A., Amado, P. J., Mandel, H., et al. 2010, *Proc. SPIE*, 7735, E13
- Quirrenbach, A., Reffert, S. & Bergmann, C. 2011, *AIPCS*, Vol. 1331, 102
- Quirrenbach, A., Amado, P. J., Seifert, W., et al. 2012, *Proc. SPIE*, 8446, E0R
- Rabl, G. & Dvorak., R. 1988, *A&A*, 191, 385
- Rafikov, R. R. 2005, *ApJL*, 621, L69
- Rafikov, R. & Silsbee, K. 2015, *ApJ*, 798, 70
- Raghavan, D., Henry, T. J., Mason, B. D., et al. 2006, *ApJ*, 646, 523
- Raghavan, D., McAlister, H. A., Henry, T. J., et al. 2010, *ApJS*, 190, 1
- Rajpaul, V., Aigrain, S., & Roberts, S. 2016, *MNRAS*, 456, L6
- Ramm D. J., Pourbaix D., Hearnshaw J. B., et al. 2009, *MNRAS*, 394, 1695
- Ramm D. J. 2015, *MNRAS*, 449, 4428
- Ramm D. J. 2016, *arXiv:1605.05453*
- Rauer, H., Catala, C., Aerts, C., et al. 2014, *Experimental Astronomy*, 38, 249
- Reffert, S., Quirrenbach, A., Mitchell, D. S., et al. 2006, *ApJ*, 652, 661
- Reffert, S., Bergmann, C., Quirrenbach, A., et al. 2015, *A&A*, 574, 116
- Reiners, A., Banyal, R. K., & Ulbrich, R. G. 2014, *A&A*, 569, A77
- Reimers, D. 1975, *Mém. Soc. Roy. Sci. Liège*, 8, 369
- Reuyl, D., & Holmberg, E. 1943, *ApJ*, 97, 41
- Ribas, I., Font-Ribera, A. & Beaulieu, J.-P. 2008, *ApJ*, 677, L59
- Ricker, G. R., Winn, J. N., Vanderspek, R., et al. 2014, in *Society of Photo-Optical Instrumentation Engineers (SPIE) Conference Series*, Vol. 9143, *Society of Photo-Optical Instrumentation Engineers (SPIE) Conference Series*, 20
- Riddle, R. L., Tokovinin, A., Mason, B. D., et al. 2015, *ApJ*, 799, 4
- Roberts, J. L. C., Turner, N. H., ten Brummelaar, T. A., et al. 2011, *AJ*, 142, 175
- Rodriguez, L. F., D'Alessio, P., Wilner, D. J., et al. 1998, *Nature*, 395, 355
- Roell, T., Neuhauser, R., Seifahrt, A., et al. 2012, *A&A*, 542, A92
- Rosenblatt, F. 1971, *Icarus*, 14, 71
- Rowe, J., Bryson, S., Marcy, G., et al. 2014, *ApJ*, 784, 45
- Russell, H. N. 1916, *ApJ*, 43, 173
- Rybicki, G. B. & Lightman, A. P. 1979, *Radiative Processes in Astrophysics* (New York: Wiley)
- Sadakane, K., Ohnishi, T., Ohkubo, M., et al. 2005 *PASJ*, 57, 127
- Santerne, A., Hébrard, G., Deleui, M., et al. 2014, *A&A*, 571, 37
- Santos, N. C., Israelian, G., & Mayor, M. 2004, *A&A*, 415, 1153
- Santos, N. C., Lovis, C., Pace, G, et al. 2009, *A&A*, 493, 309

- Sato, B., Kambe, E., Takeda, Y., et al. 2002, PASJ, 54, 873
- Sato, B., Ando, H., Kambe, E., et al. 2003, ApJ, 597, L157
- Sato, B., Izumiura, H., Toyota, E., et al. 2008, PASJ, 60, 539
- Sato, B., Omiya, M., Harakawa, H., et al. 2013, PASJ, 65, 85
- Sato, B., Hirano, T., Omiya, M., et al. 2015, ApJ, 802, 57
- Saumon, D. & Guillot, T., 2003, ApJ, 609, 1170
- Schäfer, S. & Reiners, A. 2012, in Society of Photo-Optical Instrumentation Engineers (SPIE) Conference Series, Vol. 8446
- Schlaufman, K. & Winn, J., 2013, ApJ, 772, 143
- Schlaufman, K. C., & Winn, J. N. 2016, ApJ, 825, 62
- Schleicher, D. & Dreizler, S. 2014, A&A, 563, 61
- Schneider, J. & Cabrera, J. 2006, A&A, 445, 1159
- Schneider, J., Dedieu, C., Le Sidaner, P., et al. 2011, A&A, 532, A79
- Schuler, S. C., Kim, J. H., Tinker, M. C., et al. 2005, ApJ, 632, 131
- Schulze-Hartung, T., Launhardt, R. & Henning, T. 2012, A&A, 545, 79
- Schwab, C., Stuermer, J., Gurevich, Y. V., et al. 2015, PASP, 127, 880
- Schwamb, M. E., Orosz, J. A., & Carter, J. A. 2013, ApJ, 768, 127
- Schwarz, G. 1978, Ann. Stat., 6, 461
- Seager, S., Whitney, B. A. & Sasselov, D. D. 2000, ApJ, 540, 504
- Seager, S. & Mallén-Ornelas, G. 2003, ApJ, 585, 1038
- Seager, S., Kuchner, M., Hier-Majumder, C. A., et al. 2007, ApJ, 669, 1279
- Shporer, A., Jenkins, J. M., Rowe, J. F., et al. 2011, AJ, 142, 195
- Siess, L., Davis, P. J. & Jorissen, A. 2014, A&A, 565, 57
- Silsbee, K. & Rafikov, R. R. 2015, ApJ, 808, 58
- Sing, D. K. 2010, A&A, 510, A21
- Skrutskie, M. F., Cutri, R. M., Stiening, R., et al. 2006, AJ, 131, 1163
- Skrutskie, M. F., Jones, T., Hinz, P., et al. 2010, in SPIE Conf. Ser., Vol. 7735
- Sliski, D.H. & Kipping, D.M. 2014, ApJ, 788, 148
- Sobolev, V. V. 1975, Light Scattering in Planetary Atmospheres (Oxford: Pergamon Press), 263
- Socrates, A., Katz, B., Dong, S., et al. 2012, ApJ, 750, 106
- Soumer, R., Pueyo, L. & Larkin, J. 2012, ApJL, 755, L28
- Sozzetti, A. 2011, EAS Publications Series, 45, 273
- Spurzem, R., Giersz, M., Heggie, D. C., et al. 2009, ApJ, 697, 458
- Steffen, J. H., Ragozzine, D., Fabrycky, D. C., et al. 2012, PNAS, 109, 7982

- Steffen, J.H., Fabrycky, D.C, Agol, E., et al. 2013, MNRAS, 428, 1077
- Stello, D., Huber, D., Bedding, T. R., et al. 2013, ApJ, 765, 41
- Stevens, D. J., Gaudi, B. S. 2013, PASP, 125, 933
- Storn, R. & Price, K. 1997, JGO, 11, 341
- Strand, K.A. 1943, PASP, 55, 29
- Struve, O. 1952, The Observatory, 72, 199
- Sudarsky, D., Burrows, A., & Pinto, P. 2000, ApJ, 538, 885
- Sudarsky, D., Burrows, A. & Hubeny, I. 2003, ApJ, 588, 1121
- Sudarsky, D., Burrows, A., Hubeny, I., et al. 2005, ApJ, 627, 520
- Takeda, G. & Rasio, F. A. 2005, ApJ, 627, 1001
- Takeda, Y., Sato, B., & Murata, D. 2008, PASJ, 60, 781
- Tanner, M. A. & Wong, W. H. 1987, Journal of the American Statistical Association, 82, 528
- Telting, J. H., Avila, G., Buchhave, L., et al. 2014, AN, 335, 41
- ten Brummelaar, T. A., McAlister, H. A., Ridgway, S. T., et al. 2005, ApJ, 628, 453
- Thébault, P., Marzari, F., Scholl, H., et al. 2004, A&A, 427, 1097
- Thébault, P., Marzari, F. & Scholl, H., et al. 2006, Icarus, 183, 193
- Thébault, P., Marzari, F. & Scholl, H. 2008, MNRAS, 388, 1528
- Thébault, P., Marzari, F. & Scholl, H. 2009, MNRAS, 393, L21
- Thébault P. & Haghhighipour N., 2015, in Planetary Exploration and Science: Recent Results and Advances. Springer Geophysics. p. 309
- Toomre A., 1964, ApJ, 139, 1217
- Tout, C. A., & Eggleton, P. P. 1988, MNRAS, 231, 823
- Trifonov, T., Reffert, S., Tan, X., et al. 2014, A&A, 568, 64
- Trifonov, T., Reffert, S., Zechmeister, M., et al. 2015, A&A, 582, 54
- Tull, R. G. 1998, Proc. SPIE, 3355, 387
- Tutukov, A. V. & Fedorova, A. V. 2012, Astron. Rep., 56, 305
- Udry, S., Mayor, M. & Queloz, D. 1999, ASPC, 185, 367
- Udry, S. & Santos, N. C. 2007, ARA&A, 45, 397
- Valenti, J. A., Butler, R. P., & Marcy, G. W. 1995, PASP, 107, 966
- Valenti, J. A. & Piskunov, N. A&AS, 118, 595
- Valenti, J. A. & Fischer, D. A. ApJS, 159, 141
- Vanderplas, J. T., Connolly, A. J., Ivezić, Ž., et al. 2012, proc. of CIDU, pp. 47-54
- van der Walt, S., Colbert, S.C. & Varoquaux, G. 2011
- Van Eylen, V., Albrecht, S., Gandolfi, D., et al. 2016, arXiv:1605.09180

- van Leeuwen, F. 2007, *A&A*, 474, 653
- Villaver, E. & Livio, M., 2009, *ApJ*, 705, 81
- Villaver, E., Livio, M., Mustill, A., 2014, *ApJ*, 794, 3
- Vogt, S. S. 1987, *PASP*, 99, 1214
- Vogt, S. S., Butler, R. P., Marcy, G. W., et al. 2002, *ApJ*, 568, 352
- Vos, J., Østensen, R. H., Marchant, P., et al. 2015, *A&A*, 579, 49
- Wagner, K., Apai, D., Kasper, M., et al. 2016, *Science*, 353, 673
- Walker, G. A. H., Walker, A. R., Irwin, A. W., et al. 1995, *Icarus*, 116, 359
- Wang, Sharon, X., Wright, J.T., Cochran, W., et al. 2012, *ApJ*, 761, 46
- Wang, J., Xie, J.-W., Barclay, T., & Fischer, D. 2014, *ApJ*, 783, 4
- Weidemann, V. 1977, *A&A*, 59, 411
- Weidemann, V. 1987, *A&A*, 188, 74
- Weidemann, V. 1990, *ARA&A*, 28, 103
- Weiss, L., Marcy, G., Rowe, J., et al. 2013, *ApJ*, 768, 14
- Welsh, W. F., Orosz, J. A., Carter, J. A., et al. 2012, *Nature*, 481, 475
- White, T. R., Bedding, T. R., Stello, D., et al. 2011, *ApJ*, 743, 161
- Whitmire, D. P., Matese, J. L., Criswell, L., et al. 1998, *Icarus*, 132, 196
- Wiegert, J., Faramaz, V. & Cruz-Saenz de Miera, F. 2016, *MNRAS*, 462, 1735
- Wildi, F., Pepe, F., Chazelas, B., et al. 2010, in *Society of Photo-Optical Instrumentation Engineers (SPIE) Conference Series*, Vol. 7735
- Wilken, T., Lo Curto, G., Probst, R. A., et al. 2012, *Nature*, 485, 611
- Windmark, F., Birnstiel, T., Güttler, C., et al. 2012, *A&A*, 540, A73
- Winn, J. N. 2009, in *IAU Symposium*, Vol. 253, *IAU Symposium*, ed. F. Pont, D. Sasselov, & M. J. Holman, 99–109
- Wittenmyer, R. A., Butler, R. P., Wang, L., et al. 2016, *MNRAS*, 455, 1398
- Wolszczan, A., & Frail, D. A. 1992, *Nature*, 355, 145
- Wright, J. T. & Howard, A. W. 2009, *ApJS*, 182, 205
- Wright, J. T., & Gaudi, B. S. 2013, *Exoplanet Detection Methods*, ed. T. D. Oswalt, L. M. French, & P. Kalas, 489
- Wu, Y. 2005, *ApJ*, 635, 688
- Wu, Y. & Lithwick, Y. 2011, *ApJ*, 735, 109
- Wu, Y. & Lithwick, Y. 2013, *ApJ*, 763, 13
- Xie, J.-W., Payne, M. J., Thébault, P., et al. 2010, *ApJ*, 724, 1153
- Yi, X., Vahala, K., Li, J., et al., 2016, *Nature Communications*, 7, 10436

Zechmeister, M. & Kürster, M. 2009, *A&A*, 496, 577

Zewail, A & Thomas, J. (2010), *4D Electron Microscopy: Imaging in Space and Time*, World Scientific, ISBN 9781848163904

Zorotovic, M., & Schreiber, M. R. 2013, *A&A*, 549, A95

Zucker, S. & Mazeh, T. 2002, *ApJ*, 568, 113

Zucker, S., Mazeh, T., Santos, N. C., et al. 2004, *A&A*, 426, 695

Zucker, S., Mazeh, T. & Alexander, T. 2007, *ApJ*, 670, 1326

